Biopolymer and Synthetic Polymer Nanocomposite Reinforcement via Interfacial Assembly

A Dissertation
Presented to
The Academic Faculty

by

Anise M. Grant

In Partial Fulfillment
of the Requirements for the Degree
Doctor of Philosophy in the
School of Materials Science and Engineering

Georgia Institute of Technology
August 2019

Biopolymer and Synthetic Polymer Nanocomposite Reinforcement via Interfacial Assembly

Approved by:

Dr. Vladimir V. Tsukruk, Advisor
School of Materials Science and Engineering
Georgia Institute of Technology

Dr. Rajesh Naik
711th Human Performance Wing
Air Force Research Laboratory

Dr. Zhiqun Lin
School of Materials Science and Engineering
Georgia Institute of Technology

Dr. Meisha Shofner
School of Materials Science and Engineering
Georgia Institute of Technology

Dr. Valeria Milam
School of Materials Science and Engineering
Georgia Institute of Technology

Date Approved: May 20, 2019

This dissertation is dedicated to my family and friends, professional mentors, and colleagues who supported me, advised me on how to navigate graduate school, and read countless fellowship, grant, and publication drafts needed to get me to the finish line. Special thanks to my parents, Mrs. Helen Taylor, Dr. Amanda Gable, Dr. Meisha Shofner, Dr. Vladimir Tsukruk, Dr. Kesong Hu, Dr. Seth Young, and Michelle Krecker.

ACKNOWLEDGEMENTS

This material is based upon work supported by the National Science Foundation CBET-1402712, National Science Foundation Graduate Research Fellowship under Grant No. DGE-1148903, the Air Force Office for Scientific Research, FA9550-14-1-0269 Award and UES-AFRL.

TABLE OF CONTENTS

ACKNOWLEDGEMENTS iv

LIST OF TABLES viii

LIST OF FIGURES ix

LIST OF SYMBOLS AND ABBREVIATIONS xvii

SUMMARY xx

Introduction 22
1.1 Background 22
1.1.1 Silk fibroin 23
1.1.2 Suckerin 25
1.1.3 Synthetic copolymers 29
1.1.4 Graphene 31
1.2 Fundamental Issues 34

Research Goals, Objectives, and Overview 37
1.3 Goals and Objectives 37
1.4 Organization and Composition of Dissertation 40

Experimental Techniques and Approaches 42
1.5 Polymers: Biopolymers and Synthetic Copolymers 42
1.5.1 Preparation of silk fibroin 42
1.5.2 Preparation of suckerin-12 42
1.5.3 Preparation of synthetic copolymers P(G66-O34) and P(G15-O66-L19) 43
1.6 Substrates 44
1.6.1 Preparation of silicon dioxide surface 45
1.6.2 Preparation of graphene derivatives 45
1.7 Experimental techniques 48
1.7.1 Sample fabrication 48
1.7.2 Sample Characterization 49
1.7.3 Molecular dynamics simulations 50

Silk Fibroin Molecular Assembly 52
1.8 Overview 52
1.9 Experimental 52
1.10 Results and discussion 53
1.10.1 Comparison of Silk Fibroin at Different Deposition Conditions 53
1.10.2 Effect of graphene oxidation on silk fibroin assembly behaviour up 58
1.10.3 Simulation Compliance with Experiment 64
1.10.4 Non-bonded Interactions and Protein Synthetic Surface Interfaces 68
1.10.5 Role of silk fibroin heavy chain in adsorption and assembly 69
1.11 Conclusions 72

Protein Assembly and Nanocomposite Toughness **75**
1.12 Overview **75**
1.13 Experimental **76**
1.14 Results and discussion **77**
1.14.1 Fabrication and Morphology of Nanocomposite Membranes 77
1.14.2 Mechanical Properties from Bulging Experiments 80
1.15 Conclusions **84**

Suckerin-12 Aqueous Toughening **86**
1.16 Overview **86**
1.17 Experimental **86**
1.18 Results and discussion **88**
1.18.1 Concentration and deposition mode dependent film formation. 88
1.18.2 Using thermal vapor annealing to drive self-assembly. 91
1.18.3 Hofmeister salt aided stabilization and crystallization. 94
1.18.4 Enzymatic crosslinking for film stability. 97
1.19 Conclusions **103**

Synthetic Copolymer Interfacial Assembly **105**
1.20 Overview **105**
1.21 Experimental **105**
1.22 Results and discussion **106**
1.22.1 Adsorption of copolymer modified GO 106
1.22.2 Adsorption of untethered synthetic copolymers type 1 and 2 110
1.23 Conclusions **113**

General Discussions and Broader Impacts **115**
1.24 General conclusions and future prospects **115**
1.24.1 Insights on assembly from silk fibroin on inorganic substrates and GO nanomembranes 115
1.24.2 Insights on mechanisms of assembly and toughening of suckerin films 117
1.24.3 Insights on the hydrophobic effect and surface adsorption from synthetic copolymers 118
1.25 Prospectus **119**
1.26 Dissemination of work **119**
1.26.1 Peer-reviewed Publications: Primary 119
1.26.2 Peer-reviewed publications: related works 120
1.26.3 Presentations 120
1.26.4 Awards and Recognition 120

Appendices **122**
1.27 Chapter 4 supporting information **122**
1.28 Chapter 5 supporting information **125**
1.29 Chapter 6 supporting information **127**

References **131**

LIST OF TABLES

TABLE 1: WAVENUMBER ASSIGNMENTS FOR SECONDARY STRUCTURES FROM FTIR MEASUREMENTS..... 63

TABLE 2: RATE OF FORMING HYDROGEN BONDS BETWEEN SILK PROTEIN AND VARIOUS SURFACES 68

TABLE 3. THE AMINO ACID COMPOSITION OF BOMBYX MORI HEAVY CHAIN AND THEIR POTENTIAL NONBONDING INTERACTIONS WITH SILK, SIO2, GO, AND RGO..... 71

TABLE 4. SUMMARY OF MECHANICAL PERFORMANCE FOR GO AT VARIOUS CONCENTRATIONS IN DSA-LBL SILK-GO NANOMEMBRANES CHARACTERIZED VIA BULGING TEST. 126

TABLE 5. SUMMARY OF RMS ROUGHNESS MEASUREMENTS DISCUSSED IN THE MAIN TEXT. 129

LIST OF FIGURES

FIGURE 1: (A) *BOMBYX MORI* SILKWORM PICTURED BESIDE ITS COCOON. SCALING DOWN TO THE MOLECULAR LEVEL, EACH FIBER IN THE COCOON HAS THE HIERARCHICAL STRUCTURE OUTLINED IN (B).26 EACH OF THESE FIBERS CONSISTS OF MOSTLY HEXAPEPTIDES WITH STRUCTURES LIKE THAT IN (C) WHICH ARE INTERSPERSED WITH AMORPHOUS REGIMES AS SHOWN IN (D).7 24

FIGURE 2: SCHEMATIC OF SUCKER RING TEETH (A), THE MANY SUCKERIN ISOFORMS IN SUCKER RING TEETH (B) 44, AND THE AMINO ACID SEQUENCE AND SECONDARY STRUCTURES THAT PRIMARILY COMPRISE SUCKERIN (C).45 27

FIGURE 3. A DEPICTION OF THE GO HONEYCOMB STRUCTURE, A NANOMEMBRANE OF SILK AND GO, AFM IMAGE OF GO ON SILICA, AND ELECTROSTATIC FORCE MICROSCOPY IMAGE SHOWING THE OXYGENATION OF THE GO SURFACE. 32

FIGURE 4: SCHEME OF PROPOSED WORK FLOW 38

FIGURE 5: CHEMICAL STRUCTURE OF SYNTHETIC COPOLYMERS P(G66-O34) AND P(G15-O66-L19) 44

FIGURE 6: SCHEME FOR MODIFYING GO WITH THE COPOLYMERS 48

FIGURE 7: AFM TOPOGRAPHICAL IMAGES OF SILK FIBROIN ABSORBED FROM 0.2 (A), 0.02 (B), AND 0.002 WT. % (C). SILK FIBROIN DEPOSITED ON GO FLAKES ON A SILICON WAFER VIA CONVENTIONAL SA-LBL AT 5000 RPM. SCALE: 200 NM. Z RANGE: 4 NM (A AND C) AND 8 NM (B) 55

FIGURE 8: AFM TOPOGRAPHICAL IMAGES OF 0.002 WT. % SILK FIBROIN MORPHOLOGY AFTER CONVENTIONAL SA-LBL ON SIO2 SURFACE (A, B, C) AND GO FLAKES (D, E, F) ON A SILICON WAFER AT 3000 (A, D), 5000 (B,E), AND 8000 (C, F). SCALE: 200 NM. Z RANGE: 2NM (A, B, C, D, E, F) AND 6 NM (D). 56

FIGURE 9: AFM TOPOGRAPHICAL IMAGES OF 0.002 WT.% SILK FIBROIN MORPHOLOGY AFTER DYNAMIC CASTING ON GO FLAKES ON SILICON WAFER AT 1000 (A), 2000 (B), 3000 (C), 4000 (D), 5000 (E), AND 8000 (F) RPM. SCALE: 200 NM. Z RANGE: 2 NM..... 60

FIGURE 10: AFM TOPOGRAPHICAL IMAGES OF 0.002 WT.% SILK FIBROIN MORPHOLOGY AFTER CONVENTIONAL SA-LBL ON RGO FLAKES ON A SILICON WAFER AT 3000 (A), 5000 (B), AND 8000 (C) RPM. SCALE: 500 NM. Z RANGE: 7 NM (A), 11 NM (B), AND 28 NM (C). 61

FIGURE 11: AFM TOPOGRAPHICAL IMAGES OF 0.002 WT.% SILK FIBROIN MORPHOLOGY AFTER DYNAMIC SPIN CASTING ON RGO FLAKES ON A SILICON WAFER AT 1000 (A), 2000 (B), 3000 (C), 4000 (D), 5000 (E), AND 8000 (F) RPM. SCALE: 500 NM. Z RANGE: 8 NM (A AN'D C), 11 NM (B AND E), 2 NM (D), AND 12 NM (F)..... 62

FIGURE 12: ATR-FTIR SPECTRA OF SILK FIBROIN (A), SILK FIBROIN-GO (B), AND SILK FIBROIN-RGO (C) IN THE AMIDE 1 REGION. THE AMOUNT OF EACH SECONDARY STRUCTURE IN EACH SAMPLE CALCULATED FROM PEAK AREA OF THEIR RESPECTIVE PEAKS IS GIVEN IN (E). 64

FIGURE 13: (A) DENSITY PROFILE OF SILK ATOMS NORMAL TO THE GRAPHENE (BLACK), GO 20% (BLUE), SIO2 (RED), AND THE INITIAL SILK STRUCTURE ON GO 20% (GREEN DASHED LINE). (B-E) FINAL SNAPSHOT OF EACH CASE IN (A). (F) DENSITY PROFILE OF SILK PARALLEL TO THE SURFACES WHERE THE INITIAL AND CURRENT STRUCTURES ARE INDICATED BY RED AND BLACK LINES, RESPECTIVELY. 65

FIGURE 14: (A) TEMPORAL PROFILE OF THE PERCENTAGE OF RANDOM COILS (BLACK) AND ORDERED STRUCTURES (GRAY) IN THE SILK STRUCTURE. YELLOW AND RED LINES PASSING THROUGH THE BLACK AND GRAY LINES INDICATE THE AVERAGED VALUES OF THE PERCENTAGE OF RANDOM COILS AND ORDERED STRUCTURE, RESPECTIVELY. (B) B-SHEET CONTENT PER SILK RESIDUE..... 66

FIGURE 15: MD SIMULATION (A) AND EXPERIMENTALLY (C) OBSERVED CHANGES IN THE SECONDARY STRUCTURE OF SILK ON THREE DIFFERENT SURFACES: GRAPHENE (RGO FOR EXPERIMENTAL RESULTS), GO WITH 20 WT. % OXYGEN COVERAGE, AND SIO2. .. 67

FIGURE 16: TEMPORAL PROFILES OF THE NUMBER OF INTERNAL HYDROGEN BONDS FOR SILK PROTEIN ON GRAPHENE (LEFT), GO (CENTER), AND SIO2 (RIGHT) SURFACE, WHERE VALUES FOR SILK AND SILK-SURFACE HYDROGEN BONDING ARE REPRESENTED BY BLACK AND GRAY LINES, RESPECTIVELY. AVERAGE VALUES ARE FOR SILK AND SILK-SURFACE HYDROGEN BONDING ARE SHOWN IN YELLOW AND RED LINES, RESPECTIVELY. 68

FIGURE 17. A SCHEMATIC LISTING THE AMINO ACIDS IN THE SILK HEAVY CHAIN, CATEGORIZED BY HYDROPATHY, POLARITY, CHARGE, AND TENDENCY FOR NONBONDING INTERACTIONS. (18) 70

FIGURE 17: MORPHOLOGIES OF THE STRETCHED SILK FIBROIN ON GO SURFACES. (A, B) SURVEY AND HIGH-RESOLUTION AFM IMAGES SHOWING THE UNIFORM DISTRIBUTION OF SILK FIBROIN MOLECULES WITHOUT SIGNIFICANT AGGREGATION OR ENTANGLEMENT (Z-SCALES: 2 NM). (C–F) CROSS-SECTIONAL PROFILE OF THE SINGLE MOLECULES FROM THE COLOR-CODED LINES IN (B)..... 78

FIGURE 18: FTIR SPECTRA OF THE SILK SPUN USING THE (A) CONVENTIONAL SA-LBL AND (B) DSA-LBL. (C) PEAK ASSIGNMENT OF THE FTIR SPECTRA. (D) COMPOSITION OF THE SECONDARY STRUCTURES OF THE SILK..... 80

FIGURE 19: STRUCTURE AND COMPOSITION OF THE GO–SILK FIBROIN NANOCOMPOSITE MEMBRANE. (A) AFM IMAGE AND HEIGHT PROFILE OF FILM EDGE (Z-SCALE: 350 NM) SHOWING THE 45 NM THICK GO–SILK FIBROIN NANOCOMPOSITE MEMBRANE ON TOP OF THE 103 NM THICK SACRIFICIAL PS LAYER. (B) ELLIPSOMETRY DATA SHOW THAT THE THICKNESS OF THE MEMBRANES INCREASES LINEARLY WITH THE NUMBER OF THE GO–SILK FIBROIN BILAYERS ASSEMBLED. (C) XRD DATA AND PEAK FITTING OF A 70-

BILAYER GO–SILK FIBROIN DSA-LBL MEMBRANE ON SILICON WAFER. THE SILICON WAFER BACKGROUND IS SUBTRACTED. (D) XPS OF THE-E GO–SILK FI-BROIN NANOMEMBRANES IN COMPARISON WITH THAT FOR PURE SILK FILMS. 81

FIGURE 20: (A) OPTICAL IMAGE OF THE GO–SILK FIBROIN NANOCOMPOSITE MEMBRANE SUSPENDED ACROSS A 300 MM COPPER APERTURE. (B) INTERFERENCE PATTERN ON THE DEFLECTED MEMBRANE DURING BULGING MEASUREMENT. (C) SEM IMAGE OF THE FREELY SUSPENDED NANOMEMBRANE BEFORE AND (D) AFTER BULGING MEASUREMENTS (THE MEMBRANE IS FRACTURED)..... 82

FIGURE 21: (A) DEPENDENCE OF THE YOUNG'S MODULUS OF THE GO–SILK FIBROIN NANOMEMBRANES UPON THE VOLUME CONCENTRATION OF GO. (B) SIGMOID DECAY CURVES FOR BULGING TESTS AT THE INTERPHASE REGION. (C) DEPENDENCE OF THE EFFECTIVE YOUNG'S MODULUS OF THE SILK LAYER ON THE THICKNESS OF THE SILK FIBROIN LAMINATES. THE DASHED LINE IS THE FITTED CURVE USING THE INTERPHASE REINFORCEMENT MODEL. (D) VARIATION OF THE YOUNG'S MODULUS FOR MEMBRANES WITH DIFFERENT THICKNESSES. 83

FIGURE 22: (A) REPRESENTATIVE STRESS–STRAIN CURVES DERIVED FROM THE BULGING TESTS AND (B) THE ULTIMATE STRAIN, (C) THE ULTIMATE STRESS, AND (D) THE TOUGHNESS AS A FUNCTION OF THE GO CONCENTRATION FOR GO–SILK FIBROIN NANOCOMPOSITE MEMBRANES FABRICATED HERE AS COMPARED TO THE VALUES FOR THE CONVENTIONAL SA-LBL MEMBRANES.124 84

FIGURE 23. AFM TOPOGRAPHICAL IMAGES OF SUCKERIN-12 AT 1 WT.% WHEN DROP CAST (A) AND SPUN CAST (B) AS WELL AS SPIN CAST SUCKERIN-12 AT 3 WT.% (C) WITH AN INSET (D) TO SHOW SURFACE MODULATIONS. SCALE: 1 UM (A, B, D) AND 4 UM (C). Z RANGE: 5 NM (A AND B), 52 NM (C), AND 40 NM (D). 89

FIGURE 24. ATR-FTIR AND CD SPECTRA OF DROP (A) AND SPUN CAST (B) SUCKERIN-12 WHERE SUBPEAKS ARE SHOULD UNDER THE OVERALL CONVOLUTED AMIDE 1 PEAK TO

SHOW HOW FTIR SPECTRA WERE ANALYZED FOR THIS STUDY. THE SECONDARY STRUCTURE IN EACH SAMPLE CALCULATED FROM PEAK AREA OF THEIR RESPECTIVE PEAKS IS GIVEN IN (C). CIRCULAR DICHROISM WAS CONDUCTED TO CORROBORATE THE ATR-FTIR SPECTRA (D). 91

FIGURE 25. AFM TOPOGRAPHICAL IMAGES OF 1 WT.% SUCKERIN-12 BEFORE (A) AND AFTER (B) TVA FOR 12 H. SCALE: 200 NM. Z RANGE: 4 NM. 92

FIGURE 26: ATR-FTIR SPECTRA OF CROSSLINKED SUCKERIN-12 FILMS IN THE AMIDE 1 REGION BEFORE AND AFTER TVA (A) AND SECONDARY STRUCTURE COMPOSITION IN INITIAL FILM AND AFTER ANNEALING (B). 93

FIGURE 27. HISTOGRAM OF FDS MEASURED MODULI FOR DROP AND SPIN CAST SUCKERIN-12 FILMS AFTER THERMAL VAPOR ANNEALING. 94

FIGURE 28. AFM TOPOGRAPHICAL IMAGES OF 3 WT.% SUCKERIN-12 AFTER SALT ANNEALING FOR 1 HR WITH SODIUM PHOSPHATE (A), SODIUM ACETATE (B), SODIUM CITRATE (C), AND SODIUM SULFATE (D). SCALE: 1 UM. Z RANGE: 33 NM (A), 38 NM (B), 30 NM (C), AND 36 NM (D). 95

FIGURE 29. ATR-FTIR OF THE AMIDE 1 PEAK OF SUCKERIN-12 NEAT AND AFTER SALT ANNEALING FOR 1 HR (A) AS WELL AS A GRAPH OF THE SECONDARY STRUCTURE COMPOSITION DERIVED FROM DECONVOLUTION OF THE SPECTRA (B) 96

FIGURE 30. AFM TOPOGRAPHICAL IMAGES OF SALT ANNEALED 3 WT.% SUCKERIN-12 FILMS BEFORE (A, C, E, G) AND AFTER (B, D, F, H) IMMERSION IN WATER. THE SAMPLES SHOWN WERE NEAT (A, B) AND ANNEALED WITH SODIUM PHOSPHATE (C, D), SODIUM ACETATE (E, F), SODIUM CITRATE (G, H), AND SODIUM SULFATE (I, J). SCALE: 1 UM. Z RANGE: 20 NM (A-H). 97

FIGURE 31. ATR-FTIR SPECTRA OF THE AMIDE 1 PEAK OF SUCKERIN-12 BEFORE AND AFTER CROSSLINKING (A) AS WELL AS GRAPH OF THE SECONDARY STRUCTURE COMPOSITION DERIVED FROM PEAK DECONVOLUTION (B) 98

FIGURE 32. AFM TOPOGRAPHICAL IMAGES OF CROSSLINKED 3 WT% SUCKERIN-12 AFTER SALT ANNEALING FOR 1 HR WITH NA3PO4 (A), NAOAC (B), NA3C6H8O7 (C), AND NA2SO4 (D). SCALE: 1 UM. Z RANGE: 35 NM (A), 38 NM (B, D), AND 44 NM (C). 99

FIGURE 33. ATR-FTIR SPECTRA OF THE AMIDE 1 OF CROSSLINKED SUCKERIN-12 BEFORE AND AFTER SALT ANNEALING (A) AS WELL AS THE SECONDARY STRUCTURE COMPOSITION DERIVED FROM PEAK DECONVOLUTION (B). 100

FIGURE 34. QNM IMAGES OF SUCKEIRN-12 DRY BEFORE (A, C, E) AND AFTER (B, D, F) CROSSLINKING WHERE HEIGHT (A,B), MODULUS (C, D), AND ADHESION (E, F) MAPS ARE SHOWN. 102

FIGURE 35. HISTOGRAMS OF FDS MEASURED MODULI FOR SUCKERIN-12 FILMS BEFORE (A) AND AFTER (B) CROSSLINKING. 103

FIGURE 36. HIGH RESOLUTION C1S XPS SCANS: (A) PRISTINE GO AND (B) GO/RMS-2. 107

FIGURE 37: AFM TOPOGRAPHICAL (A) AND PHASE (B) IMAGES OF GRAPHENE FLAKES MODIFIED WITH COPOLYMER TYPE 2 IN WATER AS WELL AS HEIGHT PROFILES (D) TAKEN FROM AN AFM TOPOGRAPHICAL IMAGE OF GRAPHENE FLAKES MODIFIED WITH COPOLYMER TYPE 1 (C) WITH PROFILE SLICES COLOR COORDINATED. 108

FIGURE 38: ATR-FTIR SPECTRA OF GO, GO MODIFIED WITH COPOLYMER TYPE 1 AND TYPE 2..... 108

FIGURE 39: TOPOGRAPHICAL (A,B) AND PHASE (C,D) IMAGES FROM IN AIR AFM GRAPHENE FLAKES MODIFIED WITH COPOLYMER TYPE 1 (A,C) AND TYPE 2 (B,D), INCLUDING AN INSET OF C SHOWING COPOLYMER EXTENSION (E). HEIGHT PROFILES TAKEN AT THE FLAKE IMAGE ARE PROVIDED TO INDICATE FLAKE THICKNESS POST GRAFTING. 110

FIGURE 40. AFM HEIGHT (A, C)AND PHASE (B, D) IMAGES OF COPOLYMER TYPE 1 (A, B) AND TYPE 2 (C, D) ON GO FLAKES ON SIO2 WAFERS. Z RANGE: 9 (A, C). ANGLE RANGE: 25O (B) AND 17O(E). 112

FIGURE 41. SILK FIBROIN AT 0.002 WT. % DYNAMICALLY CAST ON GO FLAKES AT 5000 RPM MORPHOLOGY IN AFM HEIGHT (A) AND PHASE (B) IMAGES WITH HEIGHT PROFILES CORRESPONDING TO THE WHITE (C), RED, GREEN, AND BLUE LINES (D) IN A. SCALE: 100 NM. Z RANGE: 2 NM. 122

FIGURE 42. SILK FIBROIN AT 0.002 WT. % DEPOSITED VIA CONVENTIONAL SA-LBL ON GO FLAKES AT 5000 RPM MORPHOLOGY IN AFM HEIGHT (A) WITH HEIGHT PROFILES CORRESPONDING TO THE RED, GREEN, AND BLUE LINES (B) IN A. SCALE: 100 NM. Z RANGE: 10 NM. 122

FIGURE 43. ATR-FTIR SPECTRA OF SILK FIBROIN (A) ON GO (B) AND RGO (C) IN THE AMIDE I AND AMIDE II REGIONS. 123

FIGURE 44. SEQUENCE OF *BOMBYX MORI* HEAVY CHAIN WITH 258-AMINO ACID SEGMENT USED IN MD. SIMULATION 123

FIGURE 45. XPS OF RGO CARBON PEAK FOR HYDRAZINE SOLUTION (A) AND VAPOR REDUCTION METHODS (B). 123

FIGURE 46. THE AFM TOPOGRAPHICAL IMAGE OF FIGURE 1B IS USED AS AN ADDITIONAL EXAMPLE OF CROSS-SECTIONS USED FOR HEIGHT MEASUREMENT, WHERE THE HEIGHT PROFILES CORRESPOND TO THE BLUE (B), RED (C), AND GREEN (D) IN A. SCALE: 100 NM. Z RANGE: 5 NM 124

FIGURE 47. HISTOGRAM OF SILK FIBROIN STRUCTURE HEIGHT WHEN CAST BY CONVENTIONAL SA-LBL AT 5000 RPM. THE DATA PRESENTED IS DIRECTLY TAKEN FROM THE IMAGES SHOWN IN FIGURE 7 124

FIGURE 48. HISTOGRAM OF SILK FIBROIN STRUCTURE VOLUME WHEN CAST BY CONVENTIONAL SA-LBL AT 5000 RPM. THE DATA PRESENTED IS DIRECTLY TAKEN FROM THE IMAGES SHOWN IN FIGURE 7 125

FIGURE 49. RAMACHANDRAN PLOT WITH THE PROBABILITY (*I*) OF SILK ON (A) GRAPHENE, (B) GO, (C) SIO2, AND (D) FREE STANDING WHERE RED INDICATES GREATER DENSITY. 125

FIGURE 50. REPRESENTATIVE STRESS–STRAIN CURVES DERIVED FROM THE BULGING TESTS FOR DSA GO-SILK FIBROIN NANOCOMPOSITE MEMBRANES WITH DIFFERENT GO CONTENT. (A) 23.7% (B) 18.4% (C) 11.1% (D) 8.75% (E) 5.1% (F) 0%. EACH SAMPLE WITH THREE DIFFERENT TEST POINTS USED FOR COMPARISON..... 127

FIGURE 51. PHASE IMAGE OF SUCKERIN-12 AT 3 WT.% ON A SILICA SUBSTRATE..... 128

FIGURE 52. OPTICAL MICROSCOPY IMAGES OF THE POLYSTYRENE PRE-LAYER IN BRIGHT (A) AND DARK FIELD (B) AND SUCKERIN-12 ON POLYSTYRENE UNDER BRIGHT (C) AND DARK FIELD (D). 128

FIGURE 53. BAR GRAPH OF SUCKERIN-12 FILM HEIGHTS BEFORE AND AFTER SALT ANNEALING AS WELL AS THE PERCENT CHANGE. 129

FIGURE 54. XPS CARBON PEAK FOR NEAT, SALT TREATED, AND CROSSLINKED SUCKERIN-12. 130

FIGURE 55. XPS CARBON PEAK COMPOSITION TAKEN FROM DECONVOLUTING FOR COMMON HYBRIDIZATION PEAKS..... 130

LIST OF SYMBOLS AND ABBREVIATIONS

AFM	Atomic force microscopy
Ala (A)	Alanine
Arg (R)	Arginine
Asp (N)	Asparagine
ATR	Attenuated total reflectance
Cis (C)	Cysteine
dSA-LbL	Dynamic spin assisted layer-by-layer
FDS	Force distance spectroscopy
Phe (F)	Phenylalanine
FTIR	Fourier transform infrared spectroscopy
GMA	Glycidal methacrylate
Glu (Q)	Glutamine
Gly (G)	Glycine
GO	Graphene oxide
His (H)	Histidine

H2O2	Hydrogen peroxide
HRP	Horseradish peroxidase
Iso (I)	Isoleucine
rGO	Reduced GO
LMA	Lauryl methacrylate
Leu (L)	Leucine
Lys (K)	Lysine
MEK	Methyl ethyl ketone
Met (M)	Methionine
N2H2	Hydrazine
OEGMA	Oligo (ethylene glycol) methyl ether methacrylate
POEGMA	Poly(OEGMA)
Pro (P)	Proline
SA-LbL	Spin assisted layer by layer
Ser (S)	Serine
SPM	Scanning probe microscopy
SiO2	Silicon dioxide

Thr (T)	Threonine
Try (W)	Tryptophan
Tyr (Y)	Tyrosine
QNM	Quantum nanomechanical mapping
Val (V)	Valine
XRD	X-ray diffraction
XPS	X-ray photoelectron microscopy

SUMMARY

Protein biopolymer composites bring together the tunability and flexibility of protein matrices and functionality of filler components. Graphene-based biocomposites are particularly popular for design of aqueously processible and strong flexible electronics for sensing, nanowires, and semiconductors. However, a lot of trial and error is required to determine biopolymer and co-constituent chemistry as well as the assembly process needed to capitalize on their synergistic properties. This dissertation identifies non-covalent methods to control interfacial interactions that drive and stabilize assembly of silk fibroin from *Bombyx mori* silkworm cocoons in order to induce mechanical reinforcement. This work, then shows the cross-applicability of assembly triggers for silk with other semi-crystalline, amphiphilic biopolymers using Humbolt squid sucker ring teeth protein suckerin. And, lastly, synthetic copolymers are used to clarify the role of biopolymer and surface properties on interfacial assembly without post-processing treatments.

The main drivers of assembly and interfacial binding studied here include temperature, shear force, hydropathy, and pH. Surface topography and polymer chemistry/conformation were studied concurrently via atomic force microscopy (AFM) and Fourier transform infrared spectroscopy (FTIR). This data was supported by simulation to better define assembly mechanisms at the interface of biopolymers and inorganic 2D fillers and their timescales. Then, mechanical characterization via bulging tests and scanning probe microscopy methods (SPM), force distance spectroscopy (FDS) and quantitative nanomechanical mapping (QNM). Mechanical performance is evaluated at the macro and nanoscales using quantitative nanomechanical mapping, FDS, and buckling tests. Overall, this dissertation shows how interfacial assembly driven by the hydrophobic effect can be manipulated using non-covalent means to study to tune mechanical performance. Thus, this work a roadmap for further optimization of biopolymer-based nanocomposites through interface-minded design.

INTRODUCTION

1.1 Background

Nanocomposites synergistically combine the strength and functionality of constituent materials to yield nanomaterials with enhanced utility and minimal added weight and cost. High surface to volume ratio confers upon nanomaterials exceptional mechanical, electrical and optical properties not seen in bulk materials.1 Nanomaterials can possess mechanical, electrical, thermal, and optical properties of use for many applications. This array of unique capabilities which can be tuned through variations in processing offers an opportunity to create devices that are not only strong and flexible but that better assure mission success through chemical sensing, actuating constructs, and smart-shielding such as gas, moisture and radiation barriers.2,3,4,5 However, recent developments are nearing the limit of bionanocomposite strength and flexibility.

Fortunately, nature offers innovative designs and robust building blocks with which to construct the next generation of functional nanomaterials. In particular, evolution has endowed natural materials with mechanisms to protect them from various environmental hazards and predators as well as facilitate their day-to-day activities. For example, silk worms and spiders extrude silk fibers with elastic modulus that rival the strongest commercial polymers thanks to their hierarchical design.12 Silk worms then use these fibers to construct cocoons for their gestation which not only keeps out predators and protects them from changes in their environment but blocks out solar radiation which could be detrimental to the developing pupae within.6 These properties have made silk fibroin a popular platform for drug delivery and matrix for flexible nanocomposites constituent.7,8,9 However, silk has poor thermal and chemical stability limit utilization of silk fibroin. Understanding the mechanisms and design features which yield these extraordinary properties enables more effective application of biopolymer in nanocomposite design.

The biggest take away from nature is the importance of hierarchical assembly. Nature commonly uses hierarchical assembly to impart strength and dexterity in natural materials whether a macromolecule like keratin and collagen or mineral-based structures like bone and nacre.10,11 In addition to their mechanical properties, natural materials are sustainable, biocompatible, aqueously processible and bio-available. Many species of plant and animal life produce comparably intriguing materials that can both add to one's arsenal of materials as well as suggest new ways to apply them.

Bio-derived polymeric materials of interest to the broader community and that will be addressed in this dissertation include silk from *Bombyx mori* silkworm cocoons and silk-like protein suckerin from Humboldt squid sucker ring teeth. Lessons from silk and suckerin are applied to investigate the assembly behavior of hydrophobic and hydrophilic synthetic copolymer brushes with controlled configuration. Studying each macromolecule will showcase a different aspect of the relationship between structure, process, and performance at the bio-inorganic interface.

1.1.1 Silk fibroin

Natural silks are fibrous proteins produced by arthropods that exhibit high extensibility and toughness comparable to steel and Kevlar.12,13,14 Under ambient conditions, arthropods like silkworms and spiders produce these exceptionally strong fibers wherein fibers contain fibroin comprised of many fibroin fibrils of silk molecules incased in hydrophilic, gumming protein sericin.14,15 The silk backbones consist of alternating hydrophobic heavy chain that tends to form hydrogen bonded anti-parallel β-sheet crystals and hydrophilic light chain that forms amorphous random coils and α-helices.15 Though different types of silks possess similar chemical design, their particular chain length and amino acid sequence might differ significantly depending on the source and function. Specifically, *Bombyx mori* silk used to construct silkworm cocoons contains Gly/Ala-rich heavy chain of approximately 390 kDa and Gly/Tyr-rich light chain of approximately 25 kDa joined by disulfide bonds.12,13,15,16 The exceptional mechanical properties conferred by

this hierarchical design, biocompatibility, and biodegradability make the protein a promising material for biomedical and engineering applications.

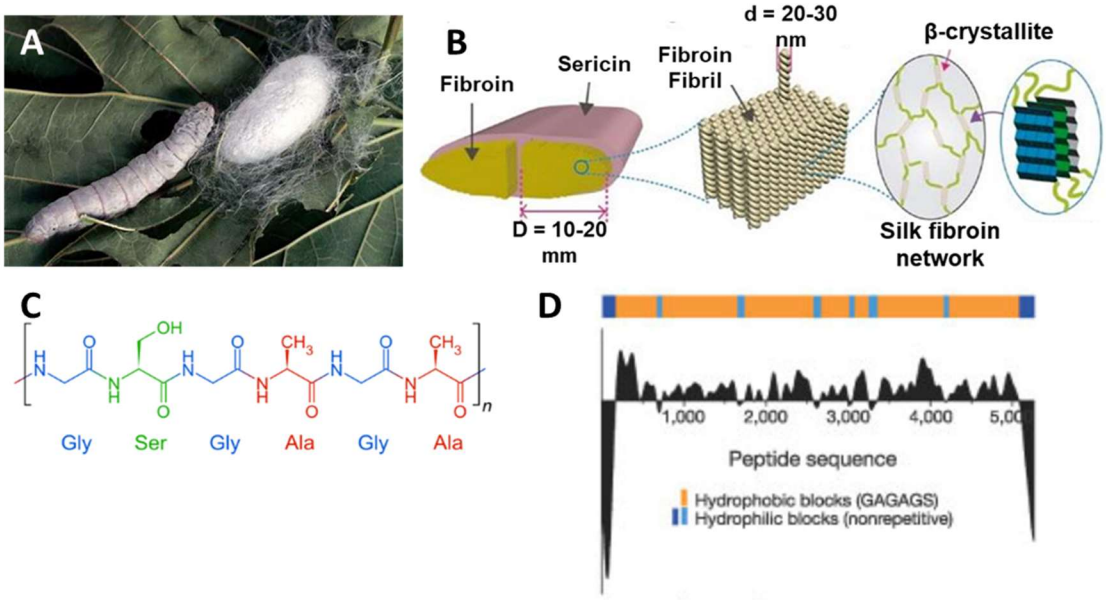

Figure 1: (A) *Bombyx mori* silkworm pictured beside its cocoon. Scaling down to the molecular level, each fiber in the cocoon has the hierarchical structure outlined in (B).26 Each of these fibers consists of mostly hexapeptides with structures like that in (C) which are interspersed with amorphous regimes as shown in (D).7

However, silk in aqueous suspension, reconstituted silk commonly used in composites lacks hierarchical structure and has inferior mechanical properties to raw silk.17,18 Thus, treatments and processing steps are used to store the assemblies and intra-silk interactions that make silk great. Silk toughness and tensile strength can be tuned using chemical modification, solvent and water annealing to alter hydrogen bonding and ion pairing.19,20,21 Surface chemistry may also be used to initiate silk structural changes. For example, silk interacts electrostatically with functional groups sticking out from graphene oxide (GO) surfaces that prevent the direct interactions between silk and underlying hydrophobic aromatic six-membered rings, leading to good structure retention in silk.22 The balance of electrostatic and van der Waals interactions contributes to secondary structure stability as van der Waals interactions can disrupt ordered secondary structure.22

Numerous studies have shown silk's potential utilities in a host of applications including hydrogel particles, core-shell particles, tissue scaffolds, and, in particular, nanocomposites.[7,23,24,25,26,27,28,29] The highly elastomeric natural biomaterial enables effective load transfer between reinforcing and functional fillers through an array of hydrophobic, van der Waals, electrostatic, and hydrogen bonding interactions.[30,31,32] For example, silk fibroin preserves therapeutic agent functionality and enables sustained, stimuli responsive release in hydrogel.[7,23,24,25,26,27] Stem cells may also be embedded in scaffolds to encourage tissue regeneration.[28,29] And, whether for biomedical or energy storage applications, silk based composites are utilized to create materials with mechanical, degradation, thermal, and optical properties most suitable for a given application.

Despite their premium properties and vast applicability, silk-based materials have their limitations. Silk is a soft biomaterial with little functional utility, like electrical conductivity, whose mechanical properties, though strong, pale in comparison to synthetic materials like graphenes. Generally, silk materials serve as a matrix for reactive and functional components with a variety of inorganic or carbon components.[9] Carbonaceous additives such as graphene and carbon nanotubes provide greater mechanical strength to the composite and electrical properties necessary for sensing and energy storage devices while the elastomeric biomaterial matrix can confer flexibility and biocompatibility.[9,30,31,33]

1.1.2 Suckerin

Plants, insect, and crustaceans have produced some of the most popular natural materials including cellulose, silk, and chitin; which gained brought utilization due to their mechanical tunability, susceptibility to chemical modification, and bio-abundance.[20,2134] Specifically, cephalopods offer a wealth of materials design inspiration from their ability to seamlessly alter the size and pigmentation of spots on their skin to their problem-solving capabilities. Mechanically, they have

some of the strongest beaks and limb grips available thanks to adeptly designed biomacromolecule composites and blends.35 The beaks derive strength from a mixture of hydrated chitin and glycine- (Gly, G) and hisitidine- (His, H) rich proteins.43 Chitin forms a supramolecular network reinforced by β-sheets in an amorphous matrix. Lessons afforded by the examination of this piece of anatomy and pure chitin have wrought films, gels, and flame-retardant matrices.36,37,38 The impressive grip comes from their physiologically strong soft tissue and aided by hard polymeric extra-cellular tissue called sucker ring teeth within their soft tissue suckers that function as grappling hooks for hunting and defense. The materially more impressive aspect of their sucker ring teeth that exhibit an elastic modulus of 6–8 GPa in the dry state and 2–4 GPa when hydrated and are comprised of suckerin proteins.39 Suckerin is a family of proteins produced by cephalopods in up to 35 different isoforms with each having different molecular weight and modular amino acid sequence with 20-90% sequence similarity across species.40 Traditionally, nature uses covalent crosslinks, metal-coordination, or the infusion of minerals to form stiff structures like sucker ring teeth. Interestingly, sucker ring teeth are solely comprised of suckerin isoforms bound by hydrogen-bonding and hydrophobic interactions and exhibit compressive and tensile strength that rivals synthetic polymers full polyethylene ethyl ketone, polymethyl methacrylate, and polyacrylamides.41

Despite their modular composition, suckerins have a few common features much like silk fibroin which differs between species but has a conserved block copolymer like structure of repetitive hydrophobic, crystalline segments amongst hydrophobic, disordered amorphous segments. Suckerin is a globular protein with Alanine- (Ala, A), threonine- (Thr, T), and His-rich nanoconfined β-sheets in a Gly-, leucine- (Leu, L), and tyrosine- (Tyr, Y) rich amorphous phase (Figure 2).42,43,44,45 The Ala-, His-rich segment exhibits strongest like-peptide interactions, which are pH dependent. This is like major ampullae spidroin from spiders that has a well-conserved polyalanine amino acid sequence that readily forms homo-peptidic bonds to form β-sheets.46 For suckerin, His provides supplemental pH-dependent support. When near neutral pH,

the His can deprotonate, imparting more aromatic character on its imidazole which can then facilitate π-π stacking. Thus, in mixing alanine and histidine, suckerin can form β-sheets and larger crystalline supramolecular complexes like β-strands. The amorphous segment consists of repetitive tripeptides of GGY and GYG as well as tetrapeptide GGLY and non-repetitive portions.

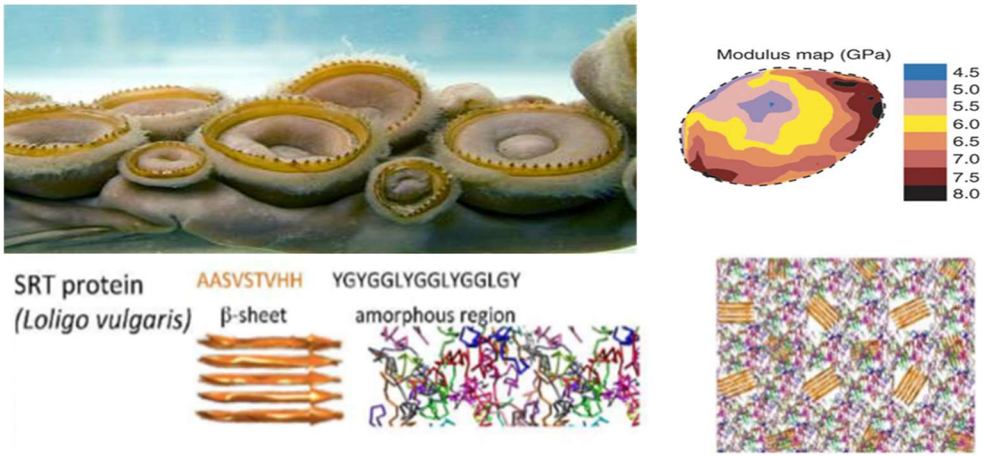

Figure 2: Schematic of sucker ring teeth (A), the many suckerin isoforms in sucker ring teeth (B) 44, and the amino acid sequence and secondary structures that primarily comprise suckerin (C).45

Unlike silk with β-crystallites nanoconfined between amorphous segments to confer a tough fibrillar morphology, suckerin has a semi-crystalline structure of anisotropic β-crystallites. The semi-crystalline composition confers tensile and shear strength while anisotropic alignment contributes to generally, globular morphology and overall high compressive stress (Figure 2).42,43,44,45 Then, several isoforms co-assemble into rings of teeth with nanotubular microstructure. The isoforms range in size from 5 – 57 kDa, much shorter than most fiber-forming, stiff natural proteins. Each isoform has distinct properties that require exploration. So far, most research has focused on the largest isoform that primarily found in the Humboldt squid suckerin-19, also known as suckerin-39. Suckerin-19 is 39 kDa and the primary component of Humboldt squid sucker ring teeth. Numerous studies have explored the materials structure, properties, and performance of suckerin-19 in a variety of environmental and solvent conditions. In short, recombinant suckerin-19 has elastic modulus of 7.5 GPa when dry, 5-8 MPa when hydrated, and

as low as 20 MPa when immersed in select solvents like urea that disrupt intermolecular hydrogen bonds, which is comparable to dragline silk.44 When photo-crosslinked using ruthenium and ammonium persulfate, researchers found that increased loading of the initiator APS increased disorder in suckerin and lead to decreased elastic modulus when crosslinked (2-0.038 GPa, depending on the concentration of APS). The results illustrate the complex effect of pH and mobility on suckerin secondary and tertiary structure orientation. In presence of higher pKa materials that can deprotonate histidine or tyrosine, suckerin becomes more disordered, thereby decreasing the assembly that imbues it strength. And, decreased mobility from crosslinks restricts suckerin's ability to transform into more crystalline organization, once again inhibiting elastomeric mechanical performance.

Altogether, suckerin is a bio-available, synthetically producible, strong biopolymer that can be processed for a variety of applications from hydrogels for drug transport to films with pH tunable toughness and dimensions. Even in the infancy of its materials research, suckerin is marketed a rival to silk, so we sought to test this assertion as well as conduct a higher resolution analysis of the recently reported Hofmeister effect on suckerin. In fact, it has been demonstrated that three-dimensional suckerin-12 hydrogels exhibit sclerotization and dimensional changes upon exposure to Hofmeister series salts according to their pKa and rank in the series. 47 The Hofmeister salts are categorized as kosmotropes (common anions: acetate (C2H3O2-1), citrate (C6H5O7-3), phosphate (PO4-3) and sulfate (SO4-2); cations: lithium (Li+), sodium (Na+) , potassium (K+), and ammonium (NH+4)) that promote aggregation in water and chaotropes (common anions: chloride (Cl-), nitrate (NO-3), chlorate (ClO-3), iodide (I-), hypochlorate (ClO-4), and cyanate (SCN-); cations: magnesium (Mg+2), calcium (Ca+2), and guanidinium (C2H6N4S+)) that promote dissolution.

There is no evidence that suckerin is covalently crosslinked in the native SRT assembly.44 Therefore, the mechanical properties and assembly of suckerin are likely controlled by modulation

of secondary structure and self-assembly into organized nanostructures. We hypothesize that suckerin assembles in a manner similar to silkworm fibers where the local chemical environment and the mobilization of bulk water drive inter-proteins interactions to create a robust water stable biomaterial.

1.1.3 Synthetic copolymers

Although, hierarchical structure and bioavailability make natural biopolymer exciting, their complexity does not allow for close examination of the effect their configuration has on interfacial interactions. For natural proteins, their amino acid sequence tends to vary between and within species. *Bombyx mori* silk quality is affected by the feed and environment enjoyed by the silkworms producing and extruding the fibers. One could even feed them leaves coated in quantum dots to produce silk interlaced with the particles. In spiders, silk strength also differs according to its purpose and is extruded from different spinnerets. More differences abound among the many other silks produced by other insects. The same is true for suckerin, which is found in many cephalopod species. While little research addresses the effect of environment and nutrition on suckerin, it does have 35 isoforms; some of which aren't found in every species but work synergistically to form a tough protein-blend grappling hook.

This complexity is surmounted in device and film making through sourcing consistency and solubilization procedures designed to reduce the proteins to consistent dimensions and remove additives like sericin, or—as for suckerin—expression via e. coli. Still, these approaches insufficiently reduce the complexity of natural polymers. Synthesis allows for control of polymer degree of polymerization, functional groups, and grafting density as well as hydrophilicity. Similarly, peptides can be synthesized with specific amino acid sequences, but it is difficult to make large molecules (<100 kDa) and in high volume. Synthetic polymers aren't as limited. Homopolymers like polystyrene (PS), polymethylmethacrylate (PMMA), and polyethylene glycol

(PEG) are commonly used in nanomemebrane and biologic fabrication. PS is a hydrophobic polymer that readily dissolves in toluene and serves as a sacrificial layer for lifting membranes from the surface on which they were assembled. PMMA and PEG are hydrophilic polymers found in electronics, plexiglass, cosmetics and medicines.48 PEG has non-ionic hydrophilicity that is thermoresponsive, is flexible without crystal formation, and attracts metal cations. Due to their tunable hydrophilicity and biocompatibility, PEG serve as antifouling coatings that prevent cell and protein adsorption.49,50 They also serve as surfactants for proteins and encourage higher-order assembly formation.51 PMMA is an anionicly hydrophilic, transparent thermoplastic polymer best known as Plexiglass and has tensile strength, impact strength, chemical and heat resistance. Industrially, PMMA is used in industrial paints, tattoo ink, and semiconductors. Like PEG, PMMA is relatively bio-inert and prevents formation of fibrotic tissue that can lead to bio-device failure.52 Thanks to this biocompatibility and shatter-resistance, PMMA bio-related applications include intraocular lenses, eyeglasses, bone cement, soft tissue filler, and dental prosthetics. 53,54,55

Copolymerization enables mediation of their fouling properties and hydrophilicity. A copolymer is a polymer comprised of two or more different kinds of mer units. There are several kinds of copolymers; block copolymers – multiple polymer segments joined linearly, star polymers – polymers joined at a central nexus point, and graft copolymers – polymers attached as functional chains along a backbone. Ideally, copolymers combine the beneficial properties of individual polymers for singular applications like acrylonitrile butadiene styrene for rubber and PEG-poly(propylene oxide) for amphiphilic coatings and surfactants. Graft and block copolymers are largely synthesized via living and ring-opening metathesis polymerization. Their properties are largely due to the composition and length of the blocks. So, their tailor-made chemical structure and high throughput producibility make copolymers especially useful for study of polymer-surface interactions driven by composition and hydrophobicity.

Two copolymers were chosen for this study. Copolymer type I contains glycidyl methacrylate (GMA) grafted to a backbone of oligo (ethylene glycol) methyl ether methacrylate (OEGMA) and demonstrates strong hydrophilic nature while copolymer type 2 shows amphiphilic behavior due to lauryl methacrylate (LMA) side chains interspersed with GMA son an OEGMA backbone. Poly(oligo(ethylene glycol) methyl ether methacrylate) (POEGMA) exhibits thermosensitivity, protein repellency, and ability to compatibilize materials with water.[56,57,58,59,60,61,62] It has hydrophobic oligo(ethylene glycol) side moieties tethered to a hydrophilic methacrylate backbone. Poly(glycidyl methacrylate) (PGMA), which is insoluble in water, can be easily "grafted to" surfaces by nucleophilic addition to its epoxy groups. This also facilitates PGMA thermal crosslinking.[63,64,65,66,67,68,69,70,71] Lauryl methacrylate addition is used to tune the hydropathy of the copolymers.[72,73,74]

1.1.4 Graphene

Altogether, biopolymers exhibit mechanical properties comparable to high performance polymers (i.e. Kevlar and PEEK), but their functions are relatively limited to matrix or binding functions. On the other hand, graphene is a 2D platelet that possesses the biocompatibility and facile processability of the best biopolymers as well as high thermal and electrical conductivity and mechanical strength. This is thanks to their honeycomb carbon lattice structure that exhibits strong interlayer π-π stacking of unique monolayer flexible sheets.[33] Graphene is produced via chemical vapor deposition, exfoliation, and many other methods; but most commonly via exfoliation of graphitic flakes. Most commonly, graphene is obtained from chemical or thermally oxidized graphitic flakes that are then reduced to graphene. The intermediary product in this process is GO. The oxygenated moieties formed force the flakes to separate into few to single atomic layer sheets hydroxyl, epoxy, and carboxyl groups during oxidation enables dissolution in water and facile, green processing with other materials. Theoretically, GO is about 0.72 nm thick, twice the thickness of pristine graphene because of the surface functionalities. A single GO flake can have an elastic

modulus of 250 GPa, and they tend to be amphiphilic due to their hydrophilic oxygen containing side groups and hydrophobic carbon lattice. Their lateral dimensions are highly dependent upon the oxidative process applied and the dimensions of the graphitic flakes used to make them.

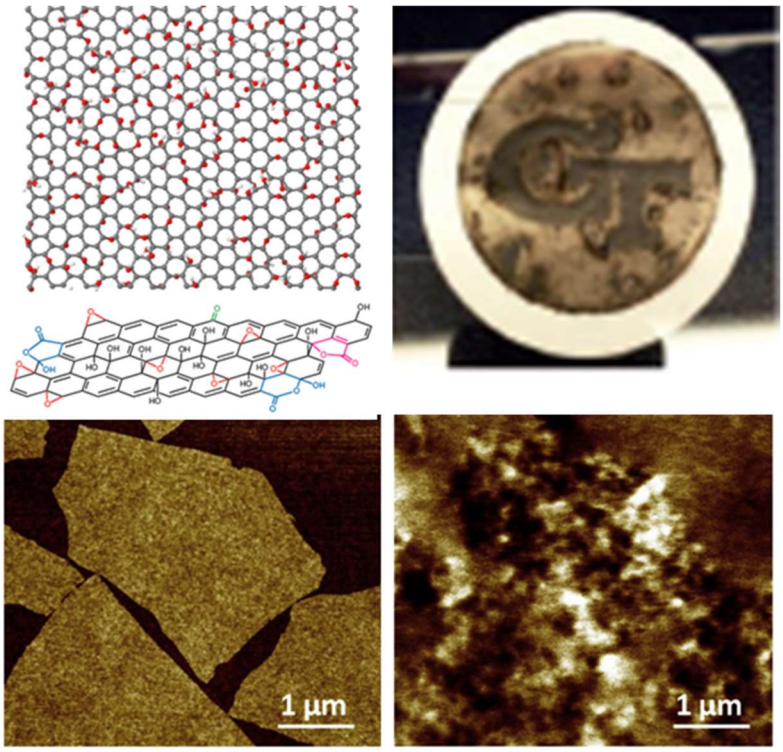

Figure 3. A depiction of the GO honeycomb structure, a nanomembrane of silk and GO, AFM image of GO on silica, and electrostatic force microscopy image showing the oxygenation of the GO surface.

Flakes exfoliated and chemically oxidized via modified Hummer's method can reach 60-70% oxidation and 2:1 carbon to oxygen ratio. However, the heat generated during this process leads to defects in the lattice that disrupt the π-π interactions that confer them strength and functionality. Defects coupled with the oxygenated functional groups make GO less thermally and electrically conductive than graphene. Then, it is reduced to restore electrically performance and, in the process, form more defects, so graphene-derivatives rarely achieve the performance seen with pristine graphene.

All the same, GO possesses amphiphilicity that allows it to strongly bind to both polar and non-polar species with optimal interfacial binding in an amphiphilic matrix like silk fibroin.75 GO can also be aqueously dispersed with water forming local cross-links between the GO flakes via hydrogen bonding while decreasing load transfer through inter-layer slip, and permanent interlocks formed by covalent cross-linkers increase reinforcement and limit flexibility.16 Once oxidized, the oxygen containing moieties can be used to functionalize GO for flame retardance, analyte binding, and macromolecules of different sizes and compositions. Chemical modification allows for incorporation of graphenes into a variety of media whether homophobic or hydrophilic and for different sensing and electrical applications. Even, when not functionalized, the amphiphilicity, strength, conductivity, and processability of GO have made a popular 2D filler in nanocomposites.

GO-based nanocomposites are typically assembled as stacks of flexible GO monolayers of about 1 nm thickness via vacuum filtration, layer-by-layer (LbL) assembly, and controlled evaporation.32 Of these methods, LbL assembly mimics the laminated design of nacre thus enabling greater interfacial contact between the natural biopolymer matrix and synthetic filler component.9,30,31,32 This fabrication method enables silk to saturate interfacial interactions and dramatically enhance mechanical properties of these nanocomposites.9,76,77,78 Increased interfacial binding between silk fibroin materials and GO components facilitates higher Young's modulus and the ultimate stress.

MD simulations show that van der Waals and hydrophobic interactions as well as π–π stacking play a major role in the adsorption of peptides and proteins to graphene-derived surfaces.79,80,81,82 The graphitic surface hydrophobicity and, possibly, its heterogeneity affect peptide conformations and secondary structure.83,84 In a study of short alpha-helical, positively charged cytoplasmic peptides on graphene (hydrophobic, homogenous atomically flat surface) and GO (heterogeneous, hydrophilic surface), adsorption on the GO surface was mediated through hydrogen bonds and the alpha-helical protein exhibited better conformational stability on GO as

compared to graphene.85 Similar results were obtained in a study of glycine-alanine protein adsorption to GO and graphene surfaces, where the protein retained a crystalline secondary structure on GO rather than graphene.86 These simulations suggest general mechanisms for peptide/protein adsorption on carbonaceous surfaces, however, there's lack of similar experimental studies.

1.2 Fundamental Issues

A lot of research on bionanocomposites focuses on integration of a few biopolymers (silk, collagen, DNA, keratin) into hybrid organic-inorganic composite structures. This is mostly due to the decades of use and experimentation on these materials for use in food, textiles, and medical devices. Oftentimes, these biopolymer composites were designed using an iterative trial and error approach. This approach has brought us silk-based hydrogels, core shell particles, and flexible films that take advantage of silk's electrostatic, van der Waals, and hydrogen bonding interactions to yield stability, responsive properties, and strength. However, silk-based composites that have high Young's modulus tend to exhibit low ultimate strain, which makes them brittle and unsuitable for applications where flexibility is required.32,87 Effective compatibilization is even worse for lesser studied biopolymers like suckerin.

Creating next generation bionanocomposites necessitates a different approach to design driven by fundamental understanding of the composite co-constituent assembly behavior and how this relates to their performance properties such as mechanical strength, opacity, and adhesion. Say that a protein is more likely to coil on itself at neutral pH and extend to bond with surface moieties on a nanoparticle at low pH. By applying this fundamental understanding of how the protein behaves at different pH, one can construct a fabrication approach that applies this phenomenon to ensure formation of a percolating network to facilitate stress, heat or electron transfer, depending on the

application and nanoparticle used. In a recent publication, for instance, electrostatic interactions between silk and cellulose were used to create nanofibers of cellulose nanocrystals coated in silk that bonds strongly to GO.88 Researchers applied a fundamental knowledge of interaction at the silk-GO and silk-CNS interfaces to create a durable, composite system. Then, upon reducing the GO, the hydroscopic nature of CNC enabled facile tunability while reduced GO (rGO) ensured expedient transfer of water through the composite matrix for fast filtration.

Likewise, applying knowledge of material interfacial interactions enables the development of fabrication processes that preserve the natural strengths of biopolymers. Biopolymers, particularly proteins are highly sensitive to changes in temperature, pH, ionic character, and mechanical stress.17,89,90,91,92 These factors lead proteins to coil or uncoil in different ways by altering noncovalent like protein and protein-substrate/surrounding media bonds. Globule forming proteins like enzymes achieve functionality through their tertiary structure. And, fiber forming proteins such as silk, collagen, and keratin may lose binding sites that facilitate assembly into hierarchical structures that confer tensile and impact strength.93 For example, chaotropic salts are used to disrupt hydrogen bonds in proteins for stable aqueous dissolution. Chaotropic salts are commonly used for water-based fabrication of biopolymer composites. So, scientists employ various post-processing thermal, strain inducing, solvent and vapor annealing treatments to recover stable, high-ordered structures and intermolecular interactions.89,90,91,92

Such an approach will be key to developing composites with more complex polymeric materials. Synthetic polymers are more resilient than biopolymers in that they are unlikely to degrade or deform in response to fluctuations in environmental conditions. They can be synthesized as copolymers in high volume with defined complexity and surface chemistry. However, their interfacial interactions and conformations in composites can be difficult to probe and predict.94 Currently, diagnostic experiments using dynamic mechanical analysis and viscometry help provide a relative understanding of polymer network ordering and pervasiveness and stress response in an

iterative approach to make a composite preparation protocol.94,95 Composite design driven by fundamental materials understanding would accelerate this process.

RESEARCH GOALS, OBJECTIVES, AND OVERVIEW

1.3 Goals and Objectives

This goal of this dissertation explores bionanocomposite design approaches driven by fundamental understanding of how material structure and process work together to impact composite performance. Figure 4 shows how this work explores composite fabrication techniques and post-fabrication processing affect protein assembly within composites and composite toughness all without imposing a configurational change in the protein backbone. Computational modeling is used to quantify the non-covalent interfacial interactions that drive protein aggregation behavior. These findings are applied to engineer composites with specific mechanical performance properties. In pursuit of that goal, this dissertation has the following core objectives:

Objective 1: Identify material processing steps that induce biopolymer interfacial assembly in response to triggers like temperature, shear force, hydropathy, and pH. Thus, this work begins by identifying characteristic aggregation and adsorption behaviors for biopolymers that have undergone specific processing procedures.

Objective 2: Compare experimental and simulation data to hypothesize underlying mechanisms and the timescale of their effects. Often the mechanisms of interfacial assembly are difficult to monitor in real-time. Simulations are used to recreate these effects in a platform where one can back calculate for temporal phenomena. The simulations will be used to calculate the magnitude of interfacial forces and map individual molecular motion overtime.

Objective 3: Correlate nano-interfacial assembly with mechanical performance and apply these findings to drive material design. Material assembly or structure affects which chemical

groups are available for binding. This then affects the types and prevalence of interfacial interactions that impact adhesion and stress-transfer within a composite, which then determines mechanical performance.

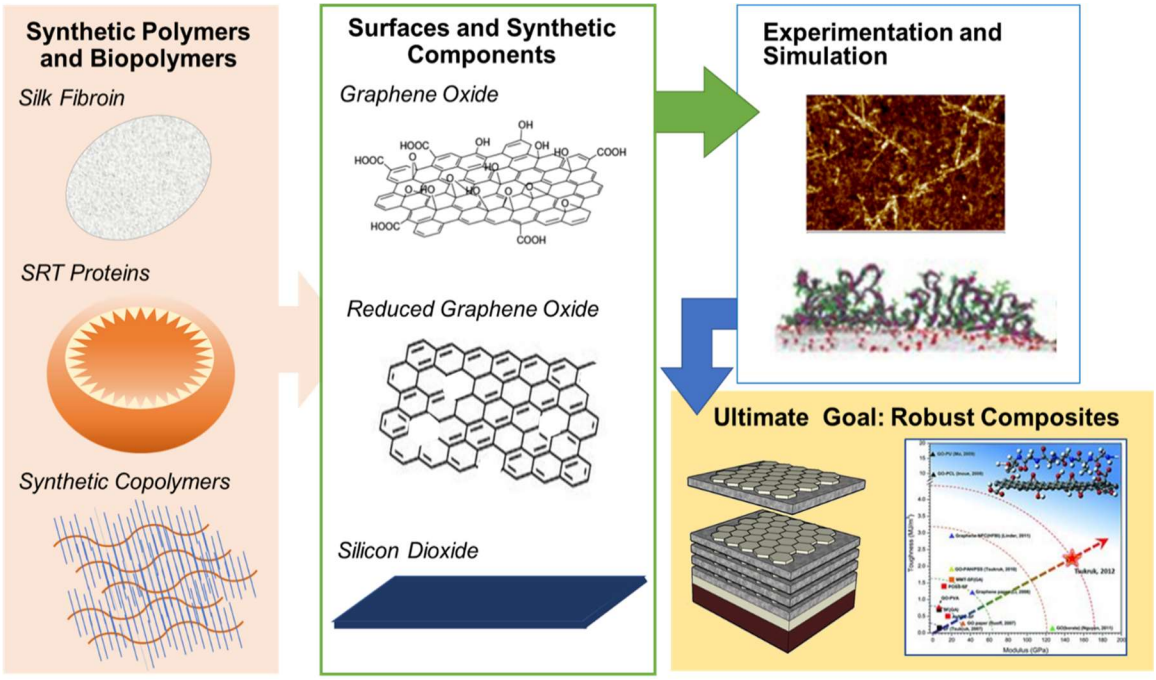

Figure 4: Scheme of proposed work flow.

To fulfill these objectives, this work first defines the effect of processing and substrate chemistry on biopolymer adsorption and assembly using silk. Experimental and theoretical methodologies are used to study *Bombyx mori* silk adsorption at the heterogeneous hydrophobic-hydrophilic surface of GO with different degrees of oxidation. Silk is deposited using various spin casting conditions relevant to the assembly of laminated nanocomposites from graphene-based components and compared with benchmark substrate, atomically flat and homogenous silicon dioxide (SiO2). Secondary structure of silk backbones changes as a function of silk fibroin concentration, substrate chemical composition, and deposition dynamics are assessed and compared with molecular dynamic simulations. The goal of this study is to gain an understanding the effects of processing conditions and surrounding media on silk assembly that can then be applied to the manipulation of other structural, semi-crystalline proteins in organic-inorganic composites.

Then, the applicability of interfacial assembly guided design is demonstrated by applying the findings from the previously mentioned study to fabrication of ultrathin and robust nanocomposite spin cast silk-GO membranes. Spin assisted layer-by-layer (SA-LbL) was used to apply high and low initial shear. Contrasting effects were observed for high versus low initial shear on silk assembly at the interface. High initial shear causes fast solution removal during dropping of solution on constantly spinning substrates that results in largely unfolded biomacromolecules with enhanced surface interactions and suppressed nanofibril formation. The resulting laminated nanocomposites are characterized mechanically, chemically, and morphologically in concurrent tests. After mechanical analysis, failure modes are identified via high resolution crack analysis. Thus, this study yields improved understanding of interphase reinforcement mechanisms at 2D silk-GO composite interfaces.

Using suckerin, this dissertation explores the applicability of lessons from the work on engineering mechanical reinforcement in silk composites via interfacial assembly and whether there is a hierarchy of post-processing treatments. This segment takes a close look at changes in film morphology and aqueous stability in conjunction with concurrently monitored secondary structures in response to shear, vapor annealing, and Hofmeister salt annealing. There is no evidence that the suckerin are covalently cross-linked in native suckerin assembly. The mechanical properties and assembly of suckerin is controlled by modulation of secondary structure and self-assembly into nanostructures. This suggests that suckerin assembles in a manner like silk where the local chemical environment and the mobilization of bulk water drive inter-proteins interactions to create a robust water stable biomaterial. The study on suckerin provides a greater understanding of how its structure impacts film stability without chemical crosslinks.

Lastly, this dissertation addresses the effect of hydrophilicity on interfacial adhesion and polymer adsorption. Synthetic copolymers are used for this study because of their well-defined architecture

and synthetically designed complexity. Graft copolymers with different hydrophilicity are spin and dip cast onto substrates with different hydrophilicity and homogeneity. Copolymer adsorption on or at the edge of GO flakes is closely observed in addition to mechanical performance with respect to different substrate application and during/post-processing treatment. Thus, a deeper understanding of the role copolymer composition has on interface assembly and adhesion is outlined.

1.4 Organization and Composition of Dissertation

Chapter 1 provides background information necessary for comprehension and critique of this dissertation.

Chapter 2 describes the goals and objectives of the research discussed in this dissertation as well as an overview of the organization of the dissertation.

Chapter 3 provides technical descriptions of materials and experimental techniques and characterization most frequently referenced in this dissertation. Subsequent chapters provide greater detail and introduce less frequently used experimental techniques as needed.

Chapter 4 addresses the effects of surface chemistry and processing on silk fibroin self-assembly using high resolution surface spectroscopy. The results show that silk fibroin is highly sensitive to shear induced crystallization and the hydrophobic effect, which can both be tuned to induce silk assembly into crystalline fibrils.

Chapter 5 details how the findings in Chapter 5 were applied to silk-GO nanocomposites. Film mechanical properties were studied using bulging tests and surface spectroscopy to verify protein interfacial assembly. Ultimately, films exhibited increased toughness and higher elongation at break.

Chapter 6 discusses how the aforementioned findings could be applied silk-like protein suckerin-12 using surface spectroscopy to characterize suckeirn-12 assembly and surface mechanical properties concurrently. Here suckerind-12 exhibits toughening due to shear, vapor, and salt treatment.

Chapter 7 details a study on the impact of hydrophilicity in macromolecular assembly wherein synthetic copolymers chemically and physically adsorbed to the surface of graphene derivatives.

Chapter 8 is a discussion of general conclusion and broader impacts of this dissertation.

Chapter 9 contains supplemental figures and information not already provided in the previous chapters.

EXPERIMENTAL TECHNIQUES AND APPROACHES

1.5 Polymers: Biopolymers and Synthetic Copolymers

1.5.1 Preparation of silk fibroin

A silk fibroin aqueous solution was prepared from *Bombyx mori* silkworm cocoons by the conventional procedure, including splitting, degumming, dissolving, and dialysis.96 Briefly, split cocoon shells were boiled in Na2CO3 aqueous solution (0.02 M, 30 min) to extract sericin, rinsed thoroughly with Nanopure water, and dried. The dry fibroin fibers were then dissolved in an aqueous solution of lithium bromide (9.3 M, 4 h, 60 °C) and dialyzed against distilled water (24 h, room temperature) to remove the salt ions. The resulting solution was extracted from the dialysis cassettes (Slide-a-Lyzer, Pierce, molecular weight cutoff 10 000), and remaining particulates were removed through centrifugation. This process enables the production of 3.0 ± 0.3 wt. % silk fibroin solution which was either used as produced or diluted with Nanopure water for experiments outlined here. As previously mentioned, silk fibroin has an amphiphilic block copolymer like structure of hydrophobic, crystalline Gly-Ala-Gly-Ala-Gly-Ser amino acid sequences between hydrophilic, amorphous sections with less defined amino acid sequences (Figure 1). After degumming and inhibition of silk fibroin-silk fibroin hydrogen bonding via LiBr, this amphiphilic structure enables aqueous processing.

1.5.2 Preparation of suckerin-12

Collaborators at the Air Force Research Laboratory in Dayton, Ohio, expressed and lyophilized suckerin-12 proteins for the following experiments. Syuckerin-12 was expressed by E. coli then harvested, purified, and lyophilized. The suckerin-12 produced has a complex amino acid sequence dominated by Gly, Tyr, Leu, His, and Ala with Gly comprising the highest percent composition and Ala the least. An N-terminal His6 tag was added to each peptide to aid purification by affinity

chromatography. Lyophilized suckerin-12 was dissolved in water and 5% glacial acetic acid added to set the solution pH to 5. suckerin-12 films were made by spin casting 3 wt. % suckerin-12 aqueous solution at 3000 rpm for 30 seconds. Select suckerin-12 films were crosslinked using a solution of 40units/mL horseradish peroxidase and 0.02 v/v % of hydrogen peroxide (H2O2). The horseradish peroxidase (HRP) –H2O2 solution was dropped onto the samples and allowed to sit in a humid petri dish overnight. The samples were then rinsed with 18 MΩ cm Millipore water and allowed to dry in air.

1.5.3 Preparation of synthetic copolymers P(G66-O34) and P(G15-O66-L19)

Copolymers type 1 P(G66-O34) and type 2 P(G15-O66-L19) were provided by researchers in Professor Igor Luzinov's research group at Clemson University according to the recently published protocol (Figure 5

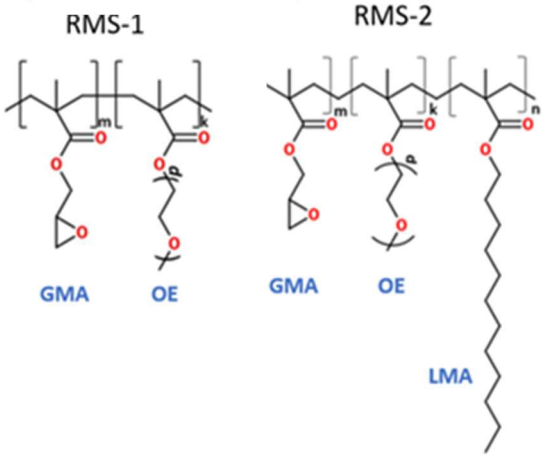

Figure 5).97 The copolymers were synthesized by solution free-radical polymerization. Monomethyl ether hydroquinone remover beads were added to glycidal methacrylate (97%) (GMA) and lauryl methacrylate (LMA) prior to the synthesis. MEHQ and tert-butylcatechol inhibitor remover beads were added to oligo(ethylene glycol) methyl ether methacrylate (OEGMA) dissolved in methyl ethyl ketone (MEK) prior to synthesis. Solutions were then filtered through 0.2 µm syringe filters. The LMA:OEGMA:GMA molar ratios for were 0:80:20 and 20:60:20 for copolymer type 1 and type 2, respectively. The overall monomer concentration was 0.5 mol L-1 and the AIBN concentration was 0.01 mol L-1. The solution was purged under nitrogen gas for 45 min then immersed in a 50 oC water bath. The polymerization reaction was terminated after 1.5 h

by opening flask to the ambient atmosphere and removal from the water bath. The resulting copolymers were precipitated by diethyl ether, centrifuged and re-dissolved in MEK. This procedure was repeated three times in order to remove unreacted monomers and initiator.

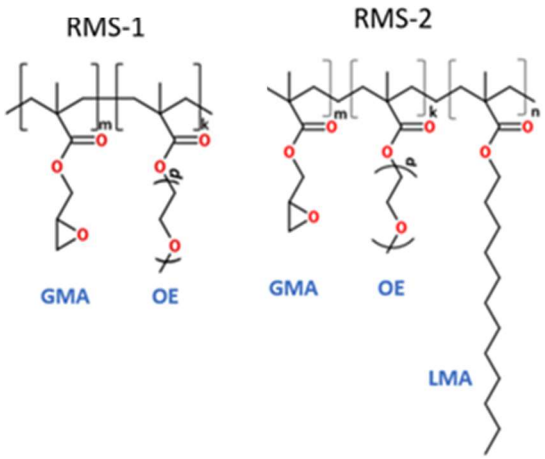

Figure 5: Chemical structure of synthetic copolymers P(G66-O34) and P(G15-O66-L19)

1.6 Substrates

A core driver for protein assembly in this work is interfacial interactions. Here, interfacial forces are tuned via (1) environmental changes like temperature, pH, ionic character, and humidity; (2) protein covalent and non-covalent modification; and (3) surface chemistry and topology of composite co-constituents and underlying substrate. The first two were mentioned above. This section explains how the third approach taken to probe the third factor in protein assemble will be probed. Specifically, the effects of surface chemistry and topology are investigated using silicon dioxide and GO derivatives. The first functions as a hydrophilic, low roughness surface.98 SiO2 is compatible with the amphiphilic and hydrophilic adsorbents discussed here. Literature shows that amphiphilic proteins tend to form β-sheets on hydrophilic surfaces, so SiO2 may serve as an aid to preferential protein assembly.22 This smooth, hydrophilic surface serves as a control to which protein assembly on graphene-derived flakes will be compared.

GO serves as the test surface given its prevalence in bionanocomposite systems and available hydroxyl and carboxylic acid groups for facile modification with anions, cations, and macromolecules.33,75 Graphene consists of a planar lattice of C-C bonds which form conjugated structure and exhibit π–π stacking when stacked. These features imbue GO with high thermal and electrical conductivity as well as mechanical strength. However, graphene is typically obtained via chemical vapor deposition of graphitic flakes that are oxidized to induce delamination into monolayered flakes of GO.2,9 Though less conductive than graphene, GO has an amphiphilic composition that enables aqueous processing and homogenous mixing with other amphiphiles like silk fibroin. Hydrophilic moieties carboxylic, epoxy, and hydroxyl groups offer sites for surface modification via grafting of nanoparticles, peptides, and polymers.99,100,101 GO has strong performance properties and chameleon-like adaptability that make it well-suited for protein bionanocomposite design and investigation of substrate surface chemistry and topology effects on proteins assembly.

1.6.1 Preparation of silicon dioxide surface

Silicon dioxide serves as a hydrophilic surface for protein and graphene-derived flake adhesion. The silicon dioxide surface is obtained by copious rinsing silicon wafers then cleaning the surface via piranha solution (70% sulfuric acid, 30% H2O2) for 1 hr followed by additional rinsing to remove residual oxidizer. Piranha treatment helps remove residual matter on the wafer prior to polymer or graphene-derivative deposition and hydroxylates the surface to make it hydrophilic with a contact angle of 5o.102

1.6.2 Preparation of graphene derivatives

Graphene oxide. GO was prepared by the modified Hummer's method using 325 mesh acid graphitic powder.103 The powder was exfoliated and oxidized by immersion in concentrated sulfuric acid while stirring. Then the suspension was cooled in an ice bath before dropwise addition

of KMnO4 with constant stirring. After adding H2O2 to terminate the reaction, the suspension was rinsed several times in water. Unexfoliated graphite was removed by centrifugation. X-ray photoelectron spectroscopy (XPS) of a drop cast sample of the prepared flakes indicated C/O of 2.2, which suggested 45 wt.% oxygen coverage of the GO flake primarily in the form of alcohols and epoxide groups. Addition of epoxide and carboxylic groups on the flake surface interfered with π-stacking via interflake electrostatic repulsion which enabled facile solvation in aqueous media.22 The flakes were amphiphilic, anionic particles as shown via contact angle and zeta potential measurements of 51° and −19.7 ± 0.9 mV, respectively. 77,104

Reduced GO. GO was chemically reduced by hydrazine (N2H4) vapor and solution reduction for AFM and FTIR, respectively. For N2H4 vapor reduction, a solution of 35 wt.% N2H4 in water and NH4OH at 3:5 ratio was heated in a glass vial on a hot plate. GO flakes cast on a substrate were placed at the vial opening for 15 min to induce full GO reduction. This method enabled rapid rGO flake preparation for AFM characterization of proteins on rGO. However, several protein–rGO bilayers were necessary for obtaining ATR-FTIR spectra. Using the vapor reduction method, protein would be repeatedly exposed to heat which could melt the protein. rGO used on ATR-FTIR samples was prepared by adding 35 wt.% N2H4 in water to 100 mg GO aqueous suspension at 100 °C while stirring. After 3 h, rGO precipitated to form a black cake that was rinsed, dried in a vacuum oven, and re-dispersed in water via sonication then centrifuged to remove insoluble aggregates.105

This method produced fragmented flakes that enabled facile preparation of ATR-FTIR samples using protein–rGO bilayers. XPS of samples for both hydrazine vapor and solution reduction of GO indicate removal of most carboxyl groups and carbon–oxygen double and single bonds.22 GO prior to oxidation had two major peaks at 285.4 and 287.5 eV and a shoulder at 288.7 eV which were characteristic of C-C and C=C bonds, C-O, and C=O bonds, respectively. From atomic weight percent of C, O, and N, it was apparent that GO began with C/O ratio of 2.2:1. Assuming there was one oxygen atom for each oxygenated group and that each benzene ring in the graphene sheets had

effectively two carbon atoms, XPS indicated each benzene ring had an oxygen atom for 45% oxygen surface coverage per GO flake surface.9 After reduction by hydrazine vapor for 15 min, the C-O diminished by 80% but a slight shoulder remained due to the presence of residual C-O moieties. C/O ratio for the rGO decreased to nearly zero. Similarly, the disappearance of peaks at 287.5 and 288.7 eV suggested complete reduction of rGO via hydrazine solution reduction.

GO modified with P(G66-O34) and P(G15-O66-L19) copolymers. Polymer grafted GO flake solutions were provided by member of Igor Luzinov's research group at Clemson University.97 They were prepared from GO aqueous suspension produced using the modified Hummers method and 300-mesh graphite powder (Alfa Aesar).103 GO water suspension (~ 3 mg ml-1) was mixed with water solution of P(G34-O66)/P(G15-O66-L19) (~ 5 mg ml-1) in mass ratio 1:6, so to have polymer in abundance (Figure 6). The mixture was shaken for 15 minutes and then it was kept at room temperature on an orbital shaker. After at least 4 hours GO sheets were evacuated from the solution by centrifugation at 10000 rpm for 5 minutes and rinsed 3-4 times with DI water to remove unattached polymer chains. Then the suspension was centrifuged at 1000 and 500 rpm for 15 min at least two times in to get rid of all flocculated sheets.

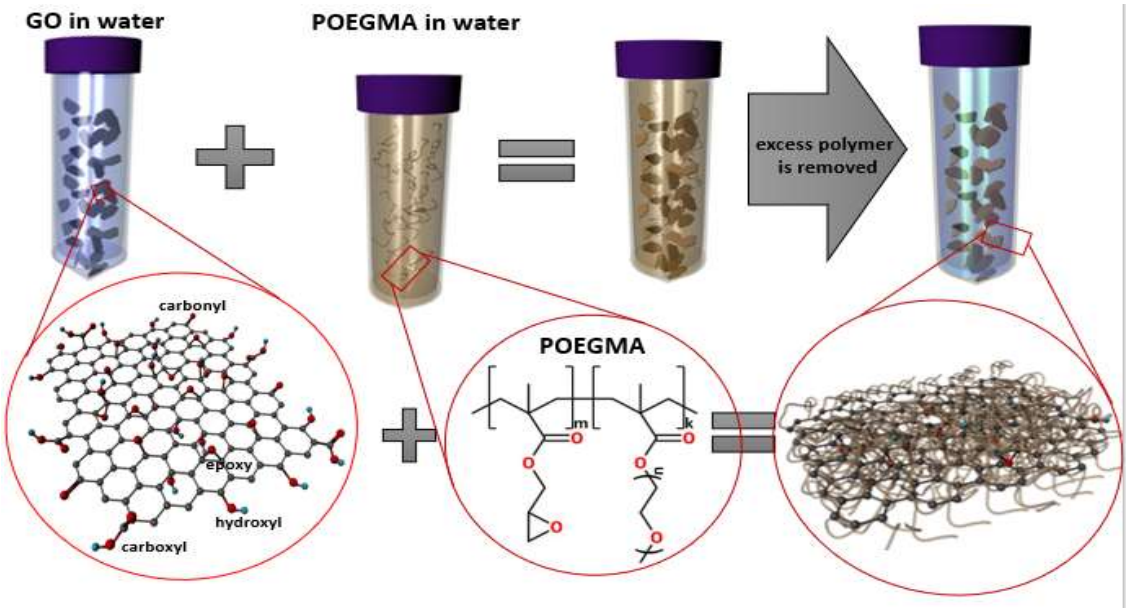

Figure 6: Scheme for modifying GO with the copolymers.

1.7 Experimental techniques

1.7.1 Sample fabrication

Layer-by-layer (LbL) assembly is a film making approach that uses electrostatic forces, hydrogen bonding, hydropathy, etc. to induce layering of different materials into multilayered systems.106 LbL is applied in polymer micelle fabrication and laminated composite assembly and enables multilayer composite forming on materials with unconventional shapes. Here LbL is applied to make laminated composites in which interfacial interactions are inherently amplified and become the core basis for observed mechanical properties whereas weakness in bulk composites could just as likely derive from inhomogeneity in the mixture.

Predominantly single and bilayer films are constructed piranha oxidized silicon wafers via dip-coating, Langmuir Blodgett (LB), and spin assisted LbL (SA-LbL). LB was pioneered by Irving Langmuir and his protegee Katherine Blodgett to enable fabrication of homogenous,

monolayers.107 In this method, a substrate is immersed in a water trough then an amphiphilic monolayer component is deposited on the water surface. Then the trough surface area is decreased to increase water surface pressure. This causes the amphiphilic material deposited on the surface to condense into a solid-like layer and the substrate is drawn out of the trough, allowing transfer of the dense, monolayer from the water surface to the substrate. The same trough and dipper used for LB was adapted for dip-coating. Dip-coating enabled faster fabrication of single flake and dense films of graphene derivatives.97 SA-LbL offered an even faster method of monolayer fabrication though often with few, rather than single layer graphene derivative flakes. SA-LbL assembly also provided accelerated solvent removal and shear force known to induce protein crystallization. In this approach, each layer was formed by depositing the solvated layer component then spinning the substrate dry in a spin-coater.22,110

1.7.2 Sample Characterization

Scanning probe microscopy. Biopolymer morphology, modulus, and adhesion properties were captured using a Bruker Icon AFM in standard tapping and QNM mode. silk fibroin fibril assembly was probed using ultra-sharp tips with resonance frequency 325 kHz and spring constant 40 N m−1 in soft tapping mode at ambient conditions.108 Most other SPM associated images were acquired using standard tapping mode tips whose average spring constants and resonant frequencies were 0.2 - 40 N m-1 and 15 - 350 Hz, respectively.

Bulging tests. The bulging test requires a stable free standing thin film of material to be stretched until breaking using a lab-made interferometer that uses automated pumps to pull air thus providing mechanical properties on the macro scale.109 During bulging tests, a film is suspended over an aperture of 300 μm in diameter, then puffs of air are applied to it at different pressures and frequencies with film deflection captured by an interferometer. A stress versus strain plot is constructed from the collected applied pressure and deformation data and analyzed.

Buckling tests. Buckling is another method that provides an evaluation for compressive elastic modulus from buckling instabilities developed during compression of the films transferred onto an elastomeric substrate. This method allows mechanical characterization of ultrathin films and high throughput analysis of many variables.110

Ellipsometry. Sample thickness was measured using a Woollam M2000U variable-angle spectroscopic ellipsometer with a wavelength range of 245–1000 nm. Generally, a Cauchy model was applied to model the 620-1000 nm region of the optical spectrum.111

X-ray diffraction (XRD). XRD experiments were performed employing Cu Kα radiation (at 40 kV and 20 mA). The Scherrer equation $D = K\lambda/(B \cos \theta)$ was employed to estimate the stacking number of the bilayer structure and the size of the β-sheet crystals of silk, where D is the stacking number, $K = 0.9$ is the shape factor, λ is the wavelength of the X-ray (0.154 nm), B is the full width at half-maximum (fwhm) of the diffraction peak, and θ is the Bragg angle.

Transmission electron spectroscopy. Microstructures of select nanocomposites were placed on 200 mesh copper grids for transmission electron microscopy conducted with a Hitachi 7700 at 120 kV.

Fourier transform infrared spectroscopy. High-resolution FTIR has been conducted by using a Bruker Vertex 70 infrared spectrometer. Samples were deposited on a silicon attenuated total reflectance crystal to probe ultrathin film samples.

Optical microscopy. Optical images were obtained using a Leica DM 4000M microscope to evaluate macroscopic morphology changes and phase separation.

X-ray photoelectron spectroscopy. XPS was conducted by using Thermal Scientific K-Alpha instrument. XPS was used to evaluate surface and film composition.

1.7.3 Molecular dynamics simulations

Atomistic molecular dynamics simulations are used to explore the interactions and secondary structure formation of proteins and synthetic copolymers in proximity to various surfaces including graphene, GO and silicon dioxide. Dr. Ho Shin Kim and Professor Yaroslava Yingling at North Carolina State University contributed the simulation results. The GO surface introduced here had 20% of oxygen content which consists of epoxy and hydroxyl molecules in the ratio of 3/2.112 The (100) face of SiO2 displays silanols with a surface density of 2.5 silanols/nm2 and a ratio of 17:1 between single to germinal silanols.113,114 Representative segments of the polymer structures were used to complement the experimental research. Initial biopolymer 3D structures will be obtained using I-TASSER server.115

SILK FIBROIN MOLECULAR ASSEMBLY

1.8 Overview

To address the first objective, silk fibroin was used to show the effects of processing and surface chemistry on protein assembly.22 Silk fibroin adsorption at the heterogeneous hydrophobic-hydrophilic surface of GO with different degrees of oxidation was explored experimentally and theoretically. Samples are prepared via spin assisted deposition using various conditions to form laminated silk fibroin and graphene based laminated composites. SiO2 serves as a benchmark substrate. Changes in the secondary structure of silk fibroin was characterized as a function of silk fibroin concentration, substrate chemical composition, and deposition dynamics. Experimental and simulated results were combined to evaluate the effects of processing and surrounding chemistry on silk fibroin assembly and to quantify interfacial interactions driving observed phenomena. Shear induced crystallization and surface amphiphilicity were found to promote silk fibroin adsorption to the surface and subsequent assembly into fibrillar structures.

This chapter contains portions of a manuscript by A. Grant, H. Kim, T. Dupnock, K. Hu, Y. Yingling, and V. Tsukruk; entitled Silk fibroin-Substrate Interactions at Heterogeneous Nanocomposite Interfaces and published in Advanced Functional Materials in 2016.

1.9 Experimental

Preparation of reconstituted silk fibroin. Silk fibroin was extracted from *Bombyx mori* silkworm cocoons as described in Chapter 3 then diluted to 0.2, 0.02, 0.002 wt. % and refrigerated at 5 oC.

Preparation of GO. GO flakes were prepared as discussed in Chapter 3 then diluted to 0.04 wt. % and spin cast for AFM and FTIR characterization.

Preparation of rGO. GO flakes were reduced via hydrazine vapor and solution treatments for FTIR and AFM samples, respectively as discussed in Chapter 3.

High resolution atomic force microscopy. The sample topography was via AFM as discussed in Chapter 3 using soft tapping mode at ambient conditions. Samples were characterized at several scan sizes though only 2, 1, and 0.500 μm were depicted here with pixel sizes of 2, 1, and 0.5 nm, respectively. Given that each tip radius was ≈1 nm, higher resolution than those shown were not possible without tip convolution due to pixel size being over an order of magnitude less than the tip size. Several points were characterized on each sample. Cross-sections were measured for 30 particles and/or fibril subunits for each captured image using 0.5 nm pixels. Height measurements taken were then used to calculate the particle/subunit volume. In these calculations, the globule-like particles were assumed spherical and the volume equation for a sphere was utilized, whereas fibril height and subunit length were utilized to compute their subunit volume as would be done for a cylindrical particle.

ATR-FTIR. Silk fibroin and/or GO were cast onto a silicon ATR crystal while both immobile (drop cast) and mobile (spin cast). Analysis was conducted as discussed in Chapter 3.

MD simulation. All simulated results were obtained as discussed in Chapter 3 from collaborators North Carolina State University.

1.10 Results and discussion

1.10.1 Comparison of Silk Fibroin at Different Deposition Conditions

Initial experiments focused on the effects of silk fibroin concentration, conventional versus dynamic casting, and spin speed on secondary structure of absorbed silk materials under common spin assisted LbL (SA-LbL) assembly conditions. A monolayer of GO flakes on silicon wafer served as the substrate and samples were prepared using silk fibroin aqueous suspension at 0.2, 0.02, and 0.002 wt. % deposited on initially immobile substrates for conventional SA-LbL and on spinning substrates for dynamic SA-LbL (dSA-LbL) then spun dry at different spin speeds.

Figure 1 shows surface morphology of silk fibroin deposited as an aqueous suspension onto a GO flake on a silicon wafer. GO flake lateral dimensions varied from 3-6 μm with 0.9 nm thickness, which is indicative of monolayers.30 On the oxidized GO substrate, silk fibroin exhibits distinct morphological transitions when deposited at different concentrations. When spun from a concentrated suspension, silk fibroin retains a spherical globular structure. For instance, 0.2 wt. % silk fibroin cast on GO exhibits densely packed globules with height of 2.0 ± 0.5 nm (Figure 7). Particles are assumed spherical in dimension, so the classic sphere volume equation was used to calculate their volume, wherein height measured via AFM was used as diameter.116 The particle volume determined this way varied depending on silk concentration as this resulted in different secondary structures and packing densities. Individual silk fibril subunits, the beads on a string like components of the fibrils are 1.4 ± 0.5 nm, while the globule-like structures exhibited are mostly 40-200 nm3. This suggests these are individual globular silk backbones.95,117,118 Variation in volume is greater for the globule-like structures than fibrils due to aggregation as Well as difficulty in accurately measuring the individual particle height amongst the bed of other globule like structures.

When diluted by 10 times to 0.02 wt. % silk fibroin, globules of similar sizes were observed (Figure 7). Upon further dilution to 0.002 wt. % silk fibroin, morphology changed dramatically with individual bundles formed which are comparable in size to individual silk backbones with average height of 0.86 ± 0.22 nm (Figure 7). The morphologies at the various concentrations reflected

findings from previous studies conducted in solution on a mica.17,89 These studies showed a dense globular morphology above 1 wt. % with a reduction in globule size at 0.1 wt. % then fibril formation below 0.01 wt. %. As shown here, the fibrils observed in this case had diameters several times smaller than the globular aggregates observed in high concentration regime.

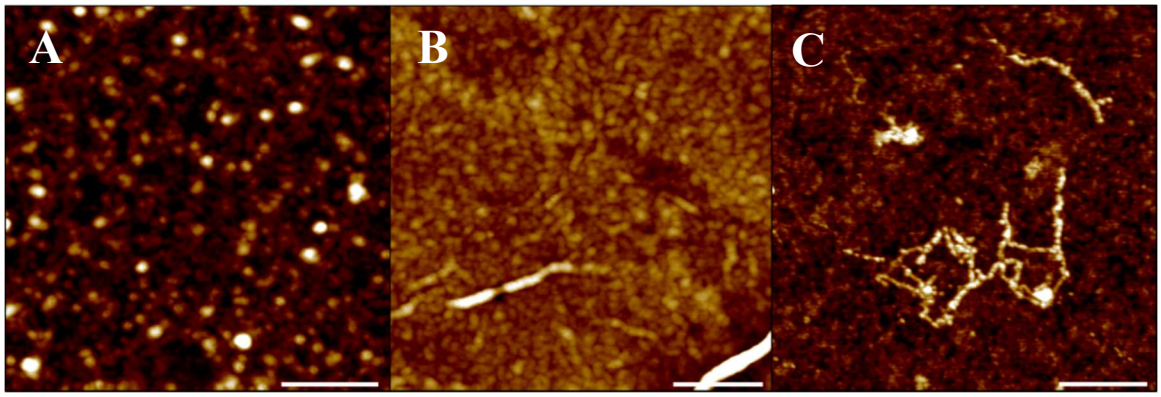

Figure 7: AFM topographical images of silk fibroin absorbed from 0.2 (A), 0.02 (B), and 0.002 wt. % (C). silk fibroin deposited on GO flakes on a silicon wafer via conventional SA-LbL at 5000 rpm. Scale: 200 nm. Z range: 4 nm (A and C) and 8 nm (B).

Figure 8 depicts AFM topographical images of silk fibroin assembly when 0.002 wt. % silk fibroin was deposited via conventional SA-LbL onto GO flakes and silicon dioxide (SiO2) surfaces at several spin speeds. As previously shown on mica, another homogenously hydrophilic, anionic substrate, the combination of low concentration and applied shear after initial adsorption are enough for fibril formation on SiO2 surfaces. Although, applied shear seems necessary for fibril formation there is no apparent effect on the dispersity of their assemblage. On GO flakes, conventional SA-LbL leads to less accumulation of silk fibroin on GO flakes with little fibril formation. Linear assemblies are observed at the highest rotational speed of 8000 rpm with some observable fibrils formed at 3000 and 5000 rpm, though increased roughness on the flakes renders them less easily distinguished (Figure 8). Conventional SA-LbL assembly yields globules of random coils at different locations with inter-globule alignment suggesting initiation of assembly.

In contrast, dynamic spin casting yielded linear silk fibroin assemblies on both SiO2 and GO flakes (Figure 9). Linear fibrils of variable length are formed at each spin speed 78-370 nm in length. Dimensional analysis of these images shows fibrils of uniform diameter with globule like structures along the fibril and at fibril intersections for 0.002 wt. % silk fibroin on GO flakes. Extended chains formed when 0.002 wt. % silk fibroin was spun cast dynamically on GO flakes (Figure 9).

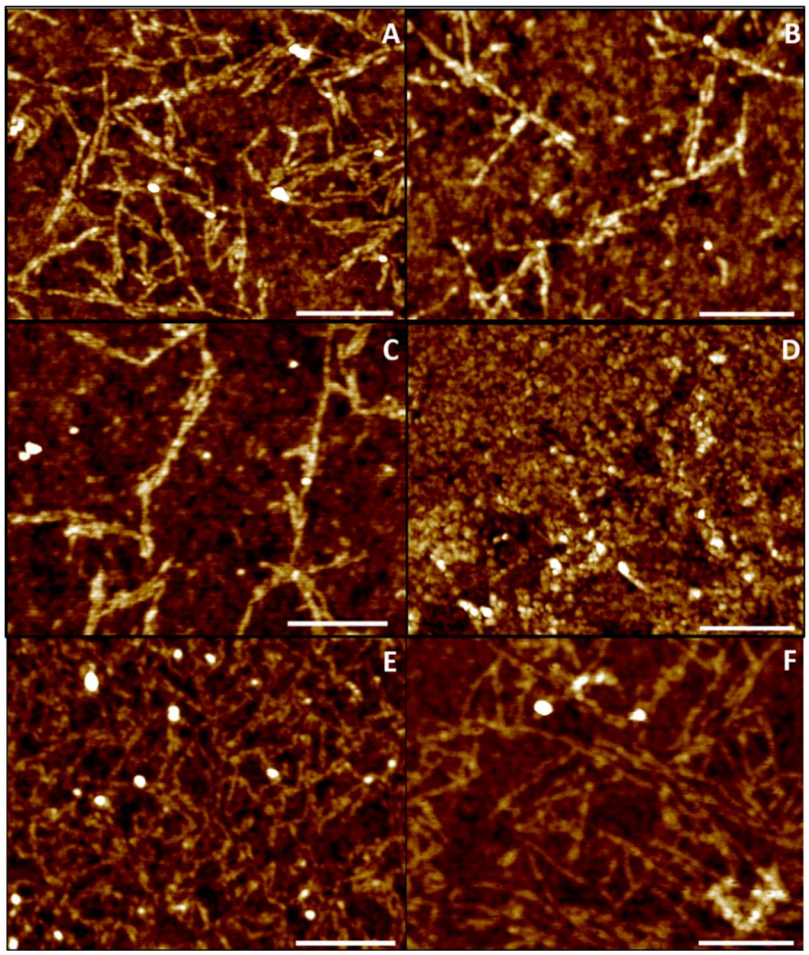

Figure 8: AFM topographical images of 0.002 wt. % silk fibroin morphology after conventional SA-LbL on SiO2 surface (A, B, C) and GO flakes (D, E, F) on a silicon wafer at 3000 (A, D), 5000 (B,E), and 8000 (C, F). Scale: 200 nm. Z range: 2nm (A, B, C, D, E, F) and 6 nm (D).

Average fibril height was 0.85 ± 0.13 nm, which is close to the expected backbone diameter and very similar to values previously reported for individual fibrils and dimensions of simulated the GAGAGS sequence in β-sheet structure.116,117 The broad distribution is attributed to the globule

like structures in Figure 3 that form at fibril junctions. Larger structures at fibril joints are thicker than the fibrils and have a volume comparable to that observed for random coils and helical conformations.117 For dilute silk fibroin on GO, high initial shearing seems to be critical for fibril formation where greater dispersion lessens intermolecular interactions between silk molecules that must be overcome to induce absorption with unfolded morphologies.

As shown in a previous publication, the rapid solution removal inherent in dynamic deposition increases interfacial adhesion and shear induced crystallization. However, spin speed variation appears to have little bearing on silk fibroin morphology as indicated by conformational uniformity at a given concentration across all spin speeds. Previous studies have shown a positive linear relationship between fibril formation and shear rate.76,119

Unlike those studies, which were conducted in solution, the present study entailed rapid solvent removal during the assembly process. The results presented suggest that as solvent quickly shears off the substrate, long-chain flexible protein macromolecules are stretched and locked in place by quenching during fast solvent removal. These dueling factors inhibit fibril formation with increased shear rate.

ATR-FTIR spectra of silk fibroin-GO films prepared under relevant conditions exhibit characteristic peaks at 1626, 1634, 1645, 1653, 1661, 1668, 1684, and 1697 cm-1.120 silk fibroin secondary structures consist of a mix of amorphous random coils and ordered β-sheets, helices, and β-turns.4,19,20,21,92 According to these studies, silk fibroin secondary structure can be categorized more broadly as silk I for random coils and helices, silk II for β-sheets, and silk III for helices. Contributions of various secondary structural components were quantified by deconvolution of the amide I peak (1586 – 1720 cm-1), which is broadly attributed to C=O stretching. The amide I region was baseline corrected and then deconvoluted via Fourier self-deconvolution and second derivative analysis of the amide I peak.121

When spun cast, silk fibroin infrared absorbance increases at representative β-sheet peaks (1626, 1634, and 1697 cm-1), indicating increased crystallinity in sheared silk fibroin. An accompanying decrease in absorbance at 1645 and 1653 cm-1, peaks attributed to random coils, suggest a shift of the secondary structure composition from random coils to β-sheets.117,26,30,93,103 Meanwhile, peaks at 1668 and 1684 cm-1 for turns and 1661 cm-1 for helices remain relatively unperturbed. silk fibroin sheared on GO has a slightly more β-sheet dominant secondary structure than drop cast silk fibroin.

Crystallization of drop cast silk fibroin is mostly owed to extended drying time during which silk fibroin has to reorder into its lowest energy conformation, β-sheets.116,118 Introduction of GO flakes for silk fibroin-GO bilayers yields similar ATR-FTIR signatures where β-sheet peaks at 1626 and 1634 cm-1 have increased while decreased absorbance at 1645 and 1653 cm-1 indicates loss of random coil secondary structures. Overall, GO appears to preserve the crystalline secondary structure while enabling switching from random coil to β-sheet.

The differences between conventional and dSA-LbL of silk fibroin-GO pairs were explored in a previous publication. Without the initial stage of slow static adsorption, there is increased stretching of proto-fibril structures as β-sheets form from random coils while the proportion of helices and turns appear unaffected. The analysis of protofilament structures observed in this experiment with increased β-sheet content allows for an understanding of secondary structure on this surface. Dimensional analysis of linear fibril assemblies suggests these structures are protofibrils of aligned silk fibroin molecules. This is further corroborated by previously reported silk morphologies on mica where the appearance of linear assemblies is accompanied by increased crystallinity.116,117,95,103

1.10.2 Effect of graphene oxidation on silk fibroin assembly behaviour up

Then, silk fibroin secondary structure changes were studied after adsorption on an increasingly hydrophobic surface with graphitic patches. After depositing GO flakes on SiO2, the flakes were fully reduced by hydrazine vapor. GO flakes were reduced to C/O of 15.1 and oxygen coverage of 3.3 wt. % after hydrazine vapor reduction to rGO state. Then, 0.002 wt. % silk fibroin was deposited via conventional and dynamic assembly at various spin speeds to probe the effects of static adsorption time and increased shear on silk fibroin folding and secondary structure. Results from initial experiments on the silk fibroin-GO interface were compared to silk fibroin-rGO. As observed, the extended exposure to hydrazine and heat added to vaporize the reducing agent during GO hydrazine vapor reduction could cause a conformational shift in silk fibroin with or without incorporation of rGO. Alternatively, samples for ATR-FTIR, were prepared by complete reduction of GO in hydrazine solution then suspension of the resulting rGO in water for assembly of silk fibroin-rGO SA-LbL films. Poor rGO solubility in water was overcome with extensive sonication and used quickly before sedimentation. Despite the different reduction methods applied for high resolution AFM and ATR-FTIR, comparable reduction was achieved for both hydrazine vapor and solution rGO.

Figures 10 and 11 show topographical AFM images of silk fibroin on fully reduced rGO. Samples universally exhibited a dense layer of silk globules rather than individual or aggregated fibrils for all deposition conditions. The globules are 3.85 ± 1.39 nm in height, an order of magnitude larger than fibrils observed on GO and comparable in size to the globules formed by concentrated silk on GO and micelles reported elsewhere.89 Morphologies observed here suggest that silk molecules previously observed as individual fibrils at 0.002 wt. % silk fibroin on GO have collapsed into single macromolecular bundles much like the morphology of non-sheared silk fibroin in solution.17,90

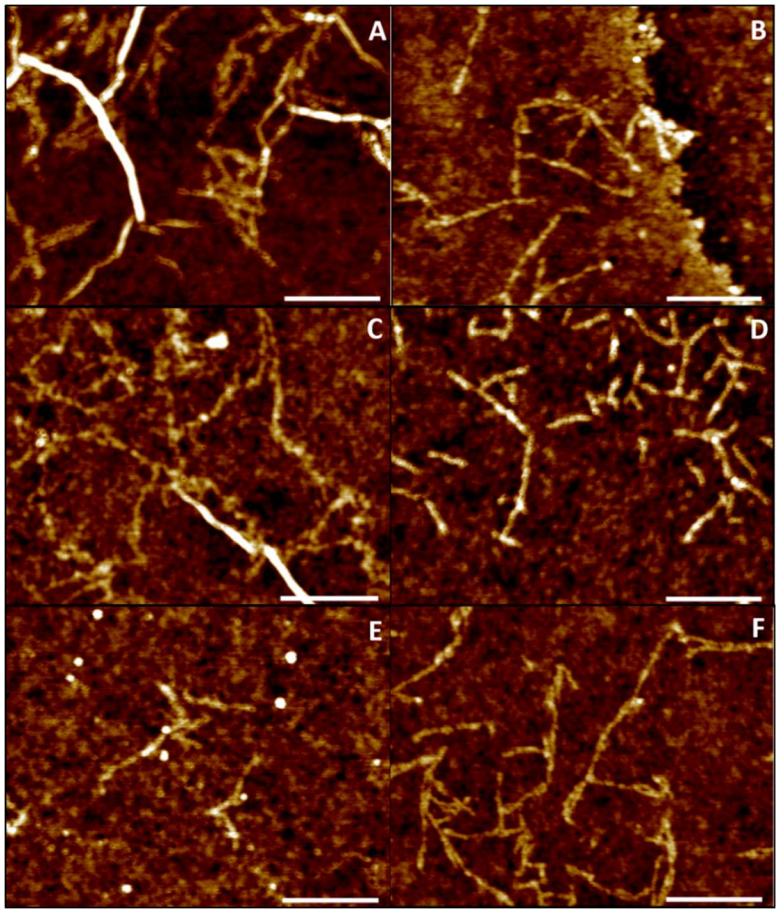

Figure 9: AFM topographical images of 0.002 wt.% silk fibroin morphology after dynamic casting on GO flakes on silicon wafer at 1000 (A), 2000 (B), 3000 (C), 4000 (D), 5000 (E), and 8000 (F) rpm. Scale: 200 nm. Z range: 2 nm.

Upon increasing the shear rate during casting, the globules exhibit the onset of assembly into bulbous, aligned structures. Figure 10 of silk fibroin cast on rGO flakes via conventional SA-LbL at 8000 rpm seems to show the onset of filament assembly among silk fibroin molecules. Globule diameter ranges 3.4-4.7 nm, though this measure is hard to discern due to dense foreground of globules around each individual structure (Figure 10). Increased silk fibroin adsorption on rGO even at low concentrations can be credited to hydrophobic interactions between the hydrophobic rGO substrate and mostly hydrophobic silk fibroin. Although silk fibroin resists extension on the hydrophobic substrate, shear seems to effect intermolecular assembly. Protein macromolecules tend to adsorb more on hydrophobic surfaces due to inability of water molecules to adsorb on the surface and interactions between hydrophobic domains on the polypeptide chain.

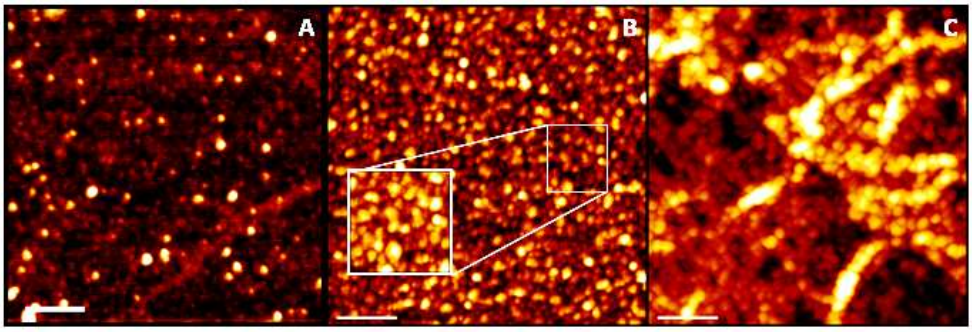

Figure 10: AFM topographical images of 0.002 wt.% silk fibroin morphology after conventional SA-LbL on rGO flakes on a silicon wafer at 3000 (A), 5000 (B), and 8000 (C) rpm. Scale: 500 nm. Z range: 7 nm (A), 11 nm (B), and 28 nm (C).

Peak assignments for ATR-FTIR spectra of the silk fibroin-rGO interface are shown in Table 1 and Figure 12, respectively. The results were analyzed with respect to amide I (C=O stretching, 1650 cm-1), amide II (N-H deformation and C-N stretching, 1530 cm-1), and amide III (C-N stretching and N-H deformation, 1250 cm-1) regions of the IR spectra. Amide III may also be used to determine the kinds of helices present in the material. The second derivative of the IR spectra was used to identify the peaks. Each peak was fitted in accordance with the protocol established in David Kaplan's lab, who were among the first to produce quantitative, high resolution IR spectra of silk fibroin.

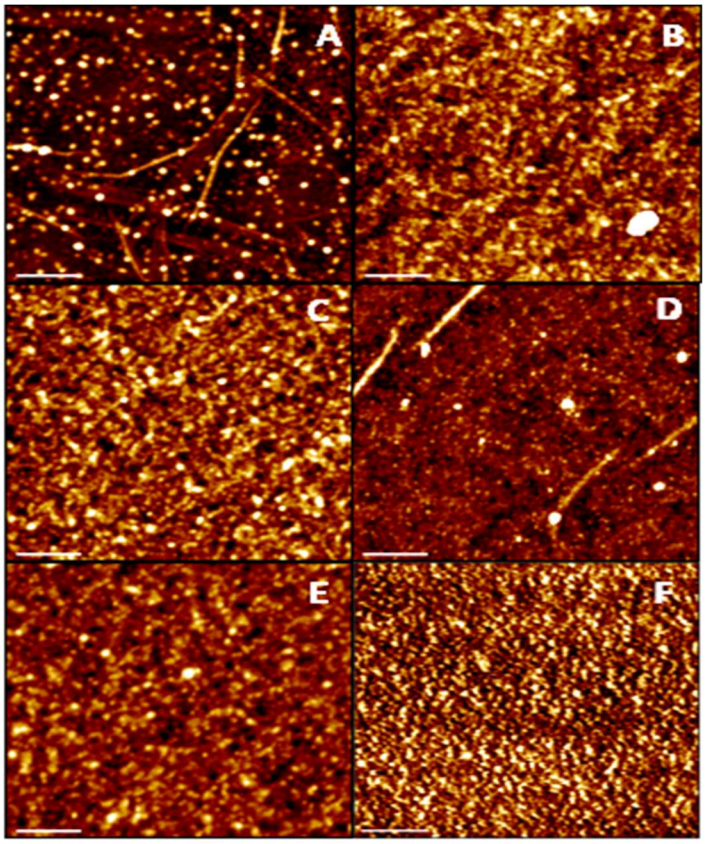

Figure 11: AFM topographical images of 0.002 wt.% silk fibroin morphology after dynamic spin casting on rGO flakes on a silicon wafer at 1000 (A), 2000 (B), 3000 (C), 4000 (D), 5000 (E), and 8000 (F) rpm. Scale: 500 nm. Z range: 8 nm (A and C), 11 nm (B and E), 2 nm (D), and 12 nm (F).

Unfortunately, the ultra-thin samples did not absorb Well in this area of IR so using deconvolution to determine shifts in particular helices was not feasible. Both the amide I and amide II regions are used to discern shifts in β-sheet and random coil content. Analysis of silk fibroin-GO and silk fibroin-rGO in the amide I and amide II regions shows a decline in β-sheet content when rGO is introduced. This is indicated by decreased absorption in an amide II β-sheet peak at 1525 cm-1 and increased absorption in amide I peaks attributed to random coils at 1537 and 1248 cm-1(Figure 12). Thus, the globules on rGO primarily consist of silk I secondary structure (random coils and helices).

Further deconvolution of the amide I region allows for discernment of the relative quantities of various secondary structures in silk fibroin-rGO versus silk fibroin-GO. Comparing spectra of silk

fibroin-GO and silk fibroin-rGO bilayers, the FTIR spectra shows a 48 % loss of β-sheet content in silk fibroin-rGO accompanied by a 52% increase in random coils (1635 and 1655 cm-1) and 50 % increase in β-turns (1668 and1684 cm-1) (Table 1).

Table 1: Wavenumber assignments for secondary structures from FTIR measurements.

Group index	Wavenumber	Assignment
1	1605-1615	side chains/aggregated strands
2	1616-1621	aggregate beta strands/beta sheets (weak)
3	1622-1627	beta-sheets (strong)
4	1628-1637	beta-sheets (strong)
5	1638-1546	random coils/extended chains
6	1647-1655	random coils
7	1656-1662	alpha-helices
8	1663-1670	turns
9	1671-1685	turns
10	1686-1696	turns
11	1697-1703	beta-sheets (weak)

Helices (1660 cm-1) exhibit a marginal decrease for silk fibroin on rGO compared to GO. Hydrophobic silk fibroin-rGO interactions and silk on silk interactions resisted shear-induced crystallization. These results differ greatly from the structure of pure silk fibroin. The observed conformational shift from the typically β-sheet dominant secondary structure of pure silk to mostly amorphous random coils and helices results from rapid adsorption onto rGO surface when the solvent quickly shears off the surface during spin casting.

Our experiments on how silk fibroin morphology and secondary structure may be tuned via substrate chemistry and shear stress can be summarized as follows. Interfacial interactions with hydrophilic GO and SiO2 surfaces induced the formation of β-sheets that aligned into linear assemblies. Enhanced interactions with hydrophobic rGO substrates led to poor initial wetting of the surface by the aqueous silk fibroin solution so that silk I secondary structure was preserved. Thus, simulations were used to study the interplay of noncovalent interactions behind these phenomena using MD simulations. MD simulations were used to identify the major noncovalent interactions, the time scale of their effects, and their impact on silk fibroin morphology.

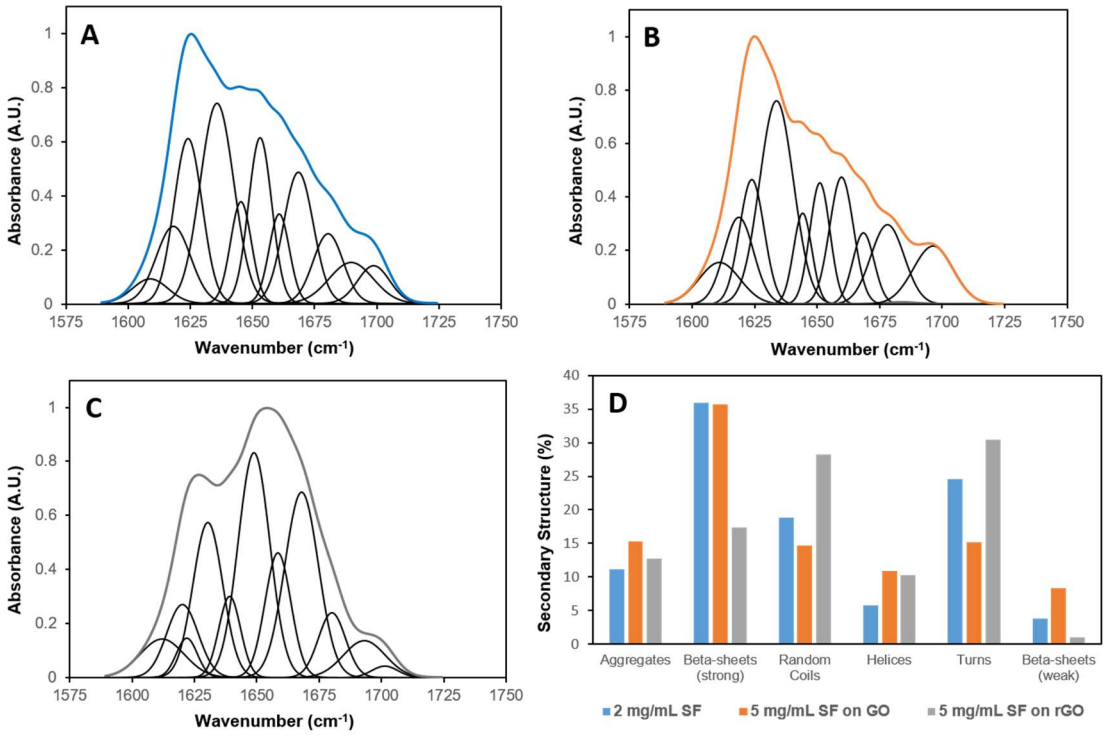

Figure 12: ATR-FTIR spectra of silk fibroin (A), silk fibroin-GO (B), and silk fibroin-rGO (C) in the amide 1 region. The amount of each secondary structure in each sample calculated from peak area of their respective peaks is given in (E).

1.10.3 Simulation Compliance with Experiment

Graphene, as an ideal fully hydrophobic surface with uniform composition and low roughness, and GO with a constant oxygen coverage were simulated because they can be rendered and have comparable surface composition to the fully reduced rGO and GO used in experiment (Figure 13) For MD simulations a typical 258 amino acid *Bombyx mori* protein folded sequence was placed within a few angstroms of graphene, GO, and SiO2 surfaces solvated in water. As shown in

Figure 12 Figure 12, after extensive simulation time, most of the amino acid groups are located near the graphene surface indicating partial unfolding dynamics from ordered helices and β-sheets to random coils and strong adsorption onto the graphene surface. Due to strong interactions between silk and graphene, the height of silk fibroin on the surface also becomes lower (down to 2.3 nm) than that of β-sheet crystal structure dimensions (~ 4.0 nm) or that on other surfaces (~ 3.0

nm) (Figure 13). In contrast, the secondary structure of silk fibroin remains unperturbed on both GO and SiO2 surfaces.

The average height of silk structures on both GO and SiO2 surfaces are like that of β-sheet crystal structures. Identical results are observed in density profiles of silk atoms along x-axis (Figure 13): silk structures on GO and SiO2 are similar to their initial structures, whereas this structure is disrupted on the graphene surface, especially residues adjacent to the backbone tails. The major secondary structure of *Bombyx mori* silk is β-sheet and turn conformations. However, our simulation result shows that β-sheet regions of silk tend to be lost when silk is attached to graphene.

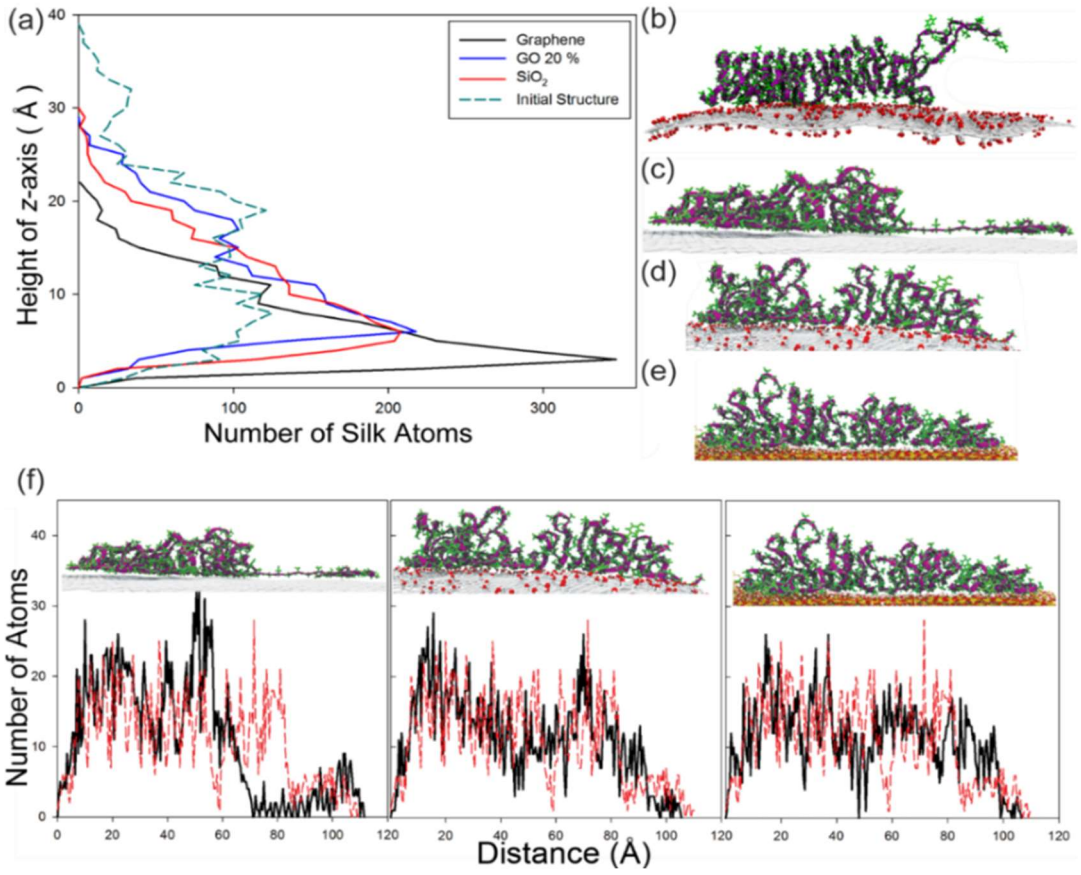

Figure 13: (A) Density profile of silk atoms normal to the graphene (black), GO 20% (blue), SiO2 (red), and the initial silk structure on GO 20% (green dashed line). (B-E) Final snapshot

of each case in (A). (F) Density profile of silk parallel to the surfaces where the initial and current structures are indicated by red and black lines, respectively.

Figure 14Figure 14 shows temporal evolution profile for ordered structures and random coils, where ordered structure includes β-sheets, β-turns, and a small portion of helices. On the graphene surface, the percent of ordered structures gradually decreases as time passes, while the percent of random coils increases.

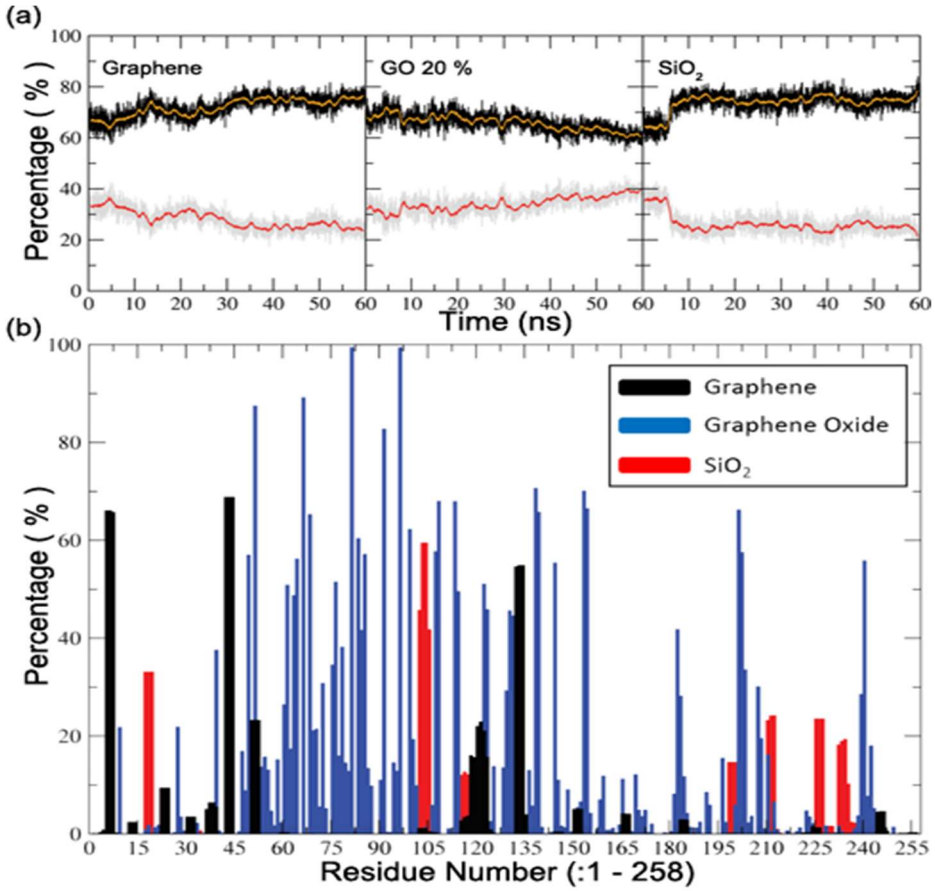

Figure 14: (A) Temporal profile of the percentage of random coils (black) and ordered structures (gray) in the silk structure. Yellow and red lines passing through the black and gray lines indicate the averaged values of the percentage of random coils and ordered structure, respectively. (B) β-sheet content per silk residue.

This trend is in a good agreement with our experimental results where a decline in β-sheet content and increase in random coil structure was exhibited by silk fibroin on rGO. The percentage of ordered structures also decreases in the case of SiO2 surface at around 5 ns, however the overall silk fibroin secondary structure is maintained. In the case of the GO surface, random coil content

decreases and ordered structure increases as a function of time. Interestingly, there is a significant loss of β-sheet structures when silk fibroin is attached on either graphene or SiO2 (Figure 14). In these cases, only a few regions are maintained as β-sheet structures and most of the β-sheet regions turned into other structures. However, these β-sheet structures are maintained Well on the GO surface (Figure 14).

Changes in silk fibroin secondary structure on the various substrates plotted in Figure 15 shows a small increase in β-sheets and over 5 % decrease in random coils on GO. On the other hand, SiO2 and graphene surface prompts an about 10 % increase in random coils content and decrease in β-sheets content. When compared to experimentally observed charges in the secondary structure of silk fibroin (Figure 15), identical trends are observed in both graphene and GO cases, except for turn structures.

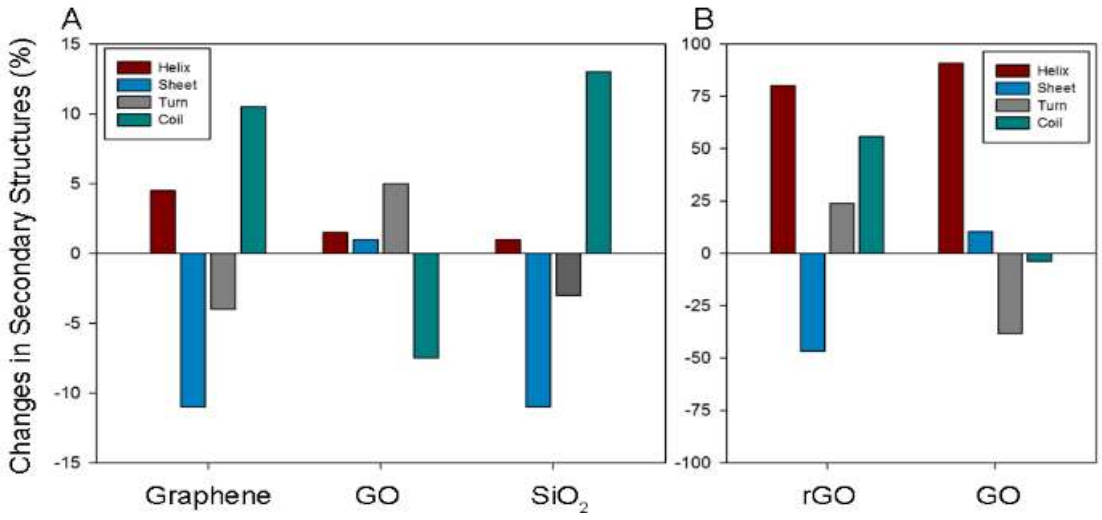

Figure 15: MD simulation (A) and experimentally (C) observed changes in the secondary structure of silk on three different surfaces: graphene (rGO for experimental results), GO with 20 wt. % oxygen coverage, and SiO2.

Therefore, it is expected that GO can stabilize entire secondary structures, however, additional shear stress, which is not considered in our MD simulation, can facilitate intermolecular assembly so that less stable turn structures can interact with a part of helix or β-sheet structures forming more stable β-sheets or helices. Overall, the GO surface not only stabilize the secondary structure of silk

but also promotes recovery from disordered structures to ordered secondary structures. On the other hand, decrease in entire ordered structures and significant loss of β-sheet structures are observed in graphene and SiO2 surface cases as will be discussed further.

1.10.4 Non-bonded Interactions and Protein Synthetic Surface Interfaces

Non-bonded interactions, such as van der Waals and electrostatic contributions were evaluated for GO, SiO2, and graphene, once again, serving as an analogue for surfaces used in experiment.86 As shown in Figure 14, silk fibroin interacts with the graphene surface via van der Waals interactions as there are no functional groups for electrostatic interactions. This assumption agrees well with reality given low functionalization of rGO (see above). However, unlike the graphene surface, the combination of electrostatic and van der Waals contributions play a role in the interactions between silk fibroin-GO and silk fibroin-SiO2. Enhanced van der Waals contributions are observed in silk fibroin-SiO2 interactions whose energy is almost equivalent to silk fibroin-graphene interactions.

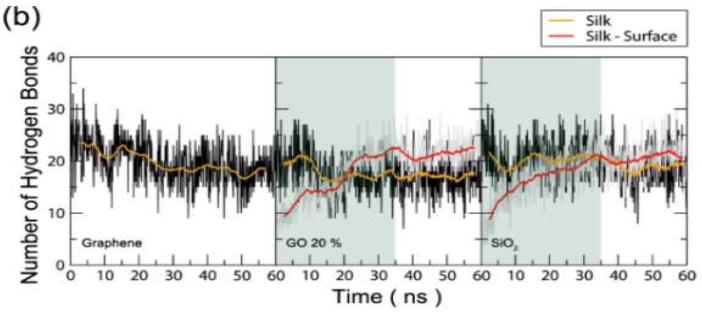

Figure 16: Temporal profiles of the number of internal hydrogen bonds for silk protein on graphene (left), GO (center), and SiO2 (right) surface, where values for silk and silk-surface hydrogen bonding are represented by black and gray lines, respectively. Average values are for silk and silk-surface hydrogen bonding are shown in yellow and red lines, respectively.

Table 2: Rate of forming hydrogen bonds between silk protein and various surfaces

Rate of H-bonds (ns^{-1})	Graphene		GO 20 %		SiO_2	
	0 - 35	35 - 60	0 - 35	35 - 60	0 - 35	35 – 60
Silk – Surface	0.000	0.000	0.412	0.064	0.351	0.062

As shown in the shaded regions in Figure 16 and summarized in Table 2, the fastest rate of hydrogen bonding between silk and surface are observed in the GO surface. In the other two cases, silk – surface hydrogen bonding occurred less and at slower rates on SiO2 due to strong van der Waals interactions, and no hydrogen bonds with graphene are observed between silk and graphene due to negligible electrostatic contributions. Overall, the simulation results suggest that balanced combinations between electrostatic and van der Waals contributions could be important factors in stabilizing protein conformation as well as restoring their ordered structures. Strong van der Waals contributions for interfacial interactions play a significant role in losing and disrupting secondary structures of silk fibroin as shown in both graphene and SiO2 cases. Moreover, as shown with SiO2, strong van der Waals contribution can lead to a loss of secondary structure.

1.10.5 Role of silk fibroin heavy chain in adsorption and assembly

The silk fibroin backbone is 64% hydrophobic heavy chain and 6% hydrophilic light chain (15), so the heavy chain is assumed to dominate silk interfacial interactions. Generally, all twenty amino acids are present in the heavy chain, where 20% are polar and 80% are nonpolar. Glycine (Gly, G) and alanine (Ala, A) account for 75% of the sequence. Figure 1 lists the amino acids present and denotes their polarity, hydropathy, charge, aromaticity, and characteristic nonbonding interactions.122 Gly has no side chain and is considered hydrophobic as is Ala which has a methyl side chain. Together they form GAGAX, GAGX, GAAX motifs where X is serine, a neutral polar amino acid that forms hydrogen bonds. The heavy chain also has considerable quantities of tyrosine (Tyr, Y), valine (Val, V), threonine (Thr, T), phenylalanine (Phe, F), glutamic acid (Glu, E), and aspartic acid (Asp, D) (in order of greatest abundance). Other than when Val, these amino acids either hydrogen bonding (Tyr, Thr, Phe) or form salt bridges (Asp or Glu). Tyr, Val, and Phe confer silk a propensity for β-sheets, while Aps and Glu have a high propensity for helices.123

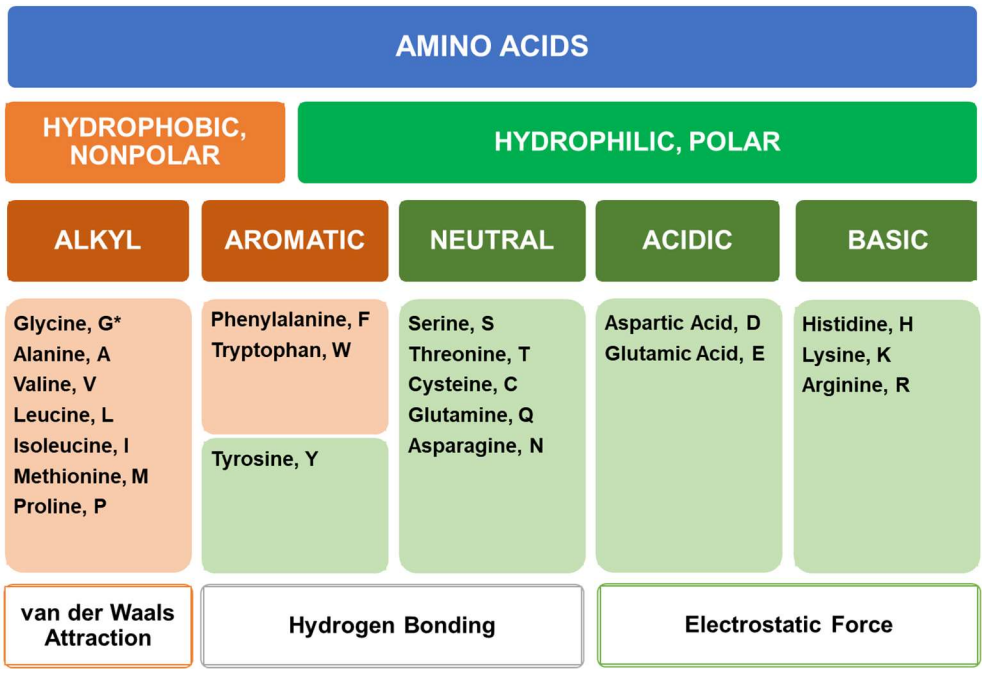

Figure 17. A schematic listing the amino acids in the silk heavy chain, categorized by hydropathy, polarity, charge, and tendency for nonbonding interactions. 122

Table 3 denotes the abundance of all amino acids in the silk backbone and their most likely interactions with other silk molecules, SiO2, GO, and rGO. The colors indicate the following: red – electrostatic repulsion, green – electrostatic attraction, blue – van der Waals attraction, and yellow – hydrogen bonding. Partial translucence indicates that the presence of a specific nonbonding interaction but to a lesser extent.124 Although the heavy chain is mostly hydrophobic, over 20% of the amino acids have polar or aromatic side groups that enable silk to adsorb to hydrophilic, polar surfaces like SiO2 and GO as well as mediate substrate sensitive assembly. Silk molecules hydrogen bond, form salt bridges, and exhibit van der Waals attraction to other silk molecules and to assemble into β-sheets as well as helices and random coils. GO flakes have an anionic, polar surface with oxide functional groups, and each flake consists of an aromatic lattice. The surface can engage in hydrogen bonds, salt bridges, and π-stacking with hydrophobic and hydrophilic moieties thanks to its heterogeneity and local amphiphilicity. This makes for strong inter-sheet intermolecular bonds as well as GO-silk bonding.

Table 3. The amino acid composition of Bombyx mori heavy chain and their potential nonbonding interactions with silk, SiO2, GO, and rGO.

Amino Acid	Abundance (%)	*Potential Interfacial Nonbonding Interactions*			
		Silk-Silk	Silk-SiO2	Silk-GO	Silk-rGO
Cationic					
Arginine	0.3				
Histidine	0.1				
Lysine	0.2				
Anionic					
Glutamic acid	0.6				
Aspartic acid	0.5				
Neutral					
Serine	12.1				
Threonine	0.9				
Asparagine	0.4				
Glutamine	0.2				
Cysteine	0.1				
Aromatic					
Tyrosine	5.3				
Phenylalanine	0.6				
Tryptophan	0.2				
Alkyl					
Glycine	46				
Alanine	30				
Valine	1.8				
Proline	0.3				
Isoleucine	0.2				
Leucine	0.1				
Methionine	0.1				

Initially, silk deposited on GO exhibits the hydrophobic effect and electrostatic repulsion between Glu and Asp and GO surface, which spur silk assembly to insulate hydrophobic moieties and inhibit silk adsorption, respectively. The hydrophobic effect would drive the amphiphilic silk backbone to fold with hydrophobic, β-sheet forming residues internally facing and available to form stable ordered secondary structures. Hydrophobic, nonpolar groups exposed to GO would be able to engage in van der Waals interactions with hydrophobic regions on GO surface. Externally facing aromatic and hydrophilic, neutral and basic groups would be available for hydrogen bonding and electrostatic attraction to the GO surface. The local amphiphilicity of silk and GO allows silk to

adsorb in extended morphology through hydrogen bonding and electrostatic attraction and form stable ordered secondary structures.

As on GO, silk would exhibit electrostatic repulsion overcome through hydrogen bonding. However, SiO2 has a homogenous anionic, hydrophilic surface thanks to piranha treatment prior to silk deposition, so there would be less electrostatic attraction and hydrogen bonding from acidic and hydrophobic groups that could adsorb to discrete regions of less acidity and hydrophobicity on GO flakes.

Silk adsorbs on rGO with significantly less ordered secondary structure and at higher density. The rGO flake surface is anionic, has heterogeneity, and largely hydrophobic due to removal of most oxygen containing functional groups. Silk is drawn to the surface via van der Waals attraction and the hydrophobic effect. Silk has a mostly hydrophobic backbone, so most of the chain would be able to adsorb and noncovalently bond to the rGO surface. Hydrophobic, β-sheet forming residues would then be less available for inter and intrachain bonding that stabilize β-sheets. And, hydrophobic, polar residues would be unable to hydrogen bond to rGO, inhibiting silk extension into ordered secondary structures. Thus, silk adsorbs to rGO in a dense layer of aggregated, amorphous secondary structure molecules due to the inability to hydrogen bond to the surface.

In summation, van der Waals attractive forces drive adsorption of silk in disordered conformations. Electrostatic attraction and hydrogen bonding between silk and the surface enable protein adsorption and promotes silk extension into ordered secondary structures. Spin casting further enhances silk extension to enable fibril formation. The inability to hydrogen bond with nonpolar surfaces makes shear ineffective in promoting silk assembly and crystallization on rGO.

1.11 Conclusions

Reconstituted silk fibroin interfacial interactions in composites and the contributions of these interactions to overall composite strength and utility have been explored. Reconstituted silk fibroin was spun cast on GO, rGO, and SiO2 at various concentrations, spin dynamics and speeds to study the effects of hydropathy, shear applied during composite preparation, and adsorption time relevant to laminated nanocomposite assemblies. This work shows what happens to reconstituted silk fibroin at the interface of silk fibroin-GO composites and how reduction to rGO (for conductive nanocomposites) effects silk fibroin morphology and interfacial interactions. The applied shear has been shown to significantly alter reconstituted silk fibroin secondary structure with changes being most notable at low silk fibroin concentrations.

Across the various reconstituted silk fibroin concentrations, three different self-assembled structures were observed. At high concentration (0.2 wt. %), reconstituted silk fibroin aggregates into uniform globules with average diameter of 19 nm, comparable in size to micelles reported elsewhere for reconstituted silk fibroin around this concentration in solution after several days of incubation. Then, upon reducing solution concentration by an order of magnitude (0.002 wt. %), reconstituted silk fibroin has more globule-like micelle morphology with interspersed structures like proto-fibril seeds. Reconstituted silk fibroin readily forms single molecule proto-fibrils at 0.002 wt. % characterized by β-sheet structures.

Reconstituted silk fibroin-GO electrostatic interactions and hydrogen bonding stabilize the crystalline structure, while the inability of reconstituted silk fibroin suspensions to fully It rGO surfaces preserves random coils and helices characteristic of its solution state which is then locked in place by rapid solution removal when spun dry. The hydrophobic substrate renders reconstituted silk fibroin impervious to shear or dilution induced elongation. Moreover, simulation results provide molecular-level insight into understanding the dynamics and interactions of silk fibroin on substrates with different surface chemistry and the concurrence of experiment with simulation has enabled investigation of intermolecular interactions acting at the interface of silk fibroin and the

substrate at the point of initial surface adsorption. This combined with the lack of differentiation in morphology when different spin speeds for samples prepared at the same concentration and on the same substrate show the importance of initial surface adsorption on overall interfacial interactions in the SA-LbL composite samples.

In summary, the results show that protofibrils form at low concentrations while variance in the deposition speed has little effect on silk secondary structure and morphology. However, balanced non-bonded interactions between electrostatic and van der Waals contributions can lead to silk secondary structure retention on the GO surface. Molecular dynamics simulations of silk fibroin at different surfaces show that strong van der Waals interactions play a pivotal role in losing and disrupting secondary structure on graphene and SiO2 surfaces. Fine tuning silk fibroin structure on heterogeneous graphene-based surfaces paves the way towards development of biomolecular reinforcement for biopolymer-graphene nanocomposites.

PROTEIN ASSEMBLY AND NANOCOMPOSITE TOUGHNESS

1.12 Overview

The findings from Chapter 4 were applied to improve GO nanocomposite design through manipulation of reconstituted silk fibroin secondary structure and morphology adjustments. Silk secondary structure is highly susceptible to shear-induced elongation and reordering into β-sheets on hydrophilic substrates. By incorporating synthetic layers of mixed hydropathy, one may control the ability of silk fibroin to hydrogen bond with heterogeneous substrates. Overall crystallinity and β-sheet arrangements can be tuned but high β-sheet content alone does not facilitate stress distribution which is required to improve robustness and toughness. Here, ultrathin, robust silk fibroin-GO nanocomposite were fabricated using SA-LbL. This chapter probes how shear inducing silk fibroin crystallization imparts added mechanical reinforcement to silk fibroin-GO laminated composites. silk fibroin assembly was captured using high resolution AFM complimented by ATR-FTIR. Mechanical effects were quantified using a bulging apparatus.

Laminated nanocomposites were prepared via dSA-LbL assembly of bilayers of silk fibroin confined between reinforcing GO flakes. Attenuated total reflectance FTIR indicated increased crystalline β-sheet content in silk fibroin secondary structure for dSA-LbL nanocomposites. Enhanced surface interactions resulting from rapid solution removal during dynamic spinning yielded outstanding mechanical properties. The mechanical properties of GO-silk fibroin nanocomposite were characterized by the bulging technique, from which the tensile modulus of 170 GPa, the ultimate strength close to 300 MPa, and the toughness above 3.4 MJ m-3 were determined, being all exceptional characteristics. The failure modes observed for these membranes suggested the self-reinforcing mechanism of adjacent GO sheets with strong binding 2-nm-thick silk interphase of individual backbones. The failure analysis by high-resolution TEM further

uncovers three hierarchical failure modes that promote the toughness by dissipating the rupture energy: compliant crack initiation, yield failure, and rupture propagation. This reinforcement leads to the effective load transfer between the GO components and introduces novel reinforced laminated nanocomposite materials with excellent mechanical strength that surpasses those known today for conventional flexible laminated carbon-based polymeric nanocomposites.

This chapter contains portion of a manuscript by Y. Yin, A. Grant; Y. Zhang, and V. Tsukruk; entitled Biopolymeric nanocomposites with enhanced interphases and published in Langmuir in 2015.

1.13 Experimental

Preparation of reconstituted silk fibroin. Silk fibroin was extracted from *Bombyx mori* silkworm cocoons as described in Chapter 3 then diluted to 0.02 wt. % and refrigerated at 5 oC.

Preparation of GO. GO flakes were prepared as discussed in Chapter 3 then diluted to 0.04 wt. % and spin cast for AFM and FTIR characterization.

Sample fabrication. Films were prepared via dSA-LbL on a sacrificial substrate. First, 2 wt. % polystyrene in toluene was spin-coated onto clean silica wafer. Then, 0.02 wt. % silk was deposited via conventional and dSA-LbL at 2000 rpm followed by the deposition of 0.04 wt. % GO at 3000 rpm. Then, this forms a single bilayer, and these steps repeated until the desired thickness reached.

High resolution atomic force microscopy. The sample topography was probed as discussed in Chapter 3 using ultrasharp tips with resonance frequency 325 kHz and spring constant 40 N m −1. Samples were characterized at 1, 5, and 20 μm with pixel sizes of 1, 5, and 40 nm, respectively.

ATR-FTIR. Silk fibroin and GO were deposited layer-by-layer onto a silicon ATR crystal while via dynamic and conventional SA-LbL. Analysis was conducted as discussed in Chapter 3.

Bulging test. Bulging tests were performed as discussed in Chapter 3.

1.14 Results and discussion

1.14.1 Fabrication and Morphology of Nanocomposite Membranes

Laminated nanocomposites were fabricated via silk deposition between GO layers by traditional SA-LbL on a static substrate and dSA-LbL on a spinning substrate. Unlike SA-LbL, dSA-LbL uses rapid solvent removal to stretch and quench silk fibroin to a substrate (Figure 17). At 0.02 wt. % silk solution and spin speeds as low as 2000 rpm, silk forms full uniform monolayers of elongated silk molecules on GO flakes. As demonstrated in the previous section, SA-LbL of higher concentrations of silk fibroin produced amorphous multilayers of bundled silk fibroin. And, higher spins speeds made too diffuse layers. Approximately 2 s was allowed for deposition to ensure the complete removal of the solvent and the fixation of the molecules. The substrate was spin cast for another 20–25 s before the next layer was deposited. Therefore, the optimal spinning condition for silk fibroin layer was determined to be 2000 rpm with 45 s between depositions. The solution concentration was limited to 0.02 wt. % because higher viscosity adversely affects the film uniformity. It is critically important that with the substrate vigorously spinning the silk solution spreads fast and the solvent evaporates in milliseconds, resulting in the major difference and advantage over the conventional LbL techniques as discussed below.90 High-resolution AFM height images in Figure 17 show the uniform surface distribution of the silk biomacromolecules without signs of significant aggregation (Figure 17). Note that samples were diluted to produce the images shown.

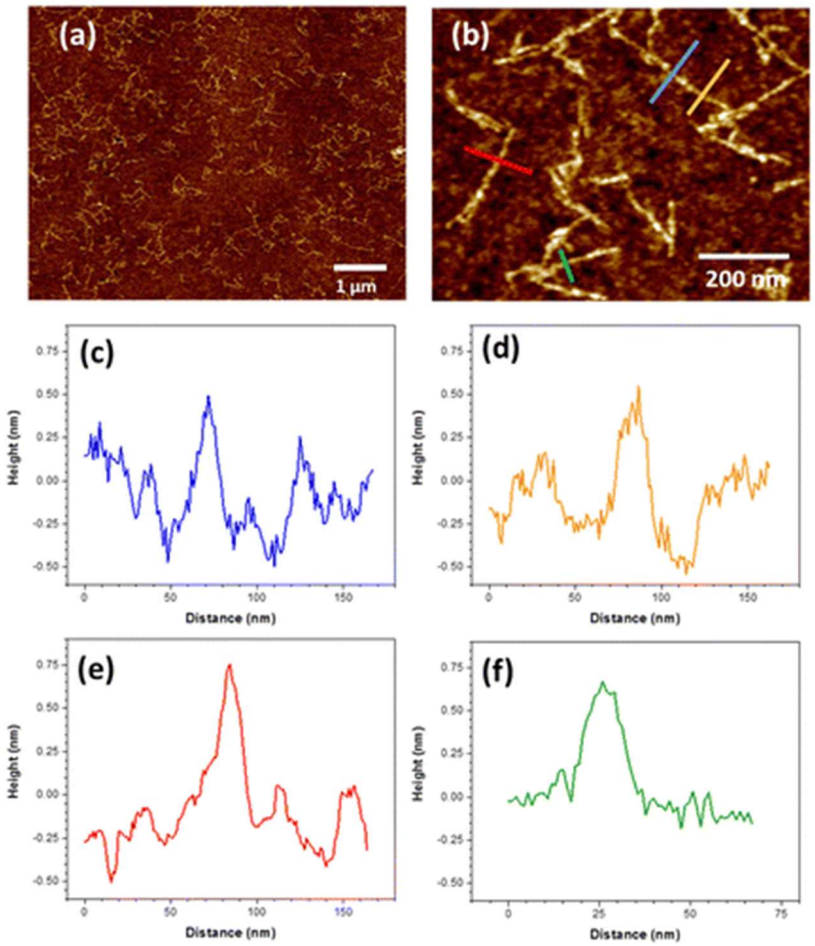

Figure 18: Morphologies of the stretched silk fibroin on GO surfaces. (a, b) Survey and high-resolution AFM images showing the uniform distribution of silk fibroin molecules without significant aggregation or entanglement (z-scales: 2 nm). (c–f) Cross-sectional profile of the single molecules from the color-coded lines in (b).

Silk deposited by conventional SA-LbL exhibits aggregation into nanofibrils, bundles, and globules, whereas silk forms a dense network when deposited by dSA-LbL. The diameter of dSA-LbL silk backbones was measured to be 0.8 ± 0.2 nm, which is close to the natural diameter of silk backbones with occasional bulky side groups of amino acids (Figure 18). The unfolding and stretching of the silk backbones by the dynamic deposition process is critically important for exposing the polar moieties along the backbone and forming high-density hydrogen bonding and other attractive like interactions between individual segments of the silk backbones and the GO

surfaces with random distribution of oxidized functionalities. Such maximization of interfacial interactions results in strong anchoring of the individual biomacromolecules to GO surface.

In addition, the molecular secondary structures of silk under the dSA-LbL processing have also altered significantly. High-resolution deconvoluted FTIR spectra of the silk fibroin after the two different type of spin coatings has been presented in Figure 18. The vibrational bands centered at around 1625 and 1680 cm–1 have been assigned to the antiparallel β-sheets and β-turns, respectively, which are corresponding to the crystallinity of the silk; the bands around 1659 and 1646 cm–1 are from the vibrations of the α-helices and random coils of the silk chains, respectively.121 From the comparison of the secondary structure composition resulted from the dSA-LbL and the conventional SA-LbL shown in Figure 18, it is clear that the dSA-LbL assembly transformed around 20% of the random coils to β-turns, indicating a higher crystallinity induced by material shearing. And the increased fraction of β-turns in the crystallized portion of silk also suggests a less ordered crystallinity, incurring the quenching effect of the dSA-LbL deposition as will be discussed in detail elsewhere.

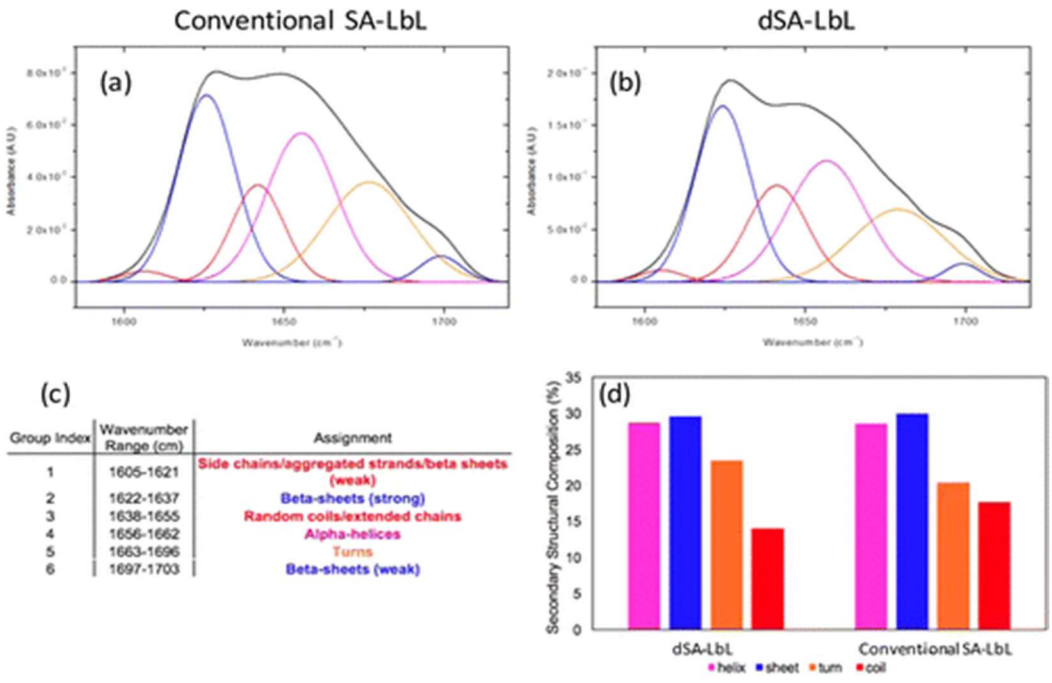

Figure 19: FTIR spectra of the silk spun using the (a) conventional SA-LbL and (b) dSA-LbL. (c) Peak assignment of the FTIR spectra. (d) Composition of the secondary structures of the silk.

The GO-silk fibroin dSA-LbL laminated composites fabricated for mechanical analysis had 15-bilayers forming a 45 nm thick membrane. The average bilayer thickness for dSA-LbL silk was 3.1 ± 0.4 nm, less than that of traditional SA-LbL films.32 The thickness of films was also independently confirmed by ellipsometry measurements, and LbL confirmed by linear increase in membrane thickness with each bilayer added. The root-mean-square surface microroughness, as measured within an area of 1 μm × 1 μm, was 5.1 ± 2.9 nm, like that of GO–silk fibroin multilayered films previously studied in the Tsukruk research group.32

Multipeak fitting of XRD data also confirms the decrease thickness (Figure 19). The broad peak at 2.6° represents the first-order diffraction peak with the average spacing of 3.3 nm that corresponds to the data obtained from AFM and ellipsometry. The diffuse halo at 5.5° suggests 1.5 nm interplanar distance within β-sheet nanocrystals.3 Using the Scherrer equation, the estimated stacking number of the GO–silk fibroin bilayer structure was about 8 for the 70-bilayer film, indicating a partially ordered layering.125 The β-sheet nanocrystals were about 3.2 nm in thickness.15

1.14.2 Mechanical Properties from Bulging Experiments

The mechanical properties of the GO–silk fibroin nanocomposites were characterized using the bulging technique, which was pioneered for mechanical analysis of freestanding ultrathin films.3,109,126,127,128,129,130 GO-silk fibroin membranes were suspended over a 300 μm diameter aperture. Puffs of air were applied to the membrane, and its deformation recorded by an interferometer. This experiment produced stress-strain data using a known procedure.32 Young's modulus, ultimate strain, ultimate stress, and toughness were derived from this data. The ultimate

strain and stress were recorded at the maximum deflection for the nanocomposite membranes before the breaking point (Figure 23).

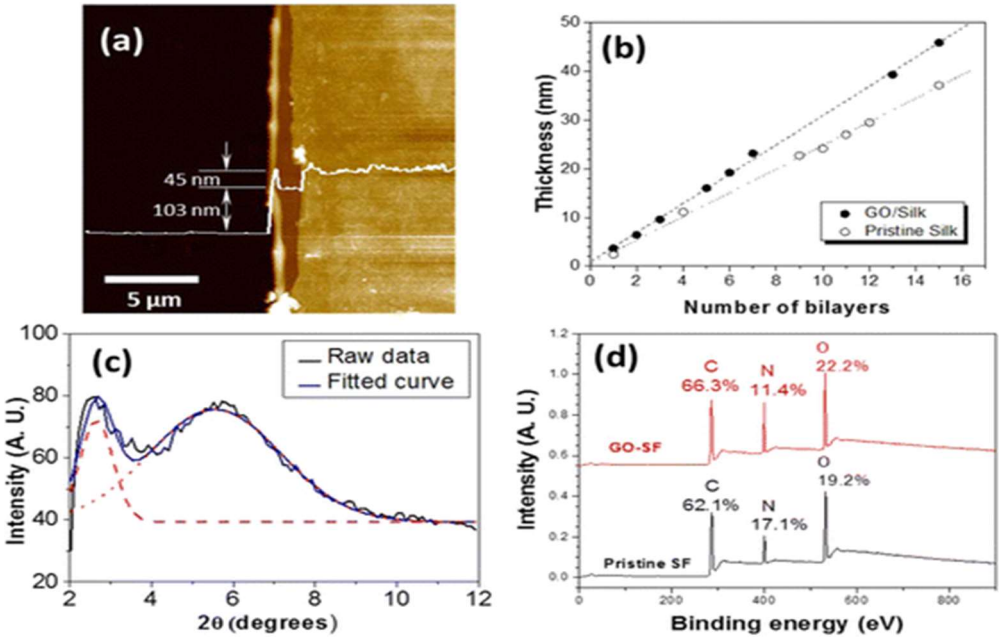

Figure 20: Structure and composition of the GO–silk fibroin nanocomposite membrane. (a) AFM image and height profile of film edge (z-scale: 350 nm) showing the 45 nm thick GO–silk fibroin nanocomposite membrane on top of the 103 nm thick sacrificial PS layer. (b) Ellipsometry data show that the thickness of the membranes increases linearly with the number of the GO–silk fibroin bilayers assembled. (c) XRD data and peak fitting of a 70-bilayer GO–silk fibroin dSA-LbL membrane on silicon wafer. The silicon wafer background is subtracted. (d) XPS of the-e GO–silk fi-broin nanomembranes in comparison with that for pure silk films.

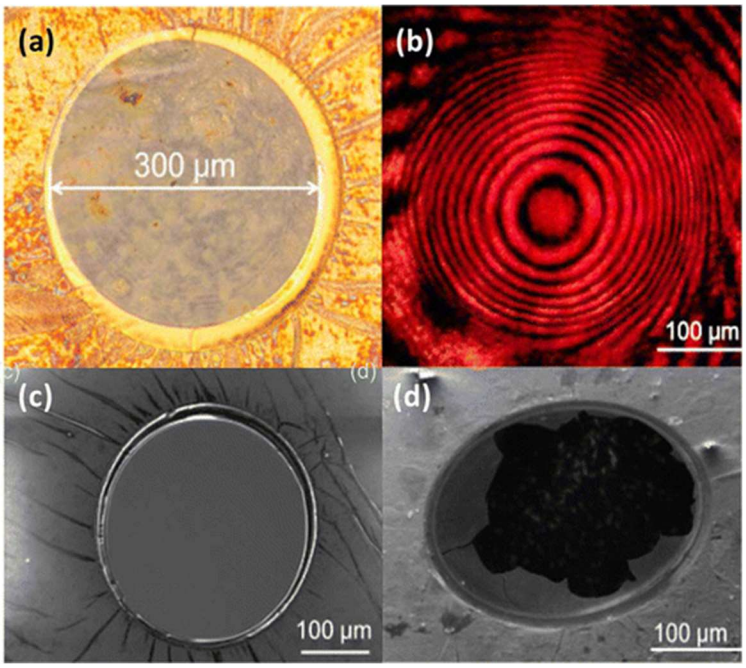

Figure 21: (a) Optical image of the GO–silk fibroin nanocomposite membrane suspended across a 300 µm copper aperture. (b) Interference pattern on the deflected membrane during bulging measurement. (c) SEM image of the freely suspended nanomembrane before and (d) after bulging measurements (the membrane is fractured).

Stress-strain data was calculated from data in Figure 21. Silk deposited by dSA-LbL and SA-LbL had elastic moduli of 12 ± 1 GPa and around 10 GPa, respectively. Their difference in modulus illustrates the strengthening induced by preferential silk fibroin assembly when deposited by dSA-LbL.32 Calculated moduli were fitted with the Halpin-Tsai model as it models for randomly oriented nanoparticles within a matrix like β-sheet crystals are nanoconfined with the silk fibroin amorphous matrix.9,131 The Young's modulus of random silk fibroin (silk I) and β-sheet crystals

is 4–5 GPa and around 22 GPa, respectively; thus, β-sheet crystal content is at about 63% (18% greater than ~45% β-sheets for silk in traditional SA-LbL films).3,15

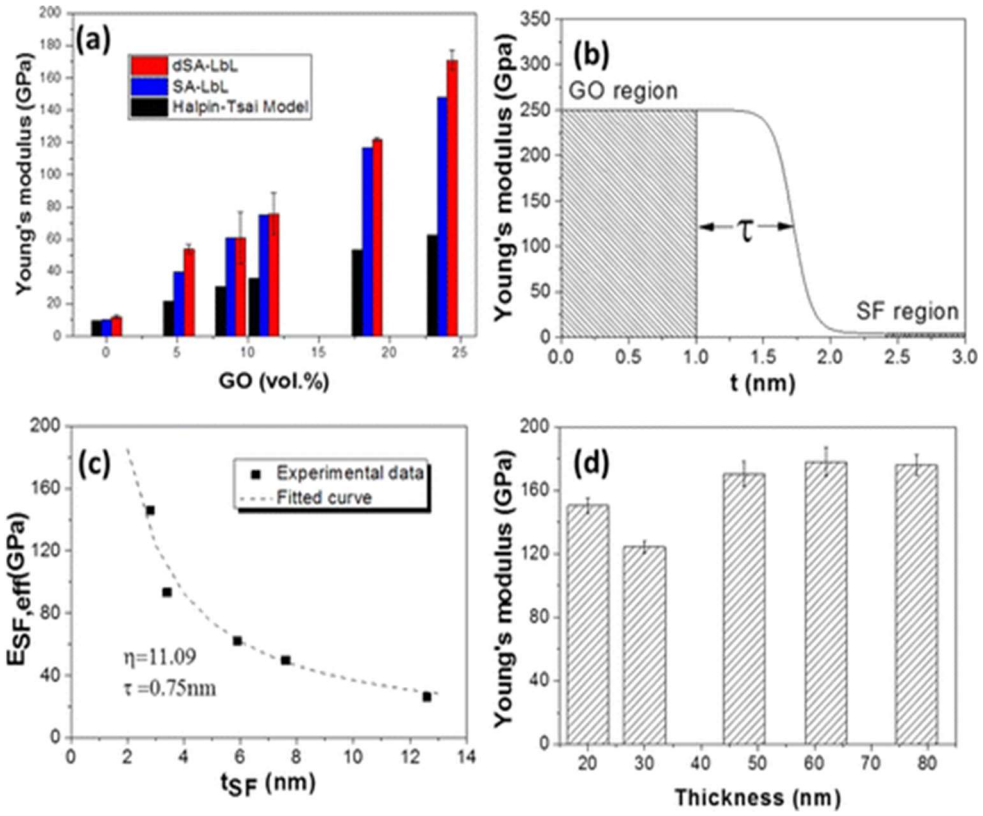

Figure 22: (A) Dependence of the Young's modulus of the GO–silk fibroin nanomembranes upon the volume concentration of GO. (B) Sigmoid decay curves for bulging tests at the interphase region. (C) Dependence of the effective Young's modulus of the silk layer on the thickness of the silk fibroin laminates. The dashed line is the fitted curve using the interphase reinforcement model. (D) Variation of the Young's modulus for membranes with different thicknesses.

The dSA-LbL GO-silk fibroin membranes had a Young's modulus of 171 ± 6 GPa at 24 vol.% GO loading, 15 times greater than SA-LbL GO-silk fibroin membranes (Figure 21). When reported in 2015, this was the highest value of the elastic modulus ever reported for flexible nanocomposites and biopolymer-based membranes.132,133,134

Each stress-strain curve shows characteristic plastic deformation, wherein initial loading causes elastic deformation then yields to before ultimate fracture (Figure 22). Increased GO loading, increases ultimate stress and strain in all samples as expected. However, dSA-LbL membrane ultimate strength is higher than those values reported for the conventional SA-LbL films thanks to their increased reinforcement and stretch ability (Figure 22). This improvement can be accredited to the effective corporation of the strong and flexible sheets and the improved stress transfer induced by the enhanced interphase zone between components. Toughness at 24 vol.% GO loading for dSA-LbL films was 3.4 MJ m–3, greater than that of SA-LbL (Figure 22) and similar graphene-based nanocomposites produced about the same time.3,129,136

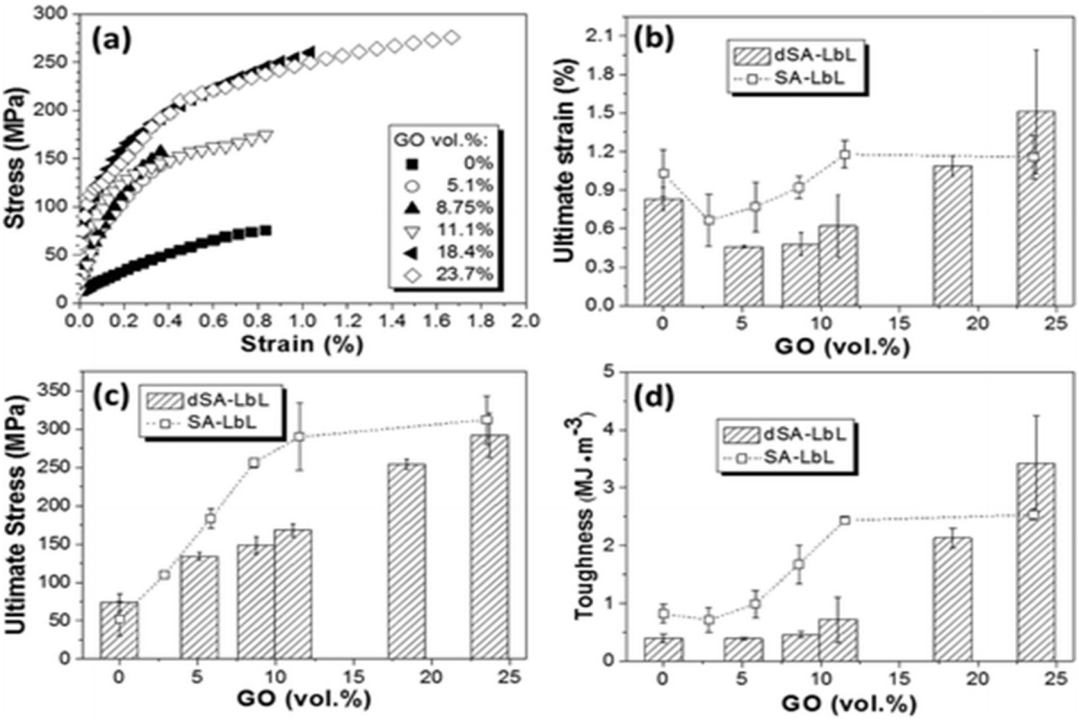

Figure 23: (a) Representative stress–strain curves derived from the bulging tests and (b) the ultimate strain, (c) the ultimate stress, and (d) the toughness as a function of the GO concentration for GO–silk fibroin nanocomposite membranes fabricated here as compared to the values for the conventional SA-LbL membranes.124

1.15 Conclusions

In summary, ultrathin silk fibroin–GO nanocomposite membranes with remarkable mechanical properties were fabricated by using the novel dSA-LbL assembly. Uniquely realized by the dSA-LbL, the strong interactions between stretched silk backbones and GO surface lead to effective load transfer between components with the interphase reinforcement. The silk–GO membranes with modest volume fraction of GO sheets show the elastic modulus above 170 GPa and a high toughness of 3.4 MJ m–3 due to 3-fold increase in the ultimate deformation as compared to conventional LbL membranes with similar chemical composition. The dense network of like interactions between the individual silk fibroin chains and GO surfaces facilitates the formation of strong molecular interphase zones of confined individual silk backbones, thus dramatically enhancing the reinforcing effect. These strong and flexible ultrathin membranes in their freely standing state can be valuable for prospective applications in sensing devices, protective molecular coatings, biological and chemical filters, cell protection and support, membranes for separation and delivery, energy harvesting, and ion separation.

SUCKERIN-12 AQUEOUS TOUGHENING

1.16 Overview

The Humboldt squid is one of the fiercest marine predators thanks in part to their sucker ring teeth that are biopolymer blends of a protein isoform family called suckerin. The suckerin polymorphs exhibit high compression strength that rivals that rivals silkworm silk. This work focuses on the suckerin-12 isoform to understand what makes this biopolymer tough, particularly in water, and the potential role of ion crosslinking in accordance with Hofmeister series principles. By choosing a proper salt post-treatment, film stability was achieved with salt annealing that is comparable to chemical crosslinks. Stable films of suckerin-12 were formed by spin assisted deposition and crosslinked using horseradish peroxidase or via salt annealing for mechanical analysis. By correlating the film morphology with the protein secondary structure changes suckerin-12 films were shown to contract upon treatment with kosmotropic salts and exhibit increased stability as if chemically crosslinked. This strength and morphological change are coupled with rearrangement of suckerin-12 secondary structure from random coils and helices to β-sheets. Overall, refining protein film stability via controlled transformation of the secondary structure caused by changing ionic environment with established trend can be instructive for the ultimate tuning of the suckerin film sclerotization and converting to tough biological materials.

This chapter contains portions of a manuscript in preparation by A. Grant, M. Krecker, M. Gupta, M. Crosby, and V. Tsukruk; entitled Enhancing marine protein stability via Hofmeister salt annealing and enzymantic crosslinking.

1.17 Experimental

Suckerin preparation. Suckerin-12 expression plasmids was obtained from Genescript. Horseradish peroxidase and Hofmeister salts ($NaC_2H_3O_2$, $Na_3C_6H_5O_7$, Na_3PO_4, Na_2SO_4) were obtained from Sigma Aldrich. Then, suckerin-12 expression and purification were conducted as discussed in Chapter 3.

Sample preparation. Thin films of suckerin-12 were prepared via spin casting at 3000 rpm for 30 s. First, polystyrene (PS) at 2 wt. % was spun cast onto a silicon wafer as a sacrificial layer. Then suckerin-12 was drop and spun-cast at 1 and 3 wt. % to produce homogenous films. Free standing films were made by spin casting on a PS layer. Half of the samples were then crosslinked using a solution of 40 units/mL HRP and 0.02 v/v % of H_2O_2. The sample was covered in the HRP – H_2O_2 solution then left in a humid environment at ambient temperature for 24 hr. The samples were then rinsed with 18 MΩ cm Millipore water and allowed to dry in air. Crosslinked and uncrosslinked films of suckerin-12 were treated with Hofmeister salts at 200 mM for 1 hr then rinsed off with Millipore water and air dried.

Surface spectroscopy. Suckerin-12 secondary structure and chemical composition were evaluated using FTIR and XPS as discussed in Chapter 3.

Scanning mechanical, topographical, and optical spectroscopy. SPM of suckerin-12 morphology and modulus properties were captured as discussed in Chapter 3 for AFM, QNM, and FDS.

Sample thickness was measured using AFM of scratched and a Woollam M2000U variable-angle spectroscopic ellipsometer with a wavelength range of 245–1000 nm. Generally, a Cauchy model was applied to model the 620-1000 nm region of the optical spectrum.111 Optical images were obtained using a Leica DM 4000M microscope to evaluate macroscopic morphology changes and phase separation.

1.18 Results and discussion

1.18.1 Concentration and deposition mode dependent film formation.

The hexahistidine-tagged suckerin-12 isoform (His-suckerin-12) was used in this study because of its relatively high expression levels in E. coli as discussed in a recent study (Figure 1).47 Initial experiments sought to determine the effects of protein suspension concentration (1 and 3 wt.%) and deposition mode (drop versus spin cast) on suckerin-12 film morphology. Figure 23 shows AFM topographical images of drop and spin cast suckerin-12 at 1 wt. %. Both films exhibit a low microroughness, grainy texture under both conditions with fewer large aggregates observed after spin casting. The drop and spin cast films had a root mean square (RMS) roughness of 0.40 ± 0.08 nm and 0.40 ± 0.08 nm, respectively. For all roughness measurements quoted below, RMS roughness was measured from 1 um2 surface areas at five different points in 5 um topographical images.

Spin assisted deposition was used to prepare homogenous films from 3 wt. % suckerin-12 formation with few large aggregates. At this higher concentration, the film surface is composed of densely packed globules and aggregates with larger-scale surface modulations not seen at 1 wt.% (Figure 23). Phase images show no phase separation of films deposited, suggesting that the suckerin films were homogenous and stable after film formation and drying (Figure 41). Optical images taken during the film deposition process also depict relatively homogenous surface and the de-wetting pattern observed in AFM (Figure 42). The large-scale modulation indicates an initial de-wetting which is arrested during drying. The average roughness of the 3 wt. % suckerin film is six-times greater (1.8 ± 0.1 nm) than 1 wt.% film, which reflects some reorganization of surface morphology. Given that RMS roughness is measured in areas smaller than the overall modulation periodicity (microns), the measurement represents the local microroughness of the densely packed biomacromolecules. The higher viscosity of the 3 wt.% suspension likely causes the increase in

microroughness and partially de-wetting observed (Figure 23). Overall, 3 wt.% was the highest concentration at which the solution is spinnable and forms a uniform thin film, so it was used for further studies into salt annealing and enzymatic crosslinking.

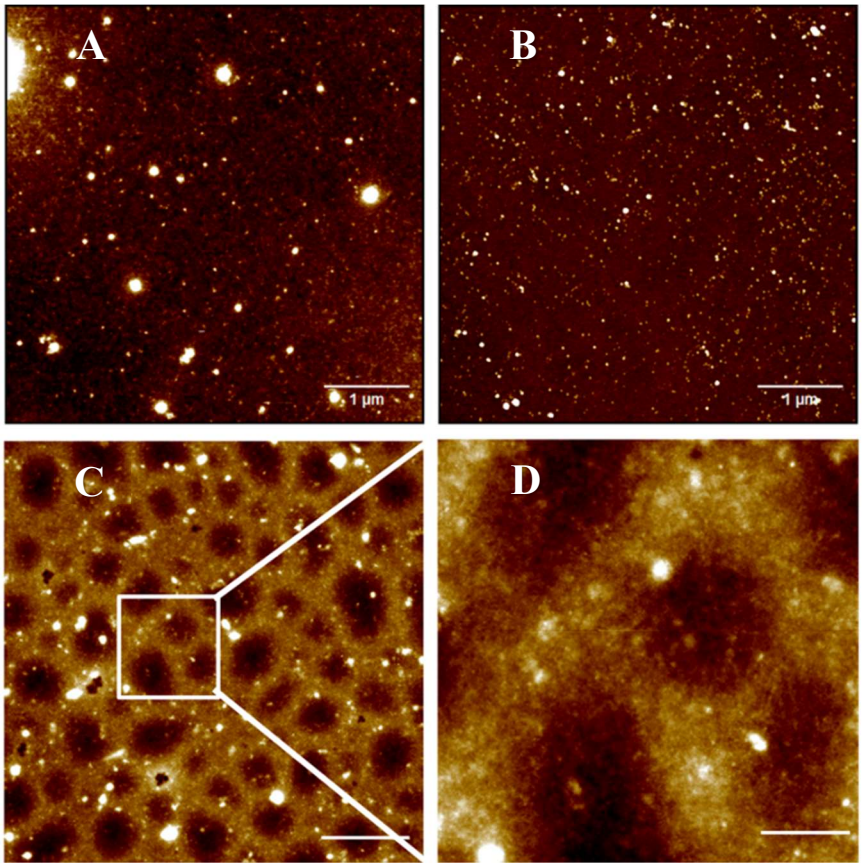

Figure 24. AFM topographical images of suckerin-12 at 1 wt.% when drop cast (A) and spun cast (B) as well as spin cast suckerin-12 at 3 wt.% (C) with an inset (D) to show surface modulations. Scale: 1 um (A, B, D) and 4 um (C). Z range: 5 nm (A and B), 52 nm (C), and 40 nm (D).

ATR-FTIR was used to characterize the changes in secondary structure that accompany the morphological effects discussed above (Figure 24). ATR-FTIR spectra analysis focused on shifts in absorption at the amide 1 peak (1600-1700 cm-1) because it represents amine bonding and exhibits individual peaks for characteristic secondary structures, i.e. β-sheets (1622-1637 and 1697-1703 cm-1), random coils (1638-1655 cm-1), α-helices (1656-1662 cm-1), β-turns (1663-1696 cm-1), and β-sheets/aggregates (1605-1621 cm-1) (Figure 24). The secondary structure composition of each sample was calculated via peak deconvolution using OriginPro to identify the subpeaks

associated with the features previously listed then fit them to the data using a Guassian function.32,121 β-sheets, β-turns, and helices are ordered structures found in more crystalline materials, and each is stabilized by hydrogen bonds. Random coils are amorphous secondary structures. The ratio of crystalline motifs (β-sheets, β-turns, and helices) to amorphous motifs (random coils) represents relative crystallinity. By tracking the shift in distribution of these motifs, it was possible to better understand the mechanism driving their change and self-assembly. Drop cast suckerin-12 has a largely helical secondary structure with β-sheets, random coils, and β-turns in the minority (listed in order of highest prevalence). Neat suckerin-12 exhibits a max at 1650 cm-1 (random coils) and secondary shoulder over 1625 cm-1 (β-sheets) and 1660 cm-1, which indicates semi-crystalline secondary structure. At the same time suckerin-12 film roughness and aggregation appearance reduce, ATR-FTIR shows an accompanying increase in film crystallinity (Figure 24). Furthermore, circular dichroism (CD) was conducted to verify observations from ATR-FTIR, similarly in Figure 24, CD curves exhibited a deep trough at 220 nm that suggests a heightened presence of random coils (dip at 205 nm) and helices (troughs at 203 and 223 nm). CD of spin case suckerin-12 exhibits a peak at 190 nm and trough at 210 nm, which are characteristic of β-sheets, along with a slight shoulder at 205 nm that indicates the presence of random coils.

Considering the spectroscopic and morphological analysis together, these results suggest that suckerin-12 undergoes shear induced crystallization when spin cast which is characterized by decrease in both film roughness and presence of large aggregates. The morphological and structural effects observed are in good agreement with previous studies on semi-crystalline structural proteins, i.e. silk fibroin during deposition from solution.17,137 Additionally suckerin-12 reacts similarly to silk fibroin when spun, stretching from amorphous random coils to organize in ordered structures like β-sheets and locked into place via rapid solvent removal.22 The susceptibility of suckerin-12 to shear induced crystallization also suggests that suckerin-12 could form crystalline nanotubular assemblies as observed in cross-sections of sucker ring teeth where they provide

additional film reinforcement.137 In spite of the structural changes observed, suckerin-12, which readily dissolved in water when drop cast, achieved only partial stability after spin casting. This was verified by submerging the suckerin-12 drop and spin cast films in DI water for several minutes then checking for changes in its thickness and coloring, which would indicate surface erosion and changes in film thickness.

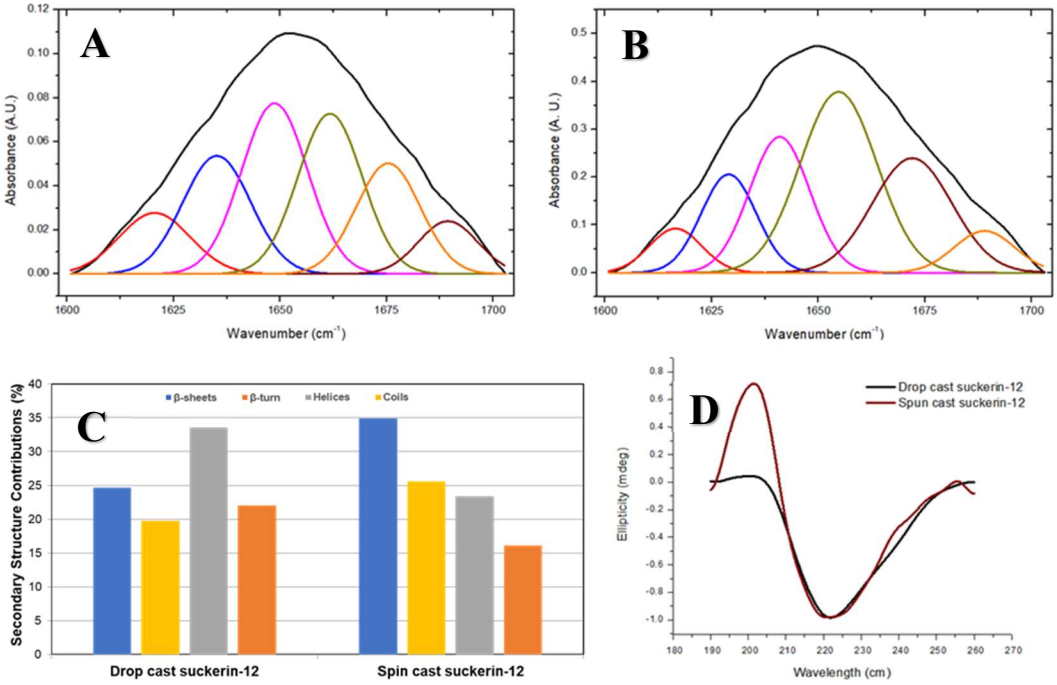

Figure 25. ATR-FTIR and CD spectra of drop (A) and spun cast (B) suckerin-12 where subpeaks are should under the overall convoluted amide 1 peak to show how FTIR spectra were analyzed for this study. The secondary structure in each sample calculated from peak area of their respective peaks is given in (C). Circular dichroism was conducted to corroborate the ATR-FTIR spectra (D).

1.18.2 Using thermal vapor annealing to drive self-assembly.

Then, the similarities between triggers for silk fibroin and suckerin-12 self-assembly were investigated using thermal vapor annealing (TVA) approach. Spin cast 1 wt.% suckerin-12 films were annealed at 60 oC, at high humidity and ambient pressure for 12 hr. Suckerin-12 films appeared smoother in AFM topographical images after TVA treatment (Figure 4). RMS roughness was virtually the same at very low value of 0.40 ± 0.04 nm with overall fewer large surface

aggregates visible. After annealing, the film surface exhibited a mesh-like morphology in which the globular protein has oriented into a connected network with nanoscale domains spreading across the entire surface (Figure 25).91 During TVA, the supply of thermal energy enables suckerin-12 to mobilize, while the vapor molecules promote reorganization into ordered structures like β-sheets, β-turns, and helices. Suckerin-12 is amphiphilic so, in the presence of water, the hydrophobic effect drives it to reorient into conformations that insulate hydrophobic segments from the water molecules.

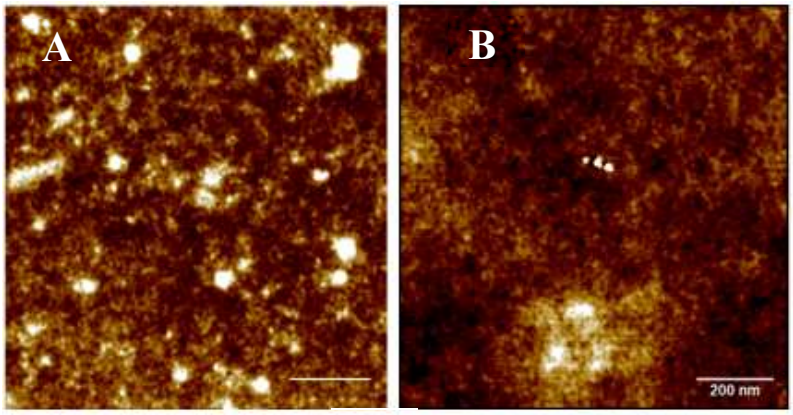

Figure 26. AFM topographical images of 1 wt.% suckerin-12 before (A) and after (B) TVA for 12 h. Scale: 200 nm. Z range: 4 nm.

The assembly mechanism is further examined via concurrent spectroscopic measurements. ATR-FTIR of TVA samples show a clear red shift towards 1620 cm-1, indicating increased β-sheet content and thereby crystallinity (Figure 26A). The amide 1 peak was fitted for six sub-peaks related to the four major secondary structures and their contributions summarized in Figure 26B. Comparing the secondary structure composition before and after, note that coils and helices seemed to have converted to β-sheets while β-turns, which are part of β-sheets, remain constant (Figure 4). In fact, β-sheet content increased 10% after TVA. Results of spectroscopic and morphological analysis show that controlling the amount of structural water surrounding suckerin-12 could be one-way nanotubular assemblies are achieved in nature. The significant shift in morphology and crystallinity also rendered both drop and spin cast suckerin-12 films relatively insoluble in water.

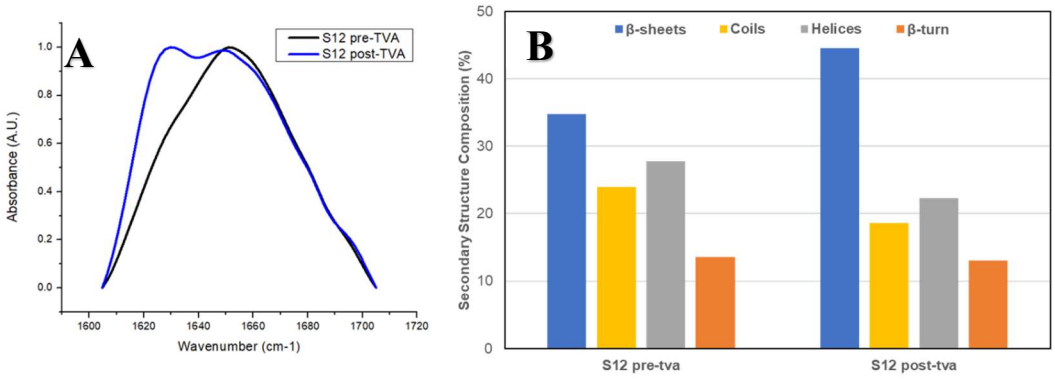

Figure 27: ATR-FTIR spectra of crosslinked suckerin-12 films in the amide 1 region before and after TVA (A) and secondary structure composition in initial film and after annealing (B).

Noting the relative aqueous solubility after vapor annealing, the mechanical reinforcement rendered by this treatment was characterized. The film surface mechanics were studied using FDS to measure the average local stiffness, respectively. FDS was the best method to interrogate the film mechanical properties given their general sub-micron film thickness. Force distance curves from FDS were analyzed using nonlinear optimization with MATLAB software, wherein the Hertzian model and elastic approximation were applied as discussed in prior work.138 The FDS mapping has a limited range of reliability that peaks around 50 GPa, and the tip used to interrogate the surface has a reliability range of approximately 1 MPa to 40 GPa.139 Despite these limitations, the elastic moduli for the thermal vapor annealed suckerin-12 films were at least double commonly reported values with 18 and 34 GPa for drop and spin cast films, respectively (Figure 27). And, it seems that spin casting enhances the effect of thermal vapor annealing. Thermal vapor annealing allows for conversion of secondary structure motifs to β-sheets, making the film more crystalline. Spin casting, as a pre-step, elongates the peptide and thus makes for more efficient rearrangement during thermal vapor annealing.

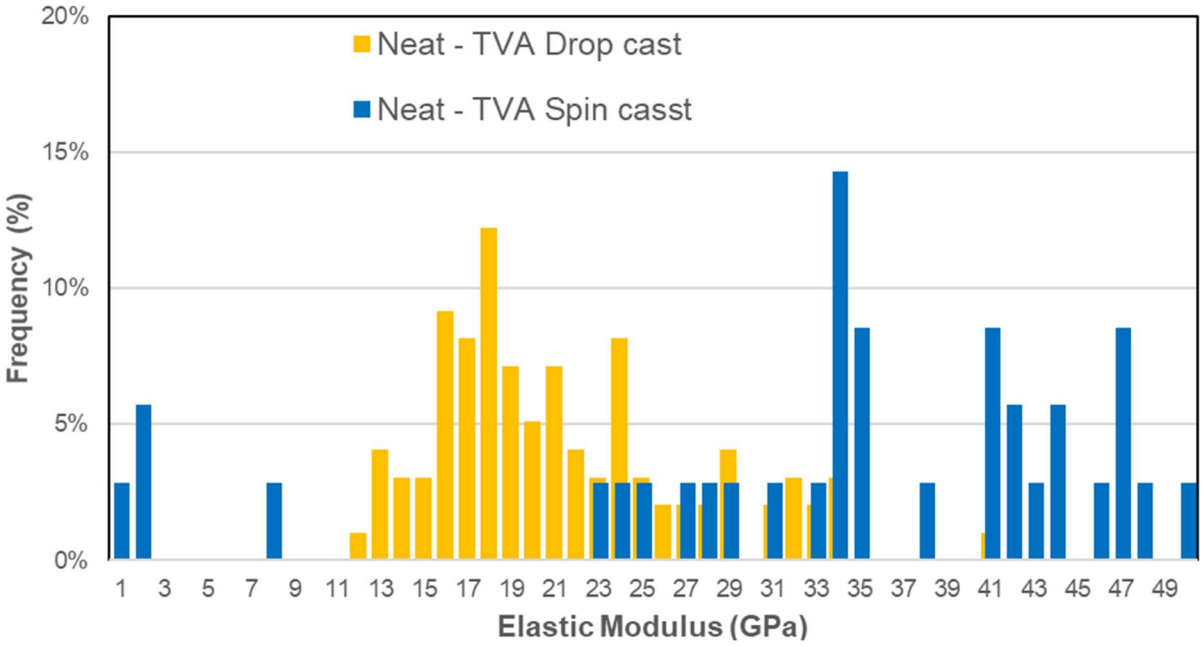

Figure 28. Histogram of FDS measured moduli for drop and spin cast suckerin-12 films after thermal vapor annealing.

1.18.3 Hofmeister salt aided stabilization and crystallization.

The environment in which suckerin assembles and functions is both aqueous and highly saline. The preceding experiments briefly show that water alone can free suckerin-12 to rearrange into more crystalline assemblies with aqueous stability. Here, the role of anions, which are abundant in seawater, were characterized on suckerin-12 assembly and crystallization. Specifically, the influence of kosmotropic Hofmeister salts on aggregation and intermolecular bonding in suckerin-12 film was studied. Spin cast suckerin-12 films were annealed in 200 mM salt solutions for 1 hr then air dried prior to characterization. Treatment with kosmotropes resulted in suckerin-12 films with rougher surface morphology, consisting of densely-packed protein globules (Figure 28). RMS microroughness values with Na3PO4, NaOAc, Na3C6H8O7, and Na2SO4 were 3.0 ± 0.3, 3.1 ± 0.3, 3.2 ± 0.5, and 2.2 ± 0.4 nm after treatment, respectively, corresponding to three-fourfold increase in roughness compared to neat suckerin-12. Salt annealing also had a distinct effect on the film thickness wherein most of the salts induced contraction of the suckerin-12 composite by at least 4% from 74 to 70 nm, 83 to 79 nm, and 116 to 102 nm for Na3PO4, Na3C6H8O7, and

Na2SO4, respectively (Figure 53). NaOAc treatment did not resulted in an increase in thickness (within 66 to 67 nm). The lack of contraction after NaOAc treatment may be related to the low kosmotropic ranking of acetate.140

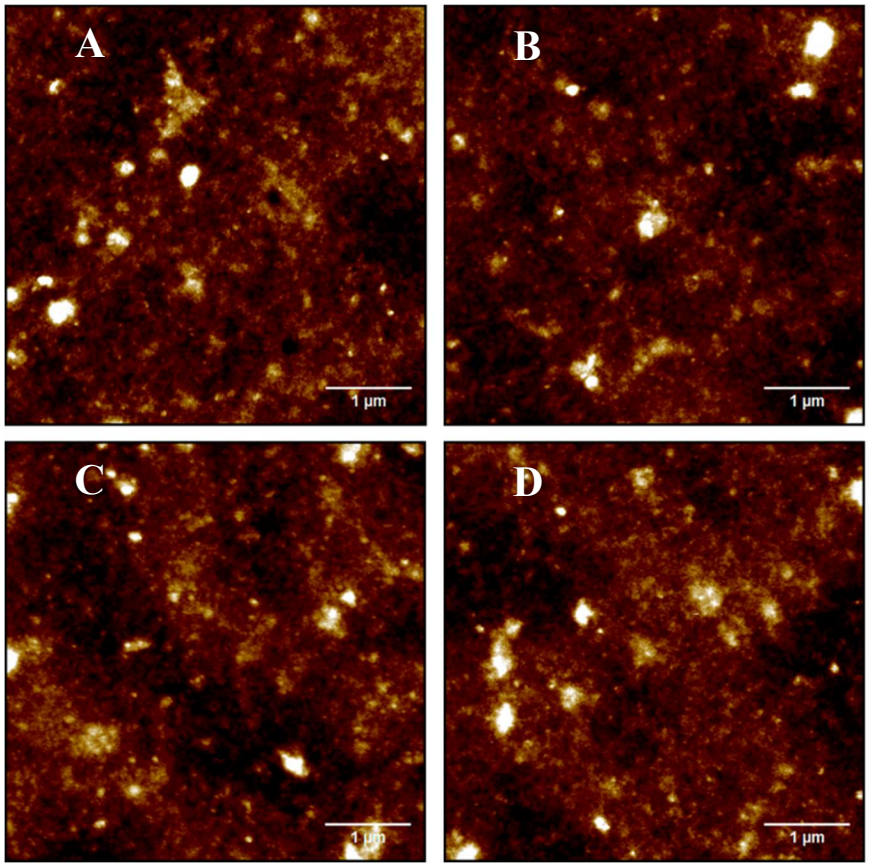

Figure 29. AFM topographical images of 3 wt.% suckerin-12 after salt annealing for 1 hr with sodium phosphate (A), sodium acetate (B), sodium citrate (C), and sodium sulfate (D). Scale: 1 um. Z range: 33 nm (A), 38 nm (B), 30 nm (C), and 36 nm (D).

ATR-FTIR of suckerin-12 films after kosmotrope treatment exhibited a red shift in the amide 1 peak from a 1650 cm-1 centroid to 1642 cm-1 and appearance of a shoulder peak at 1628 cm-1 (Figure 29A). The shift was strongest for NaOAc, Na3C6H8O7, and Na3PO4. However, treatment with Na2SO4 treatment induces a peak broadening rather than a peak shift (Figure 29A). Deconvolution of the amide 1 peak shows that treatment with Na2SO4 results in some conversion of random coils to β-sheets while the other salts cause higher conversion or random coils overall and to both β-sheets and helices (Figure 29B).

This distinction between the effects of Na2SO4 and the other salts is consistent with a preceding publication comparing the effects of kosmotropes on suckerin-12 hydrogels.47 The study showed that immersing suckerin-12 hydrogels in salts with stronger conjugate bases lead to increased compressive modulus. Previous studies have shown that for organic and inorganic surfaces, increased crystallinity leads to increased microroughness, so the increase in roughness in Figure 6 along with increased ordered secondary structure content is reasonable.

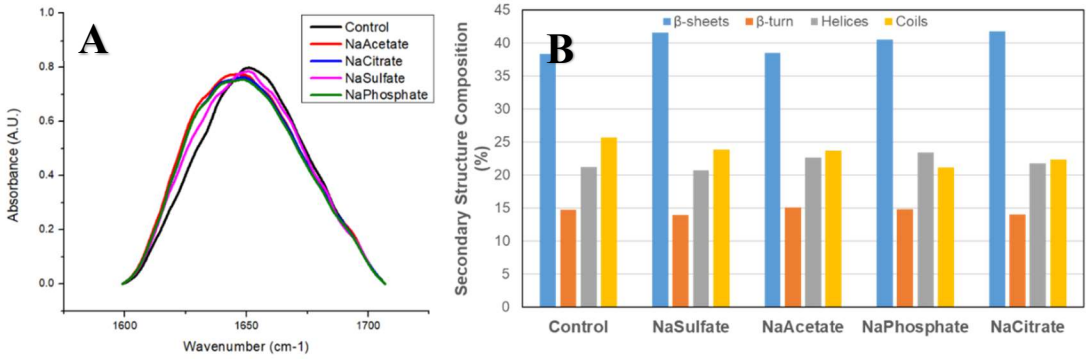

Figure 30. ATR-FTIR of the amide 1 peak of suckerin-12 neat and after salt annealing for 1 hr (A) as well as a graph of the secondary structure composition derived from deconvolution of the spectra (B).

Interestingly, the kosmotrope treatment was enough to stabilize the suckerin-12 films in water even after salt removal via rinsing (Figure 30). More spin cast suckerin-12 samples were salt annealed, characterizing their topography AFM before and after immersion in DI water. Without annealing, the suckerin-12 films dissolved within moments of submersion in DI water. When salt annealed, the suckerin-12 film surface exhibits surface aggregates but is otherwise homogenous and intact indicating aqueous stability salt annealing (Figure 30). As a next step, the effects of salt annealing were compared to enzymatic crosslinking.

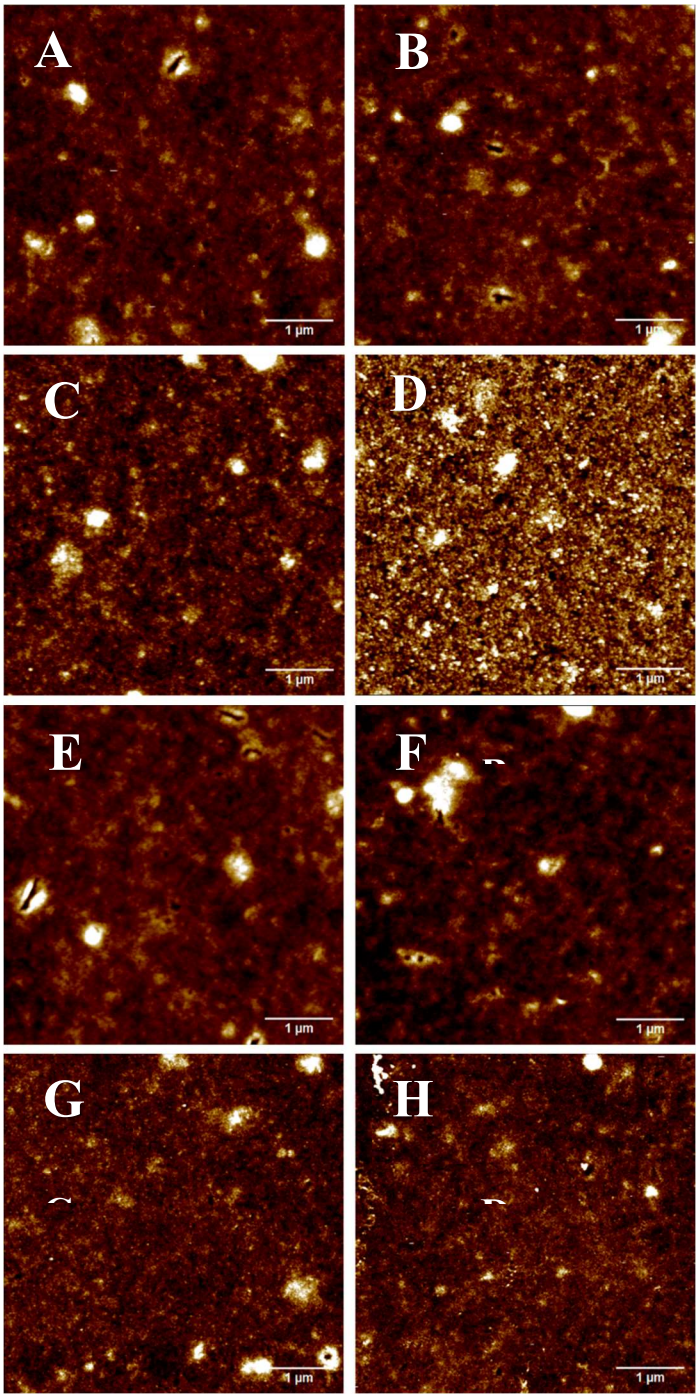

Figure 31. AFM topographical images of salt annealed 3 wt.% suckerin-12 films before (A, C, E, G) and after (B, D, F, H) immersion in water. The samples shown were neat (A, B) and annealed with sodium phosphate (C, D), sodium acetate (E, F), sodium citrate (G, H), and sodium sulfate (I, J). Scale: 1 um. Z range: 20 nm (A-H).

1.18.4 Enzymatic crosslinking for film stability.

Spin cast suckerin-12 were enzymatically crosslinked using HRP and H2O2 to form inter-macromolecule di-tyrosine bonds.47 Crosslinking was verified via FTIR conducted on neat and crosslinked films. ATR-FTIR spectra of suckerin-12 films after enzymatic crosslinking exhibit comparable shape of amide 1 peaks to the control film; however, there is a shoulder over 1620 cm-1 that indicates an increase in β-sheets as compared to the control suckerin-12 film (Figure 31).

Similar spectral shifts were observed in crosslinked silk and amyloid forming proteins which exhibit di-tyrosine crosslinks.141,142,143,144 The di-tyrosine crosslinks provide added stability to β-sheet forming peptides like those in suckerin-12--and when surrounded by other β-sheet forming residues like leucine (L), valine (V), and phenylalanine (F), as in this case.145,146,147 Previous studies have shown that di-tyrosine form mainly at the edges of crystalline domains, suggesting that the bonds aid in crystallization. 145,146

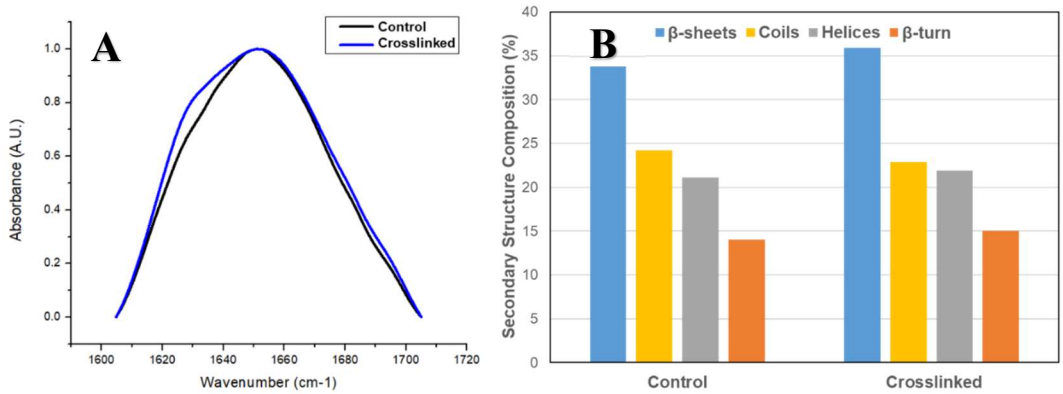

Figure 32. ATR-FTIR spectra of the amide 1 peak of suckerin-12 before and after crosslinking (A) as well as graph of the secondary structure composition derived from peak deconvolution (B).

After crosslinking, larger scale topographical images of suckerin-12 films appear to have more prominent de-wetting patterns like that shown in Figure 23. This means that the film has compacted but not undergone phase separation or macroscale rearrangement due to chemical crosslinking. There was also an increase in RMS microroughness for the enzyme crosslinked films after treatment with 200 mM of Na3PO4, NaOAc, Na3C6H8O7, and Na2SO4 to 3.1 ± 0.1, 3.5 ± 0.6, 3.6 ± 0.8, and 3.2 ± 0.7 nm, respectively (Figure 32). The modest increase in microroughness was

accompanied by film contraction. These results suggest a double crosslinking effect wherein the films exhibit chemical crosslinks from HRP and increase in secondary structure crystallinity after salt annealing.

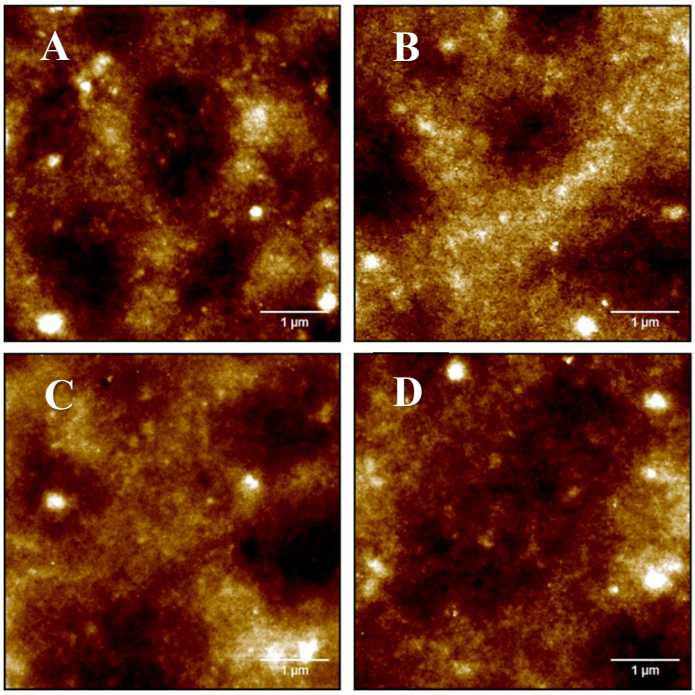

Figure 33. AFM topographical images of crosslinked 3 wt% suckerin-12 after salt annealing for 1 hr with Na3PO4 (A), NaOAc (B), Na3C6H8O7 (C), and Na2SO4 (D). Scale: 1 um. Z range: 35 nm (A), 38 nm (B, D), and 44 nm (C).

FTIR spectra of crosslinked films support this hypothesis given the enhancement in shoulder over 1625 cm-1, suggesting that salt annealing of the enzyme crosslinked films leads to further reorganization of the secondary structure into β-sheets (Figure 34). Deconvolution of the spectra in Figure 33 shows that coils were converted to β-sheets and helices during salt annealing. This is different from the effect of salt annealing on neat suckerin-12 films (Figure 7) where random coils and helices convert to β-sheets. The crosslinked films exhibit a considerable decrease in β-turns, leading to increases in helices and β-sheets. Here, it's proposed that, in addition to enhancing suckerin-12 crystallinity, di-tyrosine bonds formed by enzymatic crosslinking stabilize inter-molecular β-sheet formation and inhibit flexibility of suckerin-12 residues with a propensity for β-turns and β-sheets, so that they are more likely to form β-sheets.146 In this way, enzymatic

crosslinking seems to enable the formation of longer runs of β-sheets, or β-strands. And, as β-strands lengthen they gain stability and a propensity for α-helices.148,149 This may account for the accompanying increase in helices.

As previously mentioned, the suckerin-12 amino acid sequence exhibits motifs with high propensity for β-sheets but also β-turns thanks to their high G and Y content.47 Thus, it's proposed that salt annealing provides an aqueous environment for reorganization while the kosmotropic salts promote hydrogen bonding, which comprise β-sheets. As shown in prior work, suckerin-12 are sensitive to salts and their pH differences in solution.47 Specifically, raising the pH to above the pKa of His enables the side chain to deprotonate, giving the protein a more aromatic character. This then would enable more π-π stacking and hydrogen bonding that is characteristic of ordered structures like helices and β-sheets.

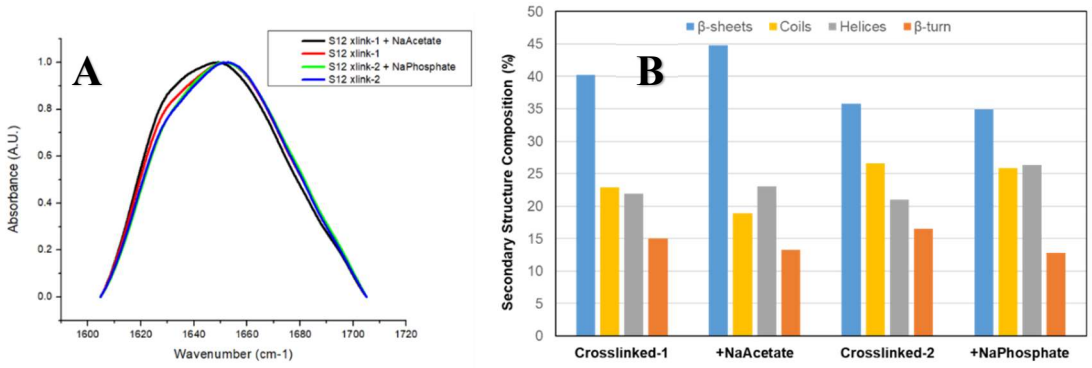

Figure 34. ATR-FTIR spectra of the amide 1 of crosslinked suckerin-12 before and after salt annealing (A) as well as the secondary structure composition derived from peak deconvolution (B).

The film surface mechanics were studied concurrent with the salt annealing and crosslinking experiments using QNM and FDS to measure elastic modulus comparatively across film surface and calculate the average local stiffness, respectively. QNM and FDS were the best SPM methods available to for characterizing the thin films. QNM yielded height, modulus, and adhesion maps as shown in Figure 35. Before crosslinking, the suckerin-12 film exhibits relative homogeneity in height and adhesion surface distribution while the modulus mapping shows a grainy surface texture,

indicating a varied surface stiffness (Figure 35). After crosslinking, the films remain relatively homogenous, but the modulus map is grainier, and the adhesion map exhibits higher contrast. The relative homogeneity before and after crosslinking confirms the suitability of these films for FDS via probing across the film surface to measure the apparent elastic modulus.

Force distance curves from FDS were analyzed as previously mentioned. QNM of select samples show that films did not exhibit clear signs of phase separation or large-scale inhomogeneity at least in topography and adhesive force during characterization (Figure 34). Elastic moduli for neat and crosslinked films with and without salt annealing were compiled into histograms in Figure 35. Moduli for non-crosslinked films appears centralized about 3-5 GPa, except for neat and NaAcO treated suckerin-12 which exhibited a broader distribution of moduli (Figure 35). The more kosmotropic salts seem to improve film mechanical homogeneity and increase β-sheet content as shown via FTIR through the conversion of random coils to β-sheets. However, NaAcO more so converted coils to helices and ultimately produced films with greater mechanical inhomogeneity.

After crosslinking, we observe modulus peak broadening for all samples, starting at about 20 GPa (Figure 35). This is likely caused by additional post-crosslinking with the resulting film moduli approaching the upper bound of data reliability for the scanning probing analysis. The FDS mapping has a limited range of reliability that peaks around 50 GPa, and the tip used to interrogate the surface has a reliability range of approximately 1 MPa to 40 GPa.139 Despite these limitations, the near order of magnitude increase in moduli after crosslinking clearly demonstrates the mechanically enhancing effect of di-tyrosine crosslinks, which stabilize β-sheet formation, resulting in significant increase in the apparent elastic modulus, well above the common values for the initial protein films.146

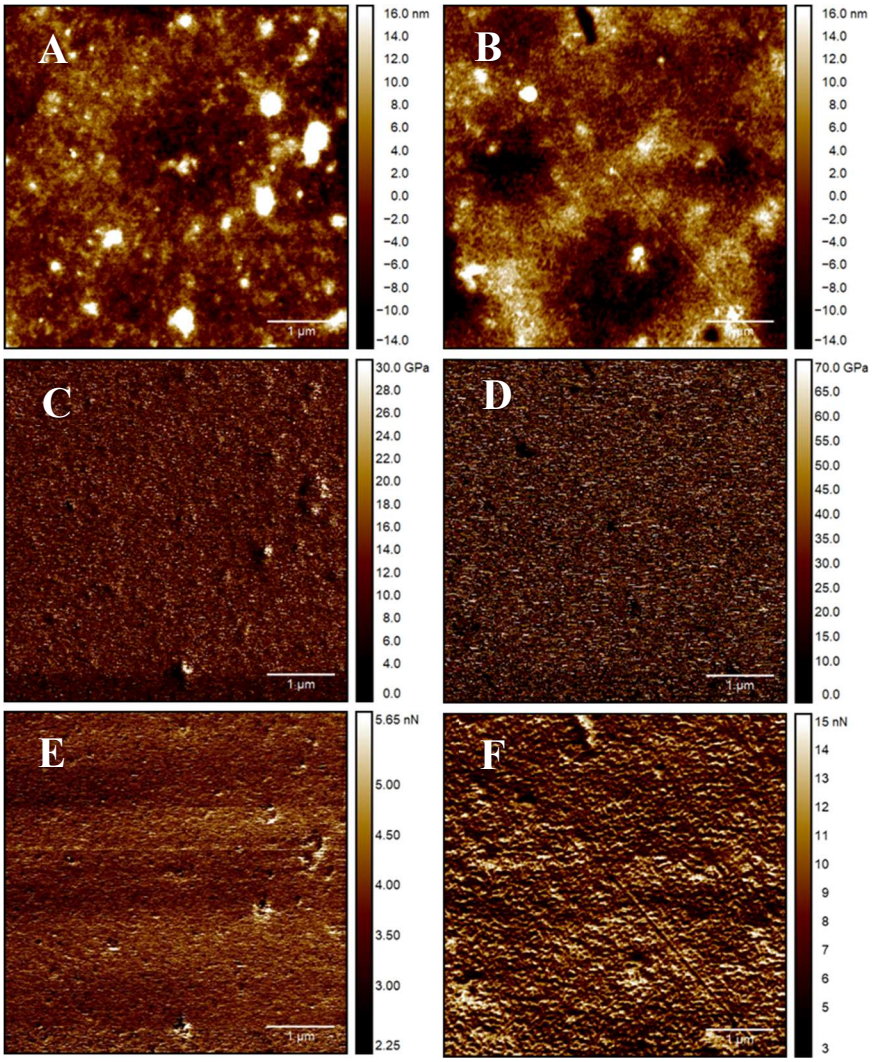

Figure 35. QNM images of suckeirn-12 dry before (A, C, E) and after (B, D, F) crosslinking where height (A,B), modulus (C, D), and adhesion (E, F) maps are shown.

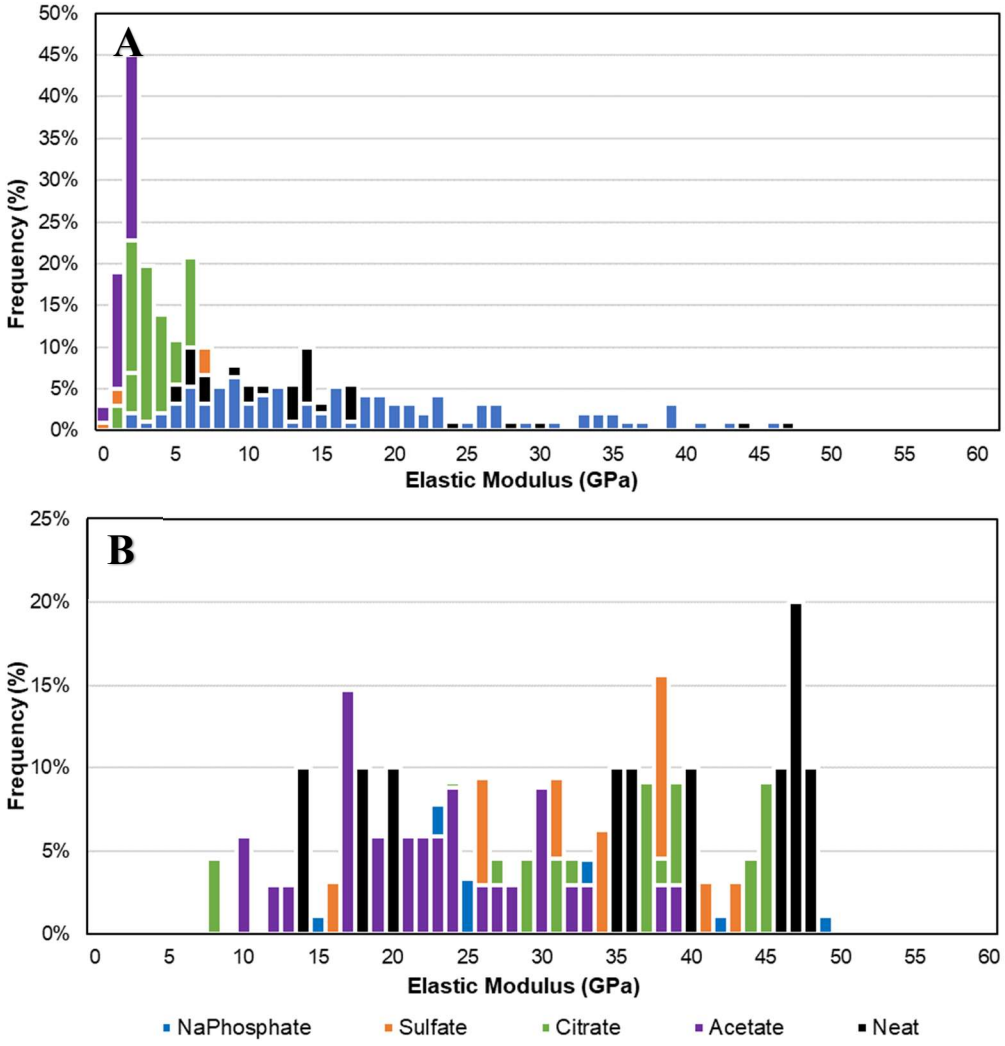

Figure 36. Histograms of FDS measured moduli for suckerin-12 films before (A) and after (B) crosslinking.

1.19 Conclusions

This work demonstrates several ways that suckerin-12 uses its local chemical environment and water to control intermolecular interactions and form aqueously stable biomaterials. Though, not a fiber forming protein, suckerin-12 is shown to can undergo shear induced crystallization and thermal vapor annealing to form a fibrous network microstructure that forms as random coils release into ordered β-sheet and helical architectures. Either is a readily implementable in materials

design to induce suckerin-12 to assemble by enabling suckerin-12 elongation from random coils into hydrogen bonded ordered structures. This work suggests that cephalopods undertake a similar protein elongating step while forming the semi-crystalline sucker ring teeth in a marine environment; after which subsequent assembly via salts is more favorable.

Then, suckerin-12 film stability is mediated by β-sheet formation provided in aqueous saline environments. Specifically, this is the case for saline environments where the solution pH is below the suckerin-12 isoelectric point as in the case of kosmotropic Hofmeister salts, where effectiveness maximized with strong conjugate bases. Changes in ionic environment not only facilitate changes in mechanical performance and dimension but correspond to shifts in secondary structure that serve as a higher-level order-induced means of mechanical tuning. Thus, the present study confirms and clarifies previously speculated mechanisms of suckerin-12 film reinforcement and presents methods of tuning its assembly in nature. In salt annealing, suckerin-12 takes advantage of both anions its environment and water to reorganize helices and random coils into β-sheets that lead to film constricting and increased elastic modulus. Salt treatment renders suckerin-12 aqueously stable films with comparable crystallinity and stability to that achieved using enzymatic crosslinking. In combining the order-induced mechanical enhancement of salt annealing and stabilization of crosslinking, we achieved a double crosslinking effect where suckerin-12 organized into more extended β-sheets. The study posits that suckerin-12 inter-protein physical crosslinks mediated via saline conditions render their aqueous stability and indicates how suckerin isoforms work together to create strong, well-bound suckerin assemblies. Our findings provide further input in understanding this relatively new protein and methods by which to tune its assembly, secondary structure, physical crosslinking, and mechanical performance in demanding biomaterials applications. In so doing, we have begun untangling the natural processes that cephalopods use to achieve strong, aqueously operable all-suckerin sucker ring teeth.

SYNTHETIC COPOLYMER INTERFACIAL ASSEMBLY

1.20 Overview

In this chapter, synthetic copolymers are used to better understand adsorption and assembly behavior found in the previous chapters. Two copolymers were chosen for this study. Copolymer type I contains GMA grafted to a backbone of OEGMA and demonstrates strong hydrophilic nature, while copolymer type 2 shows amphiphilic behavior due to LMA side chains interspersed with GMA son an OEGMA backbone. POEGMA exhibits thermosensitivity, protein repellency, and ability to compatibilize materials with water.[150,151,152,153,154,155,156] Lauryl methacrylate addition is used to tune the hydropathy of the copolymers.[157,158,159] This study focuses on the effect copolymer and substrate chemistry on copolymer when unbound and bound to GO flake surface adsorption. SiO_2, GO, and rGO surfaces were used. Hydrophobic interactions led to copolymer type 1 adsorbing solely at the edge of rGO flakes, while amphiphilic copolymer type 2 to adsorb onto all surfaces and exhibited network formation on GO, much like amphiphilic protein silk fibroin. Thus, this chapter shows the dominance of hydrophobicity in polymer adsorption and assembly to inorganic surfaces.

1.21 Experimental

Preparation of P(G66-O34), P(G15-O66-L19), and copolymer modified GO. The synthetic copolymers and modified GO were prepared as discussed in Chapter 3. The copolymers were diluted to 0.1 v/v % copolymer solution in methanol, and modified GO suspension dispersed in water only and methanol and water solutions for the following experiments.

Sample preparation. Copolymer samples were spin cast at 3000 rpm onto GO and rGO on SiO2 wafers. GO and rGO were prepared as explained in Chapter 3. The copolymer modified GO was deposited in SiO2 wafers via dip coating and spin casting on SiO2 wafers; the first for preparation of thick films and the second for disperse monolayers of modified GO.

Surface morphology and chemistry characterization. AFM and QNM were used to characterize adsorption and surface morphology of the copolymers and copolymer modified GO on silica surfaces. FTIR and XPS were used to characterize their surface chemistry. Parameters for each characterization technique are as discussed in Chapter 3.

1.22 Results and discussion

1.22.1 Adsorption of copolymer modified GO

First, copolymer grafting was verified using XPS, AFM and FTIR. Dip coated samples of the copolymer grafted flakes were used for XPS analysis. Figure 8 shows representative XPS scans for GO and GO-type 2. GO type-1 was like that of type 2. The scans show 280 – 300 eV on the XPS scan which corresponds to carbon. This elemental peak can be deconvoluted into the following subpeaks: sp2 and sp3 carbon at 284 eV, sp2 carbon-oxygen bonds at 286 eV, and sp1 carbon oxygen bonds at 290 eV. For pristine GO, C-C and C-O bonds would be at relative parity as shown here due to the single and double bonded carbon lattice of graphene and nearly 46 % oxygen loading of GO.22 Copolymer type 1 grafted GO on the other hand would have a higher loading of sp2 and sp1 carbon-oxygen bonds from GMA and POEGMA which causes the peak at 286 eV to exceed the magnitude of the peak at 284 eV. For GO modified with copolymer type-1 the disparity in peaks is more exaggerated because the copolymer type-1 only has GMA and POEGMA side chains, rather than the alkane LMA on type-2.

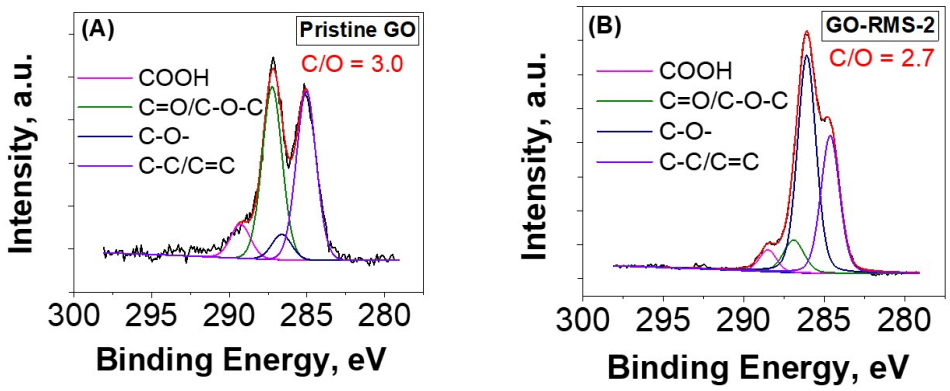

Figure 37. High resolution C1s XPS scans: (A) pristine GO and (B) GO/RMS-2.

AFM images of the modified flakes show increased roughness relative to typical GO flakes. A monolayer of GO flakes grafted with copolymer type 1 and type 2 at 0.04 wt. % was spun cast at 3000 rpm for 30 s onto a SiO2 surface. shows AFM micrographs of both types of polymer grafted flakes on SiO2 surface of a silicon wafer. GO flake lateral dimensions were approximately 3 – 10 µm with ~3 nm thickness. Given that flakes tend to be 0.9 nm thick, there is about 2 nm of copolymer tethered to the GO flakes.22 The flake surface exhibits uniform height and phase which suggests full, single layer copolymer coverage of the flakes.

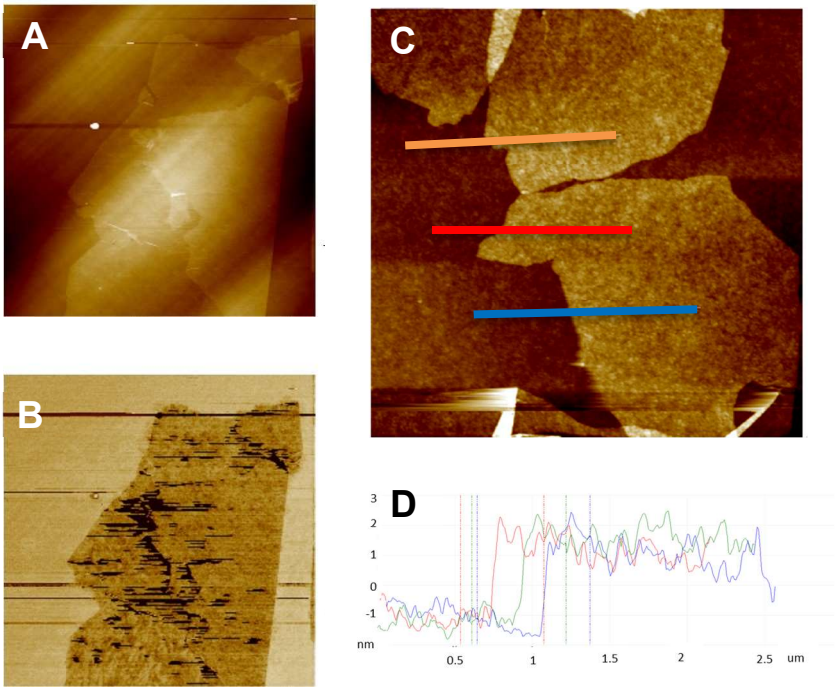

Figure 38: AFM topographical (A) and phase (B) images of graphene flakes modified with copolymer type 2 in water as Well as height profiles (D) taken from an AFM topographical image of graphene flakes modified with copolymer type 1 (C) with profile slices color coordinated.

FTIR shows that GO has a C-C and C=C bonded, conjugated lattice with epoxy, hydroxyl, and carboxylic side groups extended from the lattice plane. After normalizing the FTIR spectra, each spectrum has similar peaks characteristic of GO at 3400, 2800, 1700, and 1600 cm-1, which correlate with -OH, C-C, C=O, and C=C, respectively (Figure 38). Copolymers were grafted to GO flakes using hydroxyl groups on the flake surface, so there is a decrease in the peak at 3400 cm-1. The copolymer link to the GO surface through an acrylate bond which leads to the peak at 1700 cm-1 being significantly greater than that at 1600 cm-1, instead of the equal weighting of these peaks as shown for unmodified GO. There is also see a pronounced alkane peak at 2800 cm-1 for the copolymer grafted flakes due to the copolymer backbone and side chains with type 2 having the highest abundance of alkanes thanks to the presence of LMA, a long alkane side chain.

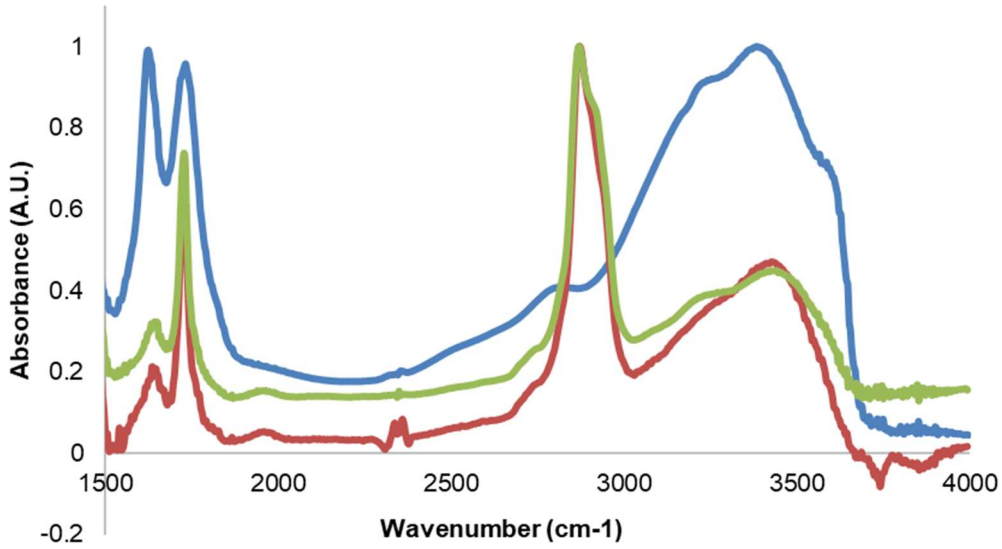

Figure 39: ATR-FTIR spectra of GO, GO modified with copolymer type 1 and type 2.

After verifying the copolymer grafting, experiments were conducted to probe copolymer assembly in terms of phase separation and copolymer extension primarily using SPM techniques AFM and

QNM. This was studied as a function of casting method, pH, flake substrate, and temperature. Sets of samples were deposited by spin casting and dip coating on SiO2 surface of a silicon wafer. GO type-1 and GO type-2 were deposited from aqueous (Figure 37) and methanol suspensions (Figure 39) then AFM was conducted in air and deionized water to probe dry and solution state behavior. And, spin coating was used create single, diffuse layers of modified flakes, whereas dip coating produced full coverage monolayer and multilayer films.

Figure 39 shows that spin casting GO type-1 and type-2 from methanol suspensions produces a distinct morphological change. For both copolymer grafted graphene flakes, AFM height and phase images obtained in air show spindles extending on the SiO2 surface from the flake surface. The spindles form an approximately 100 nm corona around each flake with each spindle having a thickness of about 1.2 nm. Three 10 μm by 10 μm images were acquired for each condition and exhibit this phenomenon on most flakes. When scanned in deionized water in QNM, which was used to enable better cantilever tracking in the It state, there is no difference in copolymer lateral extension. However, copolymer vertical extension does differ between the water and methanol modified GO suspensions. GO type 1 exhibited thicknesses of 10 and 12 nm when spun from water and methanol, respectively. Even more enhanced extension is seen from copolymer on GO type 2 which saw an over 2-fold increase in extension from 6 nm when spun from water and 15 nm when spun from methanol. These results suggest that the copolymer elongation could be caused by a combination of shear force applied during spin casting and rapid quenching due to fast eluting methanol. Additionally, hydrogen bonding moieties on the copolymer may preferentially interact with the methanol solvent rather than water which would lead to more elongated polymer when these flakes are spun cast. More work is needed to loosely identify this mechanism of elongation.

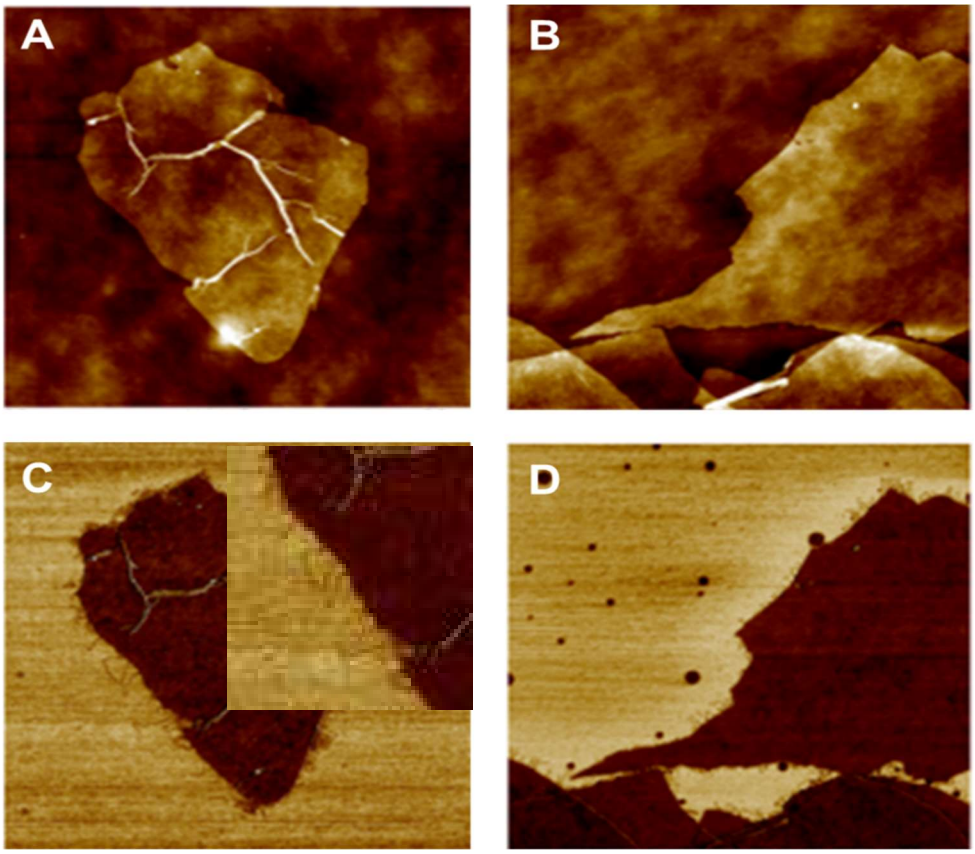

Figure 40: Topographical (A,B) and phase (C,D) images from in air AFM graphene flakes modified with copolymer type 1 (A,C) and type 2 (B,D), including an inset of C showing copolymer extension (E). Height profiles taken at the flake image are provided to indicate flake thickness post grafting.

1.22.2 Adsorption of untethered synthetic copolymers type 1 and 2

Similar experiments were undertaken with the untether copolymer to better understand what drives the assemblies in the previous section by characterizing their adsorption to surfaces of different philicity and degrees of heterogeneity. The copolymers in methanol were spin cast onto diffuse GO and rGO flakes on SiO2. On GO, copolymer type 1, which consists of POEGMA and is mostly hydrophilic, adsorbed to both GO and SiO2. Figure 40 shows dewetting pattern is observable SiO2 while relatively smooth and continuous coating forms on GO. Copolymer type 2 that consists of POEGMA with LMA sidechains that confer amphiphilicity and seems to adsorb preferentially on GO. Type 2 also develops higher order assembly on GO as indicated by the web-like white features in Figure 40. The surface used here can be categorized as homogenous, hydrophilic – SiO2,

heterogenous, hydrophilic – GO, and heterogenous, hydrophobic – GO. Thus, the selective adsorption of copolymer type 2 seems to selectively adsorb to GO because of its heterogeneity and local amphiphilicity. While, GO is generally hydrophilic thanks to a high density of oxygenated groups on its surface. However, the surface has defects and only 46% maximum loading of epoxides, hydroxyls, and the like; so, it is locally amphiphilic. This part of what enables silk fibroin, which is also amphiphilic, to adsorb and exhibit fibrillar assembly on GO.22 The amphiphilic type 2 copolymer seems to exhibit a similar phenomenon driven by the hydrophobic effect. Copolymer 2 assembles on GO to bring together like segments of the copolymer chain and GO surface. In contrast, copolymer type 1 does not exhibit assembly and wets both GO and SiO2, but it forms a thicker layer on SiO2. This result suggests that where there are two surfaces of comparably preferable hydrophilicity, the homogenous surface is preferred. The dewetting pattern observed seems to be a result of the low concentration rather than a lack of affinity because it is not observable at higher concentrations.

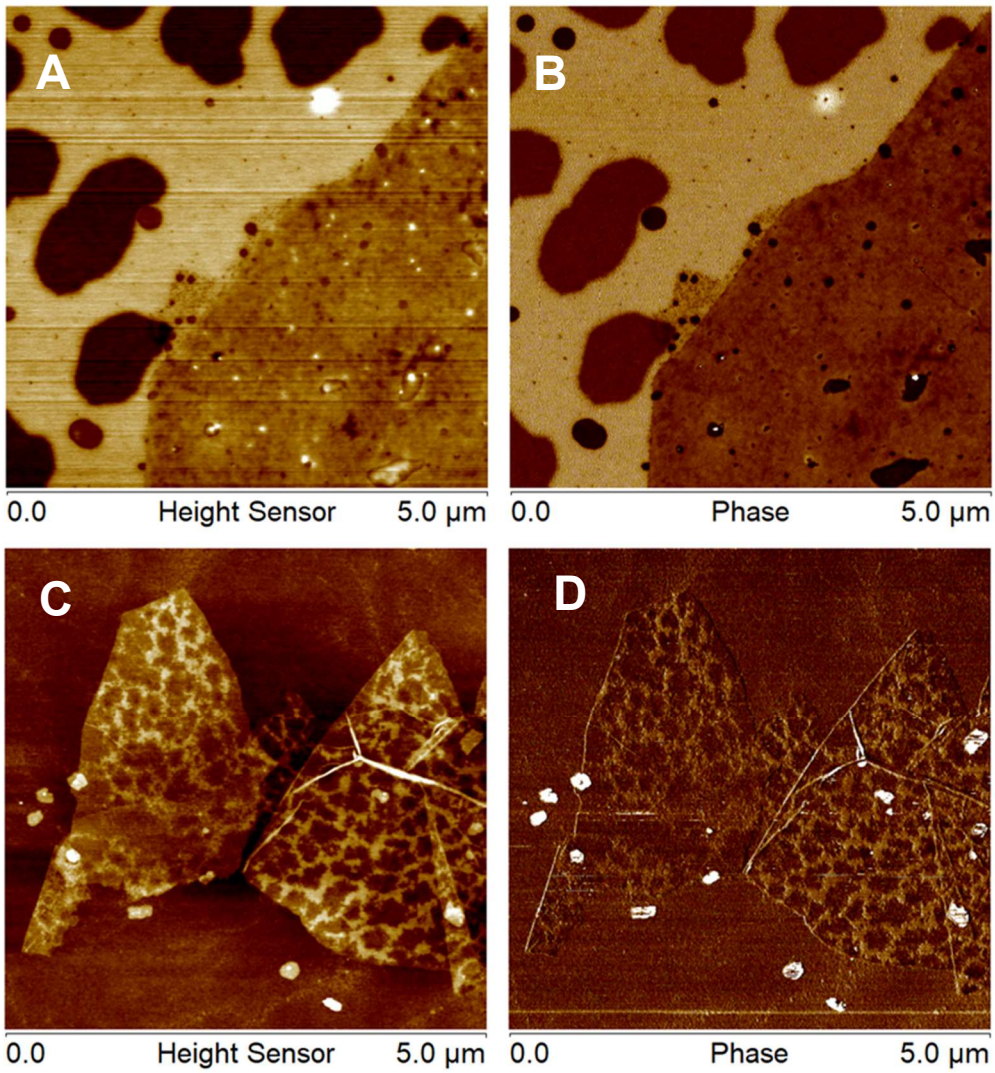

Figure 41. AFM height (A, C)and phase (B, D) images of copolymer type 1 (A, B) and type 2 (C, D) on GO flakes on SiO2 wafers. Z range: 9 (A, C). Angle range: 25O (B) and 17O(E).

Then, the copolymers were observed on rGO on SiO2 wafers. AFM height and phase images of copolymer type 1 exhibits the greatest contrast to the previous results (Figure 40). Copolymer type 1 seems to have adsorbed solely to SiO2 and the edge of each rGO flake. Adsorption of copolymer type 2 was observed at four different locations at 90 um2 before capturing the images shown in Figure 40, and the same phenomenon was observed. Aggregation and decreased adsorption were anticipated, but not near complete avoidance of the hydrophobic rGO flake surface, particularly, after spin casting. Meanwhile, copolymer type 2 adsorbs to both SiO2 and rGO. Adsorption on rGO appears slightly greater than on GO flakes, and copolymer type 2 exhibits less of the web-like

assembly observed on GO. This occurrence is likely due to the largely hydrophobic nature of rGO. The assemblies seem to form only at the flake edge. Previously, GO flake reduction was monitored using electrostatic force microscopy to track removal of oxygen moieties.9 In that study, the flake edge was the last to reduce completely as reduction appeared to propagate out from the flake surface interior. Thus, in the present study, the network formation on likely still partially oxidized flake edge due to the hydrophobic effect and forms a film on the remainder of the surface because of its high density of hydrophobic LMA sidechains.

1.23 Conclusions

The experiments and results outlined in this section provide a closer look at the role of surface and polymer surface chemistry, specifically their hydrophobicity and heterogeneity on adsorption and assembly using synthetic copolymers. Copolymer adsorption was observed unbound and when bound to GO. The bound GO exhibited sensitivity to solvent selection where dip coating or spin casting from methanol, a volatile solvent, enabled the copolymer to extend into corona around the GO flakes. No such extension or corona was observed when using copolymer modified GO in water suspensions. Taking this result into consideration, the adsorption of the unbound copolymer in methanol was characterized on GO and rGO coated SiO2 wafers. The results indicate that surface homogeneity and philicity have a significant impact on copolymer adsorption and assembly. When hydrophilicity of the copolymer and surface were matched, the more homogenous surface was preferred. For the amphiphilic copolymer type 2, heterogeneity was preferred over homogenous, hydrophilic in favor of heterogenous, hydrophobic rGO surface where philicity was better matched. Higher order assemblies occurred chiefly on amphiphilic surfaces, suggesting the hydrophobic effect is the impetus. Subsequent experiments are needed to further parse out the roles of homogeneity and philicity in adsorption and assembly and how they are disrupted by processing conditions. However, this study succeeds in experimentally detailing the role polymer and surface

structure play in interfacial assembly observed, not only with copolymers, but also suckerin, silk, and other amphiphilic biopolymers that may exhibit network and fiber assembly.

GENERAL DISCUSSIONS AND BROADER IMPACTS

1.24 General conclusions and future prospects

The goal of this dissertation was to elucidate interfacial interaction and assembly processes that drive interfacial assembly in order to mediate mechanical performance enhancement in biotic-abiotic composites. This is a complex task, so several studies were undertaken to achieve it. First, a well-studied, semi-crystalline biopolymer silk is used to identify non-covalent methods for manipulating interfacial interaction. In doing so, this work showed that by increasing positive interfacial interactions one can induce high order assemblies that provide improve stress transfer and improve mechanical performance of bionanocomposites. Then, lesser known protein suckerin was used to test cross applicability of findings from the silk studies to other semi-crystalline biopolymers. Not only is cross-applicability demonstrated, but some triggers for interfacial assembly were proven to operate constructively when applied together. Finally, synthetic copolymers were used to further investigate the specific role of biopolymer and inorganic surface properties (i.e. hydrophobicity and heterogeneity) on adsorption and assembly. The findings presented show that both like philicity and decreased roughness promote polymer adsorption and assembly. Below, these insights are discussed here in more depth.

1.24.1 Insights on assembly from silk fibroin on inorganic substrates and GO nanomembranes

The silk fibroin study sought to identify interfacial interactions and assembly processes that occur between silk and amphiphilic, heterogeneous GO flake surfaces as a function of during and post-processing conditions. Silk fibroin adsorption at the heterogeneous hydrophobic–hydrophilic surface of GO with different degrees of oxidation is addressed experimentally and theoretically. Samples were prepared using various spin-assisted deposition conditions relevant to assembly of laminated nanocomposites from graphene-based components and compared with SiO2 as a

benchmark substrate. Secondary structure of silk backbones changes as a function of silk fibroin concentration, substrate chemical composition, and deposition dynamics are assessed and compared with molecular dynamic simulations. It is observed that protofibrils form at low concentrations while variance in the deposition speed has little effect on silk secondary structure and morphology. However, balance of non-bonded interactions between electrostatic and van der Waals contributions can lead to silk secondary structure retention on the GO surface as opposed to aggregation and loss of crystalline assemblies on the hydrophobic rGO surface. Molecular dynamics simulations of silk fibroin at different surfaces show that strong van der Waals interactions play a pivotal role in losing and disrupting secondary structure on graphene and SiO2 surfaces.

Fine tuning silk fibroin structure on heterogeneous graphene-based surfaces paved the way toward development of biomolecular reinforcement for biopolymer–graphene laminated nanocomposites. Ultrathin and robust nanocomposite membranes were fabricated by incorporating GO sheets into a silk fibroin matrix by a dSA-LbL. In contrast to traditional SA-LbL, fast solution removal during deposition of solution on continuously spinning substrates resulted in largely unfolded biomacromolecules with enhanced surface interactions and suppressed nanofibril formation. The resulting laminated nanocomposites possessed outstanding mechanical properties, significantly exceeding those previously reported for conventional LbL films with similar composition. The tensile modulus reached extremely high values of 170 GPa, which had never been reported at the time for GO-based nanocomposites, the ultimate strength was close to 300 MPa, and the toughness was above 3.4 MJ m–3. The failure modes observed for these membranes suggested that increased silk assembly at the silk-GO flake composite interphase facilitated the observed performance enhancement. This interphase reinforcement led to effective load transfer between GO flakes in reinforced laminated nanocomposite materials with excellent mechanical strength that surpassed

those known for conventional flexible laminated carbon nanocomposites from GO and biopolymer components.

1.24.2 Insights on mechanisms of assembly and toughening of suckerin films

Over the course of this study, the cross-applicability of triggers for assembly in silk were tested on suckerin-12 in addition to salt annealing and enzymatic crosslinking, and then demonstrated their potential additive effects when applied in simultaneously. Assembly methods used include shear induced crystallization, thermal vapor annealing, salt annealing and enzymatic crosslinking. Thin films of suckerin-12 were used in order to closely monitor resultant changes in the microstructure concurrent with the protein secondary structure. First, the results showed suckerin-12 to exhibit susceptibility to shear induced crystallization and thermal vapor annealing just as fellow semi-crystalline biopolymer silk fibroin. Both methods resulted increased crystallinity of suckerin-12 as observed from FTIR with thermal vapor annealing causing a more pronounced secondary structure shift (10% increase in β-sheets). The clear shift in secondary structure caused by thermal vapor annealing was accompanied by the formation of a fibrous network on suckerin-12 surfaces, and ultimately yielded increased Young's modulus in both drop and spin cast suckerin-12 films (Figures 25 and 27). The fibrous structures that develop upon shearing or vapor annealing suckerin-12 are reminiscent of the nanotubular structures within the bulk sucker ring teeth matrix.47 Temperature mediation and abundance of water inherent in thermal vapor annealing produced assembly and crystallization with greater efficacy than shear induced crystallization. Both salt annealing and enzymatic crosslinking enhanced suckerin-12 crystallinity, exhibiting conversion of random coils to β-sheets crystallites that provide interfacial mechanical reinforcement (Figure 29).

And ultimately, salt annealing and enzymatic crosslinking were applied in concert to determine whether their effects on assembly and mechanical performance were additive. Our findings are in good agreement with a previous study on similar materials which was focused on the effect of

Hofmeister anions on suckerin-12 hydrogel swelling behavior and mechanics.47 This study not only demonstrates microstructure changes such as secondary structure composition and surface morphology but shows that the treatments can operate constructively. Enzymatic crosslinking seems to stabilize the ordered structure and enable formation of longer β-sheets as indicated by the substantial increase in β-sheet content at the expense of β-turns. This results in an increase in extended β-crystallites after crosslinking, and then salt treatment leads to an increase in suckerin-12 elastic modulus as measured via FDS nanomechanical probing. Overall, these results demonstrate the cross-applicability of the mechanisms found in Chapters 4 and 5 to other proteins and their mechanical performance, while suggesting that processing can have additive effects on performance, structure and assembly.

1.24.3 Insights on the hydrophobic effect and surface adsorption from synthetic copolymers

The brief study on copolymer adsorption and assembly then shows the dominance of the hydrophobic effect in polymer adsorption and assembly to inorganic surfaces. Hydrophilic copolymer type 1 (POEGMA) and amphiphilic copolymer type 2 (POEGMA-LMA) were spin coated onto GO flakes and rGO on SiO2 surface then characterized via AFM. Copolymer type 1 exhibited a clear preference for like surfaces GO and SiO2, and only adsorbed to the rGO flake edge, which tends to be less reduced. This is striking given that all sample were spin cast, a method that usually results in at least shear deposition. Copolymer type 2 adsorbed to each surface, but it formed high order assemblies on GO and rGO surfaces that were reminiscent of silk fibroin on GO without any additional processing. Similar effects were observed when the copolymers were tethered to GO and copolymer type 2, exhibited greater extension onto the homogenously hydrophilic SiO2 surface. These results provide subtext for the phenomena observed with suckerin and silk, suggesting that assembly of biopolymers is result of chiefly due to the hydrophobic effect which may be disrupted by processing steps.

1.25 Prospectus

This dissertation explored and the interfacial mechanisms that drive biopolymer-inorganic composite performance. The key insight from the work presented is the dominance of the hydrophobic effect and one's capacity to shield or promote hydrogen bonding drive interfacial assembly that enables bulk composite or polymer reinforcement. This work shows the importance of using fundamental materials knowledge to drive design and suggests avenues for future studies to better understand how to apply processing steps that work constructively with dominant hydrophobic interactions to tune the interfacial interactions and materials performance. Additionally, extrapolation of the nanoscale characterizations to macroscale and bulk media would improve industrial applicability of these findings. While leading with fundamentals takes patience and carefulness, the rewards for subsequent materials research and design are worth it.

1.26 Dissemination of work

This work has been distributed to the research community in the following publications and presentations.

1.26.1 Peer-reviewed Publications: Primary

[1] A. Grant, M. Krecker, M. Gupta, M. Crosby, V. Tsukruk. Enhancing marine protein stability via Hofmeister salt annealing and enzymatic crosslinking. *In preparation.*

[2] R. Xiong, A. Grant, R. Ma, S. Zhang, V. Tsukruk. Naturally-derived components for bionanocomposites. Materials Science and Engineering Reviews, 2018, 125, 1-41.

[3] M. Savchak, N. Borodinov, R. Burtovyy, M. Anayee, K. Hu, R. Ma, A. Grant, H. Li, D. Cutshall, Y. In, G. Koley, W. Harrell, G. Chumanov, V. Tsukruk, I. Luzinov. High conductive and transparent reduced GO nanoscale films via thermal conversion of polymer-encapsulated GO sheets. ACS Applied Materials and Interfaces, 2018, 10, 3975-3985.

[4] A. Grant, H. Kim, T. Dupnock, K. Hu, Y. Yingling, & V. V. Tsukruk. silk fibroin-Substrate Interactions at Heterogeneous Nanocomposite Interfaces (Cover story). Advanced Functional Materials, 2016, 26(35), 6496-6496.

[5] Y. Yin, K. Hu., A. Grant, Y. Zhang, and V. V. Tsukruk. Biopolymeric Nanocomposites with Enhanced Interphases. Langmuir, 2015, 31(39), 10859 – 10870.

1.26.2 Peer-reviewed publications: related works

[1] R. Xiong, K. Hu, A. Grant, R. Ma, W. Xu, C. Lu, X. Zhang, & V. V. Tsukruk. Ultrarobust Transparent Cellulose Nanocrystal-Graphene Membranes with High Electrical Conductivity. Advanced Materials, 2016, 28, 1501– 1509.

1.26.3 Presentations

[1] M. Krecker, A. Grant, M. Savchak, N. Borodinov, I. Luzinov & V. V. Tsukruk, Oral and Poster Presentations at the American Chemical Society Spring National Conference, New Orleans, LA, March 2018.

[2] A. Grant & V. Tsukruk. Protein Assembly at Bionanocomposite Interphases, Oral and Poster Presentations at the American Chemical Society Spring National Conference, New Orleans, LA, March 2018.

[3] A. Grant, M. Krecker, S. Tadepalli, M. Gupta, M. Crosby, P. Dennis, S. Singamaneni, R. Naik, V. Tsukruk. Aqueous Toughening in Crosslinked Marine Animal Proteins, Oral Presentation at the American Chemical Society Spring National Conference, New Orleands, LA, March 2018.

[4] H. S. Kim, B. Farmer, A. Grant, V. V. Tsukruk, & Y. Yingling. Role of graphene oxidation on physisorption of biomolecules using computational modeling, Oral Presentation at the American Chemical Society Fall National Conference, Washington, DC, August 2017.

[5] A. Grant, K. Hu, S. Young, Y. Yingling, & V. V. Tsukruk. Controlled Protein Folding for Robust Bionanocomposite Design, Oral Presentation at the 12th Annual National Graduate Research Polymer Conference, Akron, OH, June 2016.

[6] A. Grant, K. Hu, S. Young, Y. Yingling, & V. V. Tsukruk. silk fibroin Secondary Structure on Various GO Substrates, Oral Presentation at the American Chemical Society Spring National Conference, San Diego, CA, March 2016.

[7] A. Grant, Y. Yi, K. Hu, Y. Zhang, & V. V. Tsukruk. Tuning Protein Secondary Structure for Bionanocomposite Reinforcement, Poster Presentation at the American Chemical Society Spring National Conference, San Diego, CA, March 2016.

1.26.4 Awards and Recognition

[1] ACS Poly Excellence in Graduate Polymer Research, April 2018

[2] McKinsey APD Impact Diversity Awardee, March 2018

[3] The Dow Chemical Company BEST Symposium, August 2017

[4] Milliken Graduate Research Symposium Honoree (7/120 applicants), April 2017

[5] National Science Foundation Graduate Research Fellowship, August 2014

[6] Air Force Research Laboratory Scholarship, April 2016

APPENDICES

The appendix contains additional tables and figures not presented in the previousr chapters.

1.27 Chapter 4 supporting information

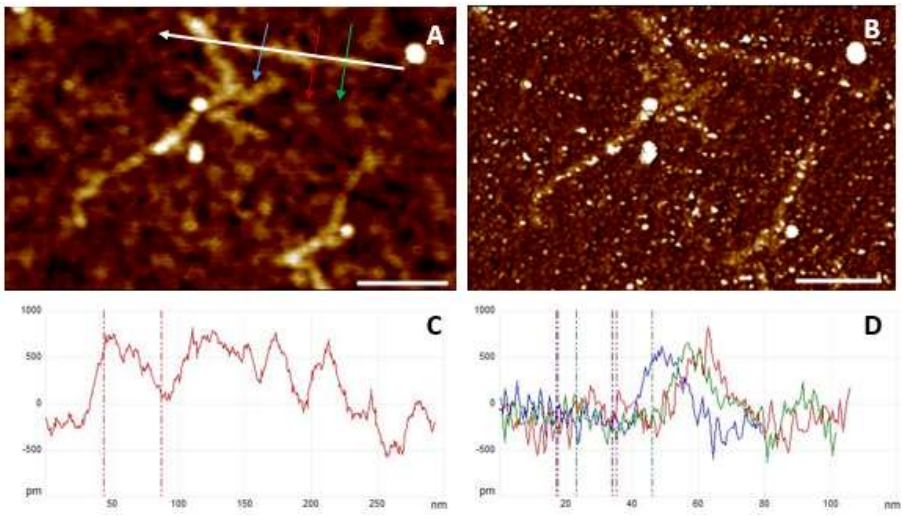

Figure 42. Silk fibroin at 0.002 wt. % dynamically cast on GO flakes at 5000 rpm morphology in AFM height (A) and phase (B) images with height profiles corresponding to the white (C), red, green, and blue lines (D) in A. Scale: 100 nm. Z range: 2 nm.

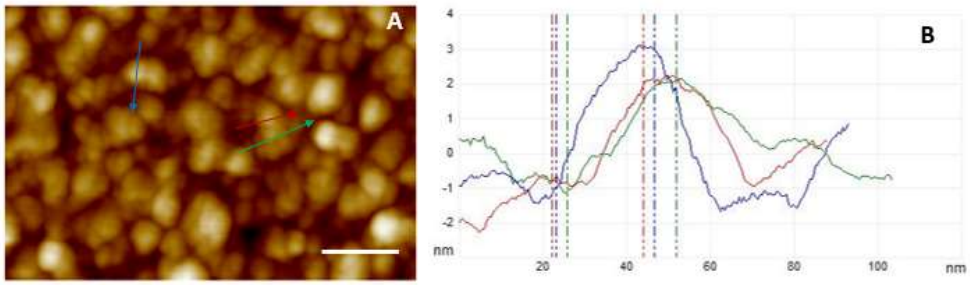

Figure 43. Silk fibroin at 0.002 wt. % deposited via conventional SA-LbL on GO flakes at 5000 rpm morphology in AFM height (A) with height profiles corresponding to the red, green, and blue lines (B) in A. Scale: 100 nm. Z range: 10 nm.

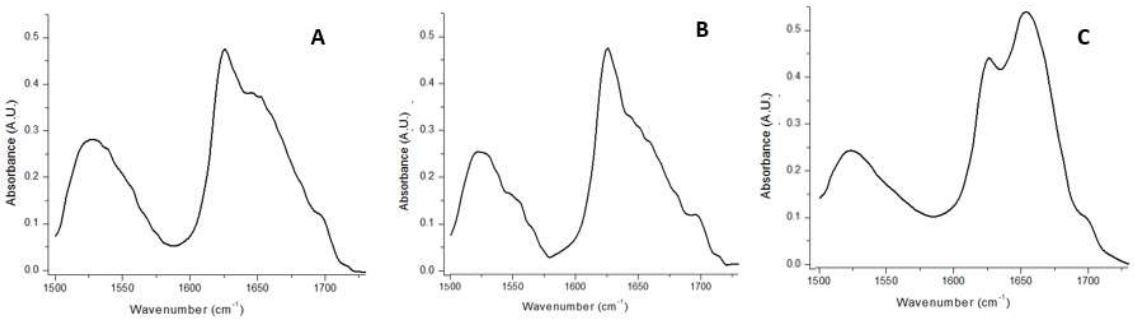

Figure 44. ATR-FTIR spectra of silk fibroin (A) on GO (B) and rGO (C) in the amide I and amide II regions.

GAGS(GAGAGS)$_4$GAGAGYGAGVGVGYGAGYGAGAGAGYGAGAGSGAAS
(GAGAGS)$_{10}$GAGVGSGAGAGSGAGAGVGYGAGAGVGYGAGAGSGAAS(G
AGAGS)$_9$GAGVGYGAGVGAGYGAGYGAGAGAGYGAGAGSGAASGAGAGS

GAGAGS: 65%
GAAS: 5%
GAGAGY: 16%
GAGVGAGY: 9%

Figure 45. Sequence of *Bombyx Mori* heavy chain with 258-amino acid segment used in MD. simulation

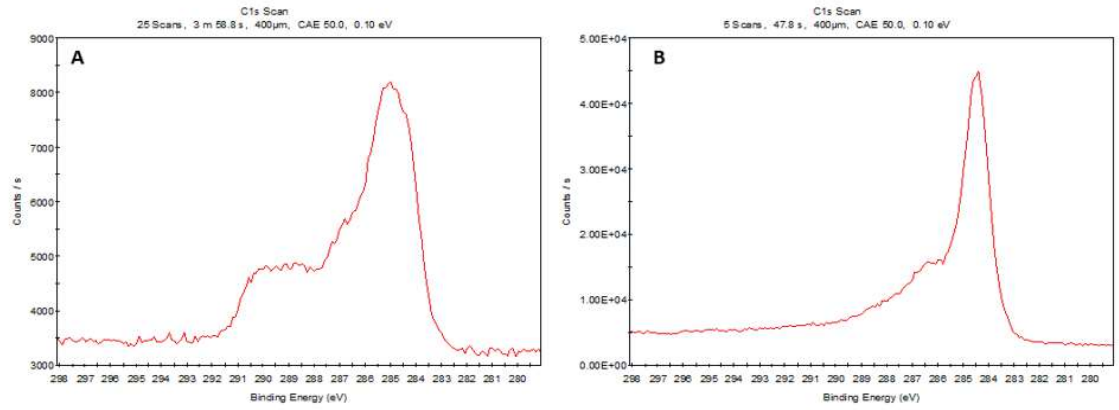

Figure 46. XPS of rGO carbon peak for hydrazine solution (A) and vapor reduction methods (B).

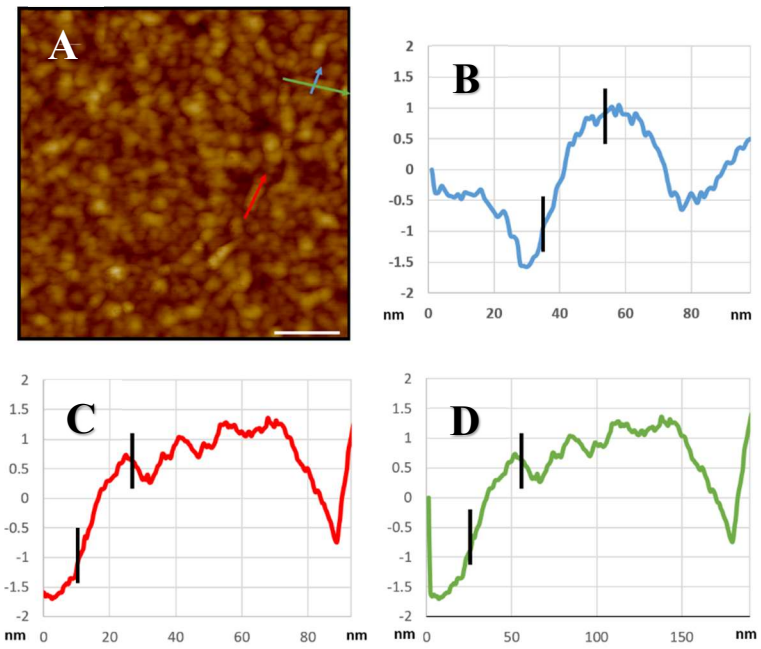

Figure 47. The AFM topographical image of Figure 1B is used as an additional example of cross-sections used for height measurement, where the height profiles correspond to the blue (B), red (C), and green (D) in A. Scale: 100 nm. Z range: 5 nm

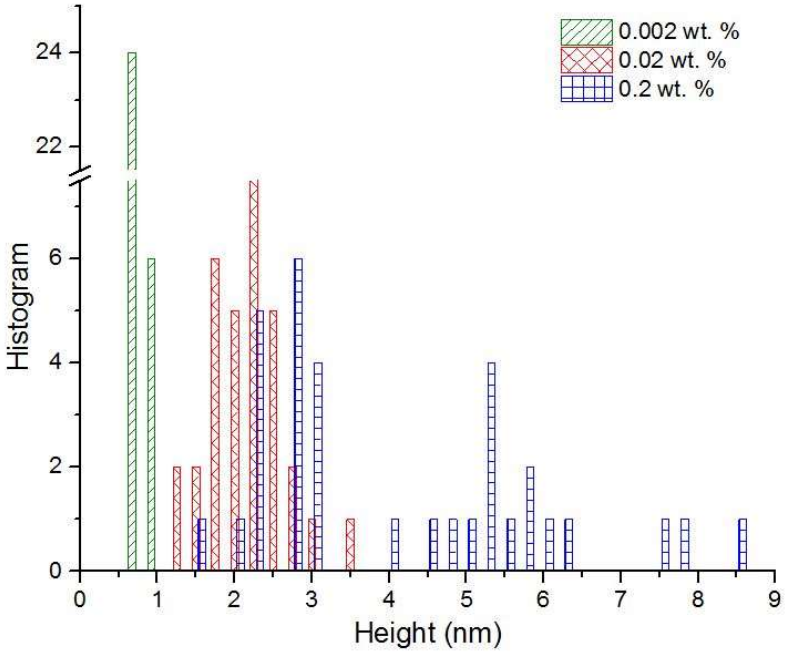

Figure 48. Histogram of silk fibroin structure height when cast by conventional SA-LbL at 5000 rpm. The data presented is directly taken from the images shown in Figure 7.

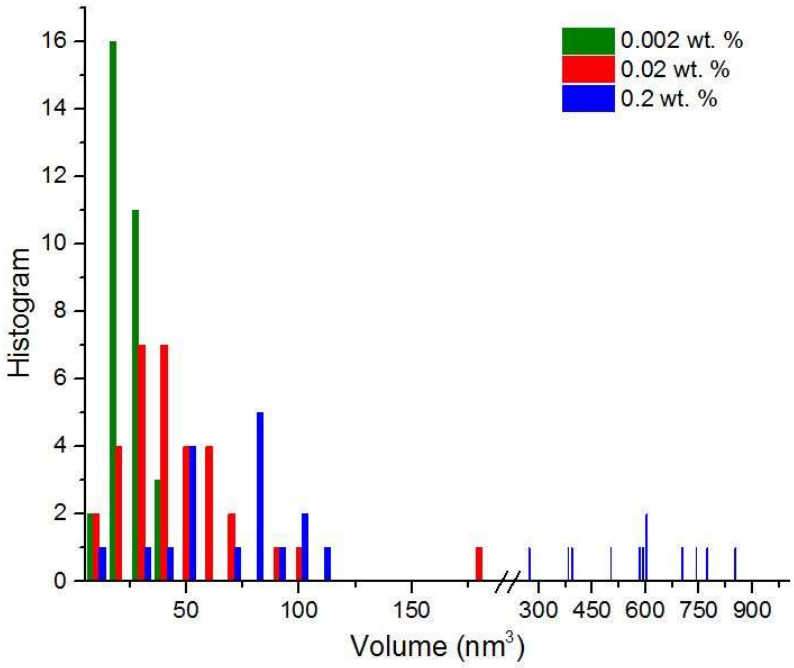

Figure 49. Histogram of silk fibroin structure volume when cast by conventional SA-LbL at 5000 rpm. The data presented is directly taken from the images shown in Figure 7.

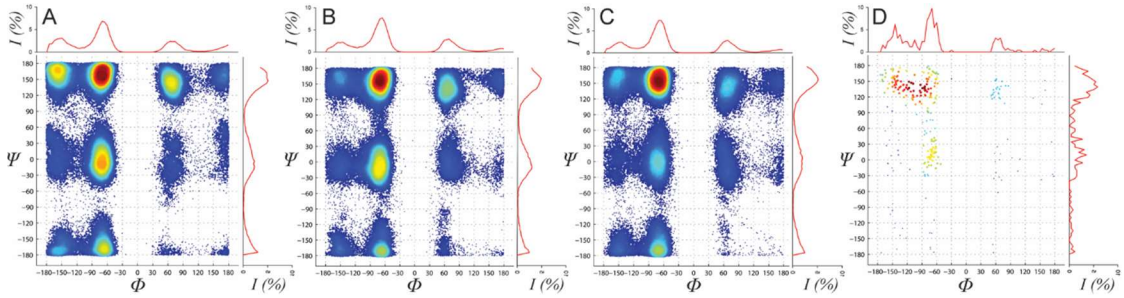

Figure 50. Ramachandran plot with the probability (*I*) of silk on (A) graphene, (B) GO, (C) SiO2, and (D) free standing where red indicates greater density.

1.28 Chapter 5 supporting information

GO content (vol.%)		Ultimate stress (MPa)	Ultimate strain (%)	Young's Modulus (GPa)	Toughness (MJ m^{-3})
23.7	A	273	1.85	170	3.97
	B	278.3	1.71	165	3.84
	C	326	0.96	176	2.46
	Average	292.4	1.51	170.5	3.42
	Std. Dev.	29.2	0.48	5.5	0.83
18.4	A	248.4	1.18	123.2	2.26
	B	253.3	1.03	120.8	1.94
	C	261.2	1.06	122.4	2.18
	Average	254.3	1.09	122.1	2.13
	Std. Dev.	6.5	0.08	1.2	0.17
11.1	A	168.7	0.36	83.2	0.36
	B	175.4	0.83	83.7	1.14
	C	159.8	0.66	60.9	0.67
	Average	168.0	0.62	75.9	0.72
	Std. Dev.	7.8	0.24	13.2	0.39
8.75	A	161	0.38	78.4	0.41
	B	140.1	0.55	50	0.5
	C	142.9	0.52	53.2	0.47
	Average	148	0.48	60.5	0.46
	Std. Dev.	11.3	0.09	15.6	0.05
5.1	A	138	0.47	57.5	0.41
	B	128.5	0.47	52.3	0.39
	C	136.4	0.45	51.2	0.38
	Average	134.3	0.46	53.7	0.39
	Std. Dev.	5.1	0.01	3.4	0.02
0	A	83	0.86	12.7	0.45
	B	61.9	0.78	11.2	0.32
	C	75.9	0.86	12.1	0.44
	Average	73.6	0.83	12.0	0.40
	Std. Dev.	10.7	0.05	0.75	0.07

Table 4. Summary of mechanical performance for GO at various concentrations in dSA-LbL silk-GO nanomembranes characterized via bulging test.

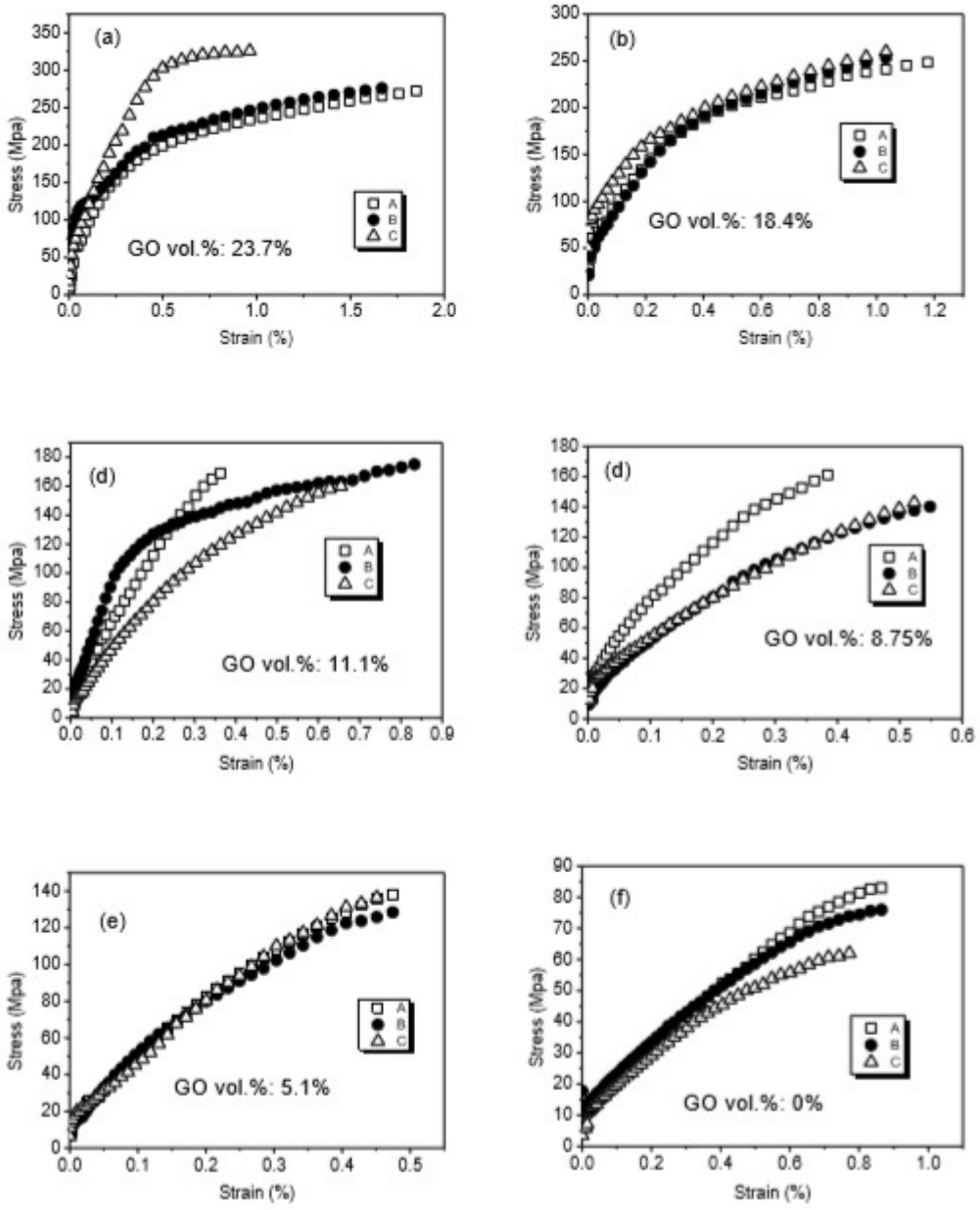

Figure 51. Representative stress–strain curves derived from the bulging tests for dSA GO-silk fibroin nanocomposite membranes with different GO content. (a) 23.7% (b) 18.4% (c) 11.1% (d) 8.75% (e) 5.1% (f) 0%. Each sample with three different test points used for comparison.

1.29 Chapter 6 supporting information

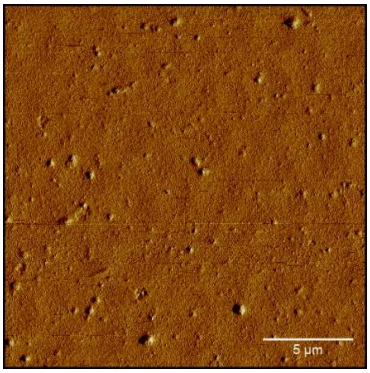

Figure 52. Phase image of suckerin-12 at 3 wt.% on a silica substrate.

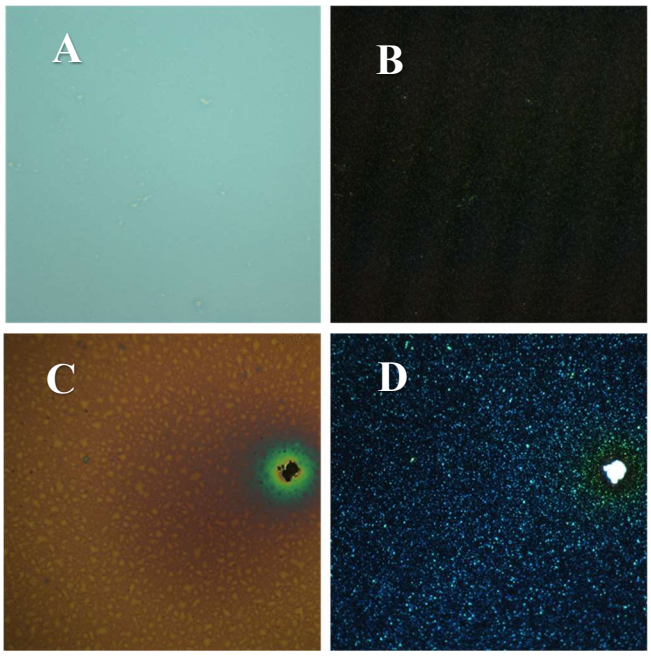

Figure 53. Optical microscopy images of the polystyrene pre-layer in bright (A) and dark field (B) and suckerin-12 on polystyrene under bright (C) and dark field (D).

.

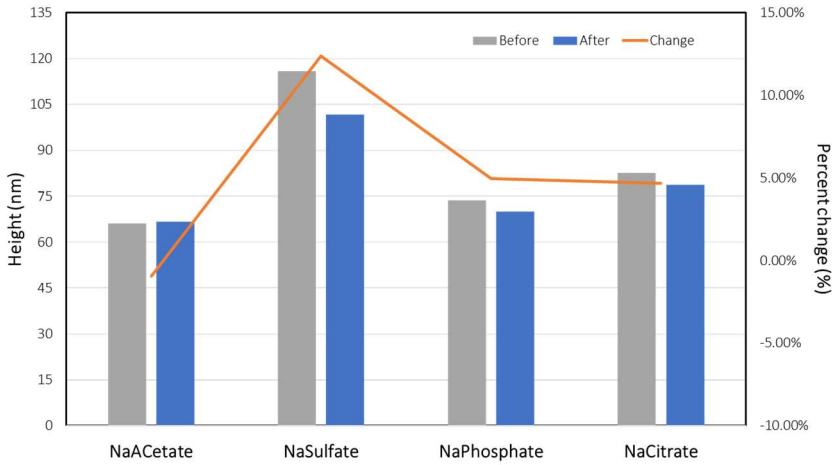

Figure 54. Bar graph of suckerin-12 film heights before and after salt annealing as well as the percent change.

Deposition	Concentration (wt. %)	Chemical/ Environmental Treatment	Non-chemical Treatment	RMS Roughness	St. Dev.
DC	1	N/A	N/A	0.40	0.08
SC	1	N/A	N/A	0.40	0.08
SC	3	N/A	N/A	1.8	0.1
SC	1	N/A	TVA	0.40	0.04
SC	3	N/A	SA - Phosphate	3.0	0.3
SC	3	N/A	SA - Acetate	3.1	0.3
SC	3	N/A	SA - Citrate	3.2	0.5
SC	3	N/A	SA - Sulfate	2.2	0.4
SC	3	Enzymatic crosslinking	SA - Phosphate	3.1	0.1
SC	3	Enzymatic crosslinking	SA - Acetate	3.5	0.6
SC	3	Enzymatic crosslinking	SA - Citrate	3.6	0.8
SC	3	in water	SA - Sulfate	3.2	0.7

Table 5. Summary of RMS roughness measurements discussed in the main text.

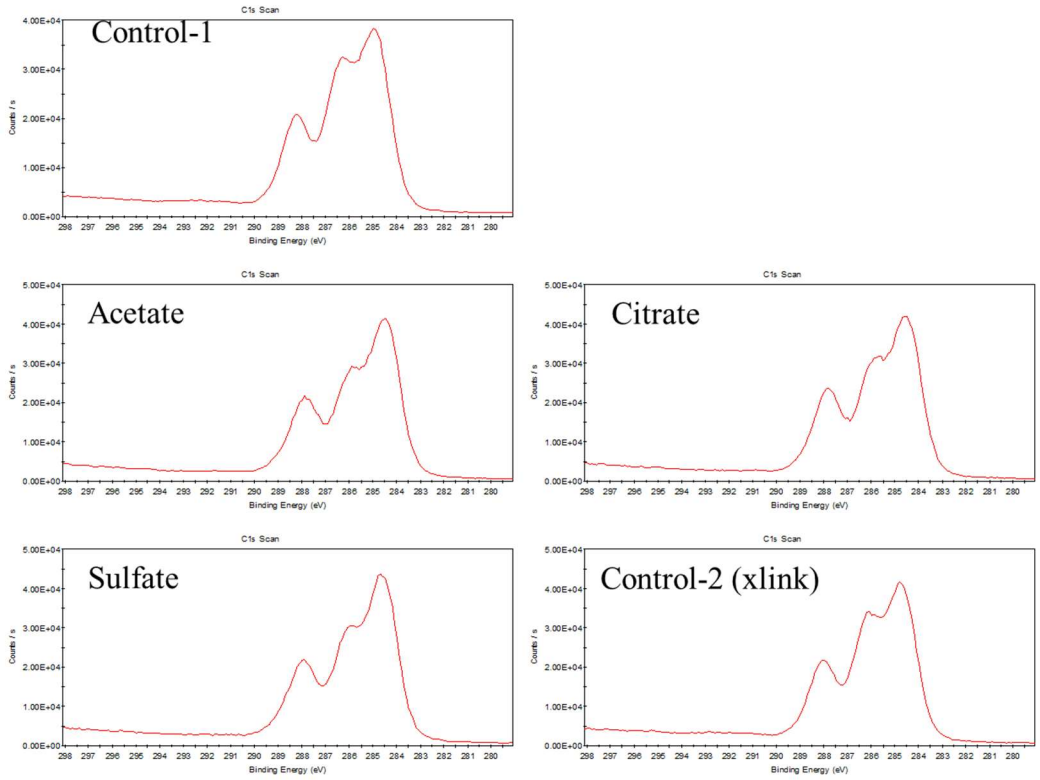

Figure 55. XPS carbon peak for neat, salt treated, and crosslinked suckerin-12.

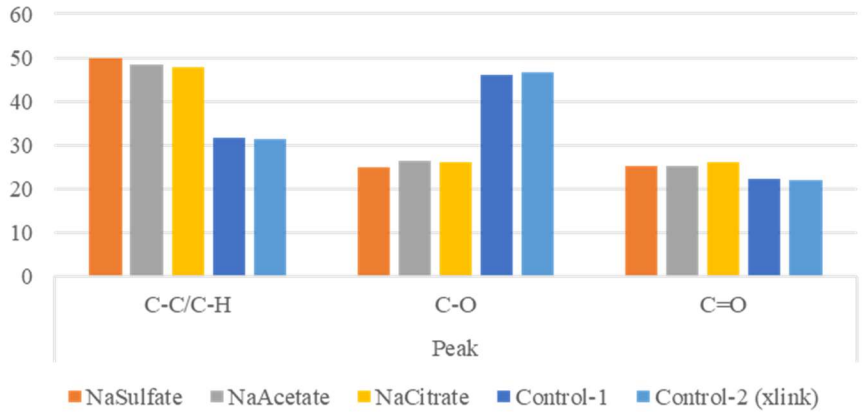

Figure 56. XPS carbon peak composition taken from deconvoluting for common hybridization peaks.

REFERENCES

1 H. D Wagner, Nat Nanotech 2007, 2, 742.

2 K. Hu, R. Xiong, H. Guo, R. Ma, S. Zhang, Z. Wang, V. Tsukruk, Adv Mater 2016, 28 (18), 3549.

3 C. Jiang, S. Markutsya, Y. Pikus, V. Tsukruk, Nat Mater 2004, 3, 721.

4 I. Lusinov, S. Minko, V. Tsukruk, Prog Poly Sci, 2004, 29, 635.

5 I. Tokarev, Tokareva, S. Minko, Adv Mater 2008, 20, 2730.

6 J. Kaur, R. Rajkhowa, T. Tsuzuki, K. Millington, J. Zhang, X. Wang, Biomacromolecules 2013, 14 (10), 3660.

7 P. H. G. Chao, S. Yodmuang, X. Wang, L. Sun, D. L. Kaplan, G. Vunjak-Novakovic, J. Biomed. Mater. Res., Part B 2010, 95B, 84.

8 C. Cheng, I. Teasdale, O. Brüggemann, Macromol. Biosci. 2014, 14, 807.37.

9 D. D. Kulkarni, I. Choi, S. S. Singamaneni, V. V. Tsukruk, ACS Nano 2010, 4, 4667.

10 R. Z. Wang, Z. Suo, A. G. Evans, N. Yao, I. A. Aksay, J. Mater. Res. 2001, 16 (09), 2485.

11 Vogel, S., Comparative biomechanics, Life's physical world. Princeton University Press, 2003.

12 F. G. Omenetto, D. L. Kaplan, Science 2010, 329, 528.

13 J. M. Gosline, P. A. Guerette, C. S. Ortlepp, K. N. Savage, J. Exp. Biol. 1999, 202, 3295.

14 O. Hakimi, D. P. Knight, F. Vollrath, P. Vadgama, Composites, Part B 2007, 38, 324.

15 S. Keten, Z. Xu, B. Ihle, M. Buehler, Nat Mater 2010, 9 (4), 359.

16 S. Inoue, K. Tanaka, F. Arisaka, S. Kimura, K. Ohtomo, S. Mizuno, J. Biol. Chem. 2000, 275, 40517.

17 S. Koebley, D. Thorpe, P. Pang, P. Chrisochoides, I. Greving, F. Vollrath, H. Schniepp, Biomacromolecules 2015, 16 (9), 2796.

18 H. Tao, D. Kaplan, F. Omenetto, Adv Mater 2012, 24 (21), 2824.

19 M. Ishida, T. Asakura, M. Yokoi, H. Saito, Macromolecules 1990, 23, 88.

20 H. J. Jin, J. Park, V. Karageorgiou, U. J. Kim, R. Valluzzi, P. Cebe, D. L. Kaplan, Adv Funct Mater. 2005, 15, 1241.

21 D. Wilson, R. Valluzzi, D. Kaplan, Biophysical J 2000, 78 (5), 2690.

22 A. Grant, H.S. Kim, T. Dupnock, K. Hu, Y. Yingling, V. Tsukruk, Adv Funct Mater 2016, 26 (35), 6496.

23 I. Drachuk, O. Shchepelina, M. Lisunova, S. Harbaugh, N. Kelley-Loughnane, M. Stone, V. V. Tsukruk, ACS Nano 2012, 6, 4266.

24 N. Guziewicz, A. Best, B. Perez-Ramirez, D. L. Kaplan, Biomaterials 2011, 32, 2642.

25 Z. Megeed, J. Cappello, H. Ghandehari, Adv. Drug Delivery Rev. 2002, 54, 1075.

26 C. Ye, O. Shchepelina, R. Calabrese, I. Drachuk, D. L. Kaplan, V. V. Tsukruk, Biomacromolecules 2011, 12, 4319.

27 S. Yodmuang, S. L. McNamara, A. B. Nover, B. B. Mandal, M. Agarwal, T. A. N. Kelly, P. H. G. Chao, C. Hung, D. L. Kaplan, G. Vunjak-Novakovic, Acta Biomater. 2015, 11, 27.

28 B. Kundu, R. Rajkhowa, S. C. Kundu, X. Wang, Adv. Drug Deliv. Rev. 2013, 65, 457.

29 J. R. Mauney, T. Nguyen, K. Gillen, C. Kirker-Head, J. M. Gimble, D. L. Kaplan, Biomaterials 2007, 28, 5280.

30 K. Hu, M. K. Gupta, D. D. Kulkarni, V. V. Tsukruk, Adv. Mater. 2013, 25, 2301.

31 L. Huang, C. Li, W. Yuan, G. Shi, Nanoscale 2013, 5, 3780.

32 Y. Yin, K. Hu, A. M. Grant, Y. Zhang, V. V. Tsukruk, Langmuir 2015, 31, 10859.

33 K. Hu, D. D. Kulkarni, I. Choi, V. V. Tsukruk, Prog. Polym. Sci. 2014, 39, 1934.

34 A. Neville, Biology of Fibrous Composites: Development Beyond the Cell Membrane. Cambridge University Press: New York, USA, 1993.

35 M. Rinaudo, Prog. Polym. Sci. 31 (2006) 603.

36 H. Pan, W. Wang, Y. Pan, L. Song, Y. Hu, K. M. Liew, Carbohydr. Polym. 2015, 115, 516.

37 A. Takegawa, M. Murakami, Y. Kaneko, J. Kadokawa, Carbohydr. Polym, 2010, 79 (1), 85.

38 N. L.Yusof, L. Y. Lim, E. Khor, Carbohydr. Res. 2004, 339 (16), 2701.

39 A.Miserez, J. C. Weaver, P. B. Pedersen, T. Schneberk, R. T. Hanlon, D. Kisailus, H. Birkedal, Adv. Mater. 2009, 21, 401.

40 A. Kumar, H. Mohanram, K. W. Kong, R. Goh, S. Hoon, J. Lescar, A. Miserez, Biomater. Sci. 2018, 6, 2440.

41 F. W. Zok, A. Miserez, Acta Materialia 2007, 55 (18), 6365.

42 Demirel, M. Cetinkaya, A. Pena-Francesch, J. Huihun, Macromol Biosci 2015, 15, 300.

43 D. Ding, P. A. Guerrette, S. Hoon, K. W. Kong, T. Cornvik, M. Nilsson, A. Kumar, J. Lescar, A. Miserez, Biomacromolecules. 2014, 15 (9), 3278.

44 P. Guerrette, S. Hoon, Y. Seow, M. Raida, A. Masic, F. Wong, V. Ho, K. Kong, M. Demirel, A. Pena-Francesch, S. Amini, G. Tay, D. Ding, A. Miserez, Nat Biotechnol 2013, 31 (10), 908.

45 P. Guerette, S. Hoon, D. Ding, S. Amini, A. Masic, V. Ravi, B. Venkatesh, W. Weaver, A. Miserez, ACS Nano. 2014, 8 (7), 7170.

46 Y. Mu, B. Q. Tang, M. Yu, Phys. Rev. E 2014, 89 (3), 032711-1.

47 C. C. Buck, P. B. Dennis, M. K. Gupta, M. T. Grant, M. G. Crosby, J. M. Slocik, P. A. Mirau, K. A. Becknell, K. K. Comfort, R. R. Naik, Macromolecular Biosci. 2018, 19 (3), 1800238.

48 F. E. Bailey Jr, J. V. Koleske, Poly(ethylene oxide). New York: Academic Press; 1976.

49 E. Tziampazis J. Kohn, P. V. Moghe, Biomaterials. 2000;21, 511.

50 S. R. Meyers, M. W. Grinstaff, 2012;113, 1615.

51 J. L. Cleland, S. E. Builder, J. R. Swartz, M. Winkler, J. Y. Chang, D. I. Wang, Polyethylene glycol enhanced protein refolding. Biotechnol (NY). 1992;10:1013–9.

52 P. Schaffner, J. Meyer, M. Dard, R. Wenz, B. Nies, S. Verrier, H. Kessler, M. Kantlehner, J Mater Sci Mater Med. 1999 Dec; 10(12):837-9.

53 S. J. Breusch, K. D. Kühn, Bone cements based on polymethylmethacrylate Orthopade. 2003 Jan; 32(1):41-50.

54 B. Wang, Q. Lin, C. Shen, J. Tang, Y. Han, H. Chen, J Colloid Interface Sci. 2014 Oct 1; 431,1-7.

55 R. Q. Frazer, R. T. Byron, P. B. Osborne, K. P. West, J Long Term Eff Med Implants. 2005; 15(6):629-39.

56 J. Hu, G. Wang, W. Zhao, X. Liu, L. Zhang, W. Gao, Biomaterials 2016, 96, 84.

57 N. M. B. Smeets, M. Patenaude, D. Kinio, F. M. Yavitt, E. Bakaic, F.-C. Yang, M. Rheinstädter, T. Hoare, Polym Chem 2014, 5, 6811

58 X. Shi, Y. Wang, D. Li, L. Yuan, F. Zhou, Y. Wang, B. Song, Z. Wu, H. Chen, J. L. Brash, Langmuir 2012, 48, 17011.

59 M. Liu, J. C. Leroux, M. A. Gauthier, Prog Polym Sci 2014, 48, 111.

60 A. Skandalis, S. Pispas, J Polym Sci, Part A 2017, 55, 155.

61 G. Wang, M. Chen, S. Guo, A. Hu, J Polym Sci Part A 2014, 52, 2684.

62 K. Knop, D. Pretzel, A. Urbanek, T. Rudolph, D. H. Scharf, A. Schallon, M. Wagner, S. Schubert, M. Kiehntopf, A. A. Brakhage, F. H. Schacher, U. S. Schubert, Biomacromolecules 2013, 14, 2536.

63 N. Borodinov, J. Giammarco, N. Patel, A. Agarwal, K. R. O'Donnell, C. J. Kucera, L. G. Jacobsohn, I. Luzinov, ACS Appl Mater Interfaces 2015, 7, 19455.

64 P. Lin, J. Giammarco, N. Borodinov, M. Savchak, V. Singh, L. Kimerling, D. Tan, K. Richardson, I. Luzinov, A. Agarwal, ACS Appl Mater Interfaces 2015, 7, 11189.

65 B. Zdyrko, I. Luzinov, Macromol Rapid Commun 2011, 32, 859.

66 N. Borodinov, A. P. Soliani, Y. Galabura, B. Zdyrko, C. Tysinger, S. Novak, Q. Du, Y. Huang, V. Singh, Z. Han, J. Hu, L. Kimerling, A. M. Agarwal, K. Richardson, I. Luzinov, ACS Nano 2016, 10, 10716.

67 E. Soto-Cantu, B. Lokitz, J. Hinestrosa, C. Deodhar, J. Messman, J. Ankner, S. Kilbey, Langmuir 2011, 27, 5986.

68 E. Soto-Cantu, B. Lokitz, J. Hinestrosa, C. Deodhar, J. Messman, J. Ankner, S. Kilbey, Langmuir 2011, 27, 5986.

69 M. Benaglia, A. Alberti, L. Giorgini, F. Magnoni, S. Tozzi, Polym Chem 2013, 4, 124.

70 K. Safa, M. Nasirtabrizi, Eur Polym J 2005, 41, 2310.

71 Y. Galabura, A. Soliani, J. Giammarco, B. Zdyrko, I. Luzinov, Soft Matter 2014, 10, 2573.

72 P. Scheibe, M. Barz, M. Hemmelmann, R. Zentel, Langmuir 2010, 26, 5661.

73 Y. Feng, C. Xiao, J Appl Polym.Sci 2006, 101, 1248.

74 D. Chatterjee, B. Mandal, Macromolecules 2006, 39, 9192.

75 D. Konios, M. M. Stylianakis, E. Stratakis, E. Kymakis, J. Colloid Interface Sci. 2014, 430, 108.

76 L. Ashton, J. Dusting, E. Imomoh, S. Balabani, E. W. Blanch, Biophys. J. 2009, 96, 4231.

77 K. Hu, L. S. Tolentino, D. D. Kulkarni, C. Ye, S. Kumar, V. V. Tsukruk, Angew. Chem. 2013, 125, 14029; Angew. Chem., Int. Ed. 2013, 52, 13784.

78 K. Hu, V. V. Tsukruk, Chem. Mater. 2015, 27, 6717.

79 Y. Cheng, Z. Q. Zhang, Z. Teo, Int. J. Appl. Mech. 2013, 5, 1350007.

80 W. Qin, X. Li, W. W. Bian, X. J. Fan, J. Y. Qi, Biomaterials 2010, 31, 1007.

81 B. Akdim, R. Pachter, S. S. Kim, R. R. Naik, T. R. Walsh, S. Trohalaki, G. Hong, Z. Kuang, B. L. Farmer, ACS Appl. Mater. Interfaces 2013, 5, 7470.

82 C. A. Jimenez-Cruz, S. G. Kang, R. Zhou, Wiley Interdiscip. Rev.: Syst. Biol. Med. 2014, 6, 329.

83 A. N. Camden, S. A. Barr, R. J. Berry, J. Phys. Chem. B 2013, 117, 10691.

84 J. Guo, X. Yao, L. Ning, Q. Wang, H. Liu, RSC Adv. 2014, 4, 9953.

85 L. Baweja, K. Balamurugan, V. Subramanian, A. Dhawan, Langmuir 2013, 29, 14230.

86 J. Chen, X. Wang, C. Dai, S. Chen, Y. Tu, Phys. E 2014, 62, 59.

87 H. J. Jin, J. Park, R. Valluzzi, P. Cebe, D. Kaplan, Biomacromolecules 2004, 5, 711.

88 R. Xiong, H. S. Kim, L. Zhang, V. Korolovych, S. Zhang, Y. Yingling, V. Tsukruk, Angew. Chem. 2018, doi:10.1002/ange.20180376.

89 J. Zhong, M. Ma, W. Li, J. Zhou, Z. Yan, D. He, Biopolymers 2014, 101, 1181.

90 I. Greving, M. Cai, F. Vollrath, H. C. Schniepp, Biomacromolecules 2012, 13, 676.

91 X. Hu, K. Shmelev, L. Sun, E. S. Gil, S. Park, P. Cebe, D. Kaplan, Biomacromolecules 2011, 12, 1686.

92 J. Magoshi, M. Mizuide, Y. Magoshi, K. Takahashi, M. Kubo, S. Nakamura, J Polym Sci, Polym. Phys. Ed. 1979, 17, 515.

93 X. Sun, Z. Feng, T. Hou, Y. Li, ACS Appl Mater Interfaces 2014, 6, 7153.

94 A. Sionkowska, Prog Polym Sci 2011, 36, 1254.

95 X. Wang, L. X. Gong, L. C. Tang, K. Peng, Y. B. Pei, L. Zhao, L. B. Wu, J. X. Jiang, Composites Part A 2015, 69, 288.

96 D. N. Rockwood, R. C. Preda, T. Yücel, X. Wang, M. L. Lovett, D. L. Kaplan, Nat Protoc 2011, 6, 1612.

97 M. Savchak, N. Borodinov, R. Burtovyy, M. Anayee, K. Hu, R. Ma, A. Grant, H. Li, D. Cutshall, Y. In, G. Koley, W. Harrell, G. Chumanov, V. Tsukruk, I. Luzinov. ACS Appl Mater Interfaces, 2018, 10, 3975.

98 M. Grundner, H. Jacob, Appl. Phys. A 1986, 39 (2), 73.

99 J. Zhang, F. Zhang, H. Yang, X. Huang, H. Liu, J. Zhang, S. Guo, Langmuir 2010, 26 (9), 6083.

100 Z. Jia, Y. Wang, J. Mater. Chem. A 2015, 3 (8), 4405.

101 T. Jiang, T. Kuila, N. Kim, J. Lee, J Mater Chem A 2014, 2 (27), 10557.

102 Y. An, M. Chen, Q. Xue, W. Liu, J Coll Interf Sci 2007, 311, 507.

103 W. S. Hummers, R. E. Offeman, J Am Chem Soc 1958, 80, 1339.

104 R. Xiong, K. Hu, A. Grant, R. Ma, W. Xu, C. Lu, X. Zhang, V. Tsukruk, Adv Mater 2015, 28, 1501.

105 K. Min, T. Han, J. Kim, J. Jung, C. Jung, S. M. Hong, C. Koo, J. Colloid Interface Sci 2010, 383, 36.

106 J. Richardson, J. Cui, M. Bjornmalm, J. A. Braunger, H. Ejima, F. Caruso Chem Rev 2016, 116 (23), 14828.

107 K. Blodgett, I. Langmuir Physical Rev. 1937, 51, 964.

108 M. McConney, S. Singamaneni, V. Tsukruk, Polym Rev 2010, 50, 235.

109 S. Markutsya, C. Jiang, Y. Pikus, V. V. Tsukruk Adv Funct Mater 2005, 771.

110 Y. Wang, R. Ma, K. Hu, S. Kim, G. Fang, Z. Shao, V. V. Tsukruk ACS Appl. Mater. Interfaces 2016, 8 (37), 24962.

111 S. Malak, J. Jung, T. Yang, S. Wark, D. Son, J. Batteas, J Am Chem Soc 2009, 131, 18204.

112 W. Humphrey, A. Dalke, K. Schulten, J. Mol. Graphics, 1996, 14, 33.

113 San Diego: Accelrys Software Inc. Discovery Studio Modeling Environment, Release 3.5 2012.

114 A. Rimola, D. Costa, M. Sodupe, J. Lambert, P. Ugliengo, Chem Rev 2013, 113, 4216.

115 Y. Zhang, BMC Bioinf, 2008, 9, 40.

116 Z. Gong, L. Huang, Y. Yang, X. Chen, Z. Shao, Chem Commun 2009, 7506.

117 S. Inoue, J. Magoshi, T. Tanaka, Y. Magoshi, M. Becker, J Polym Sci Part B 2000, 38, 1436.

118 H. Shulha, C. Foo, D. Kaplan, V. Tsukruk, Polymer 2006, 47, 5821.

119 E. Hill, B. Krebs, D. Goodall, G. Howlett, D. Dunstan, Biomacromolecules 2006, 7, 10.

120 E. Kharlampieva, D. Zimnitsky, M. Gupta, K.Bergman, D. Kaplan, R. Naik, V. Tsukruk, Chem Mater 2009, 21, 2696.

121 X. Hu, D. Kaplan, P. Cebe, Macromolecules 2006, 39 (18), 6161.

122 C. Zhu, Y. Gao, H. Li, S. Meng, L. Li, J. S. Francisco, X. C. Zeng. Proceed Natl Acad Sci 2016, 113(46), 12946-12951.

123 K. Fujiwara, H. Toda, M. Ikeguchi *BMC Structural Biology* 2012, 12 (18).

124 H. S. Kim, B. L. Farmer, Y. G. Yingling *Adv Mater Interfaces* 2017, 4, 1601168.

125 U. Holzwarth, N. Gibson Nat Nanotechnol 2011, 6, 534.

126 J. Vlasak, W. Nix, J Mater Res 1992, 7, 3S. 242

127 S. Timoshenko, Theory of Plates and Shells; McGraw-Hill: New York, 1959.

128 J. Beams, Structure and Properties of Thin Solid Films; John Wiley: New York, 1959.

129 E. Kharlampieva, V. Kozlovskaya, B. Wallet, V. Shevchenko, R. Naik, R. Vaia, D. Kaplan, V. Tsukruk, ACS Nano 2010, 4, 7053.

130 C. Law, K. Wong, Z. Yang, K. Horsburgh, A. Monkman, Appl Phys Lett 2000, 76, 1416.

131 J. Affdl, J. Kardos, Polym Eng Sci 1976, 16, 344.

132 T. Posati, V. Benfenati, A. Sagnella, A. Pistone, M. Nocchetti, A. Donnadio, G. Ruani, R. Zamboni, M. Muccini, Biomacromolecules 2014, 15, 158.

133 M. de Moraes, T. Crouzier, M. Rubner, M. Beppu, Biomacromolecules 2015, 16, 97.

134 S. Yun, M. Kim, H. Kwak, J. Lee, M. Kim, E. Kim, H. Lee, Fibers Polym 2013, 14, 2111.

135 F. Gojny, W. Wichmann, U. Köpke, B. Fiedler, K. Schulte, Compos Sci Technol 2004, 64, 2363.

136 C. Jiang, S. Markutsya, V. Tsukruk, Adv Mater 2004, 16, 157.

137 S. H. Hiew, A. Miserez, A. Squid sucker ring teeth: multiscale structure–property relationships, sequencing, and protein engineering of a thermoplastic biopolymer ACS Biomater. Sci. Eng. 2017, 3, 680-693.

138 M. Chyasnavichyus, S. L. Young, V. V. Tsukruk, Langmuir 2014, 30 (35), 10566.

139 V. Tsukruk, S. Singamaneni, Scanning Probe Microscopy of Soft Matter: Fundamentals and Practices, John Wiley & Sons, Inc, 2011.

140 H. I Okur, J. Hladilkova, K. B.Rembert, Y. Cho, J. Heyda, J Dzubiella, J.; Cremer, P. S.; Jungwirth, P. J Phys Chem B 2017, 121 (9), 1997.

141 G. K. L. Chan, A. Witkowski; D. L. Gantz; T. O. Zhang, M. S. Zanni, S. Jayaraman, G. Cavigiolio, J. Biol. Chem. 2015, 290 (17), 10958.

142 C. S. Kim Y. J. Yang, S. Y. Bahn; H. J. Cha, NPG Asia Mat. 2017, 9 (6), e391.

143 K. Min, S. Kim, S. Kim., Proc. Natl. Acad. Sci. U. S. A. 2017, 114 (24), 6185.

144 D. L. Minor Jr, P. S. Kim, Nature 1994, 367 (6464), 660.

145 Y. K. Al-Hilaly, T. L. Williams, M. Stewart-Parker, L. Ford, L., E. Skaria, M. Cole, W. G. Bucher, K. L. Morris, A. A. Sada, J. R. Thorpe, L. C. Serpell, Acta Neuropathol. Commun. 2013, 1 (83).

146 B. P. Partlow, M. B. Applegate, F. G. Omenetto, D. Kaplan, ACS Biomater. Sci. Eng. 2016, 2 (12), 2108.

147 A. Perczel, Z. Gaspari, I. G. J. Csizmadia, Comput. Chem. 2005, 26 (11), 1155.

148 H. E. Stanger, F. A.Syud,J. F. Espinosa, I. Giriat, T. Muir, S. H. J. Gellman, Proc. Natl. Acad. Sci. U. S. A. 2001, 98 (21), 12015.

149 F. A. Syud, H. E. Stranger, H. S. Mortell, J. F. Espinosa, J. D. Fisk, C. G. Fry, S. H. J. Gellmanm, Molec. Bio. 2003, 326 (2), 553.

150 J. Hu, G. Wang, W. Zhao, X. Liu, L. Zhang, W. Gao, Biomaterials 2016, 96, 84.

151 N. M. B. Smeets, M. Patenaude, D. Kinio, F. M. Yavitt, E. Bakaic, F.-C. Yang, M. Rheinstädter, T. Hoare, Polym Chem 2014, 5, 6811

152 X. Shi, Y. Wang, D. Li, L. Yuan, F. Zhou, Y. Wang, B. Song, Z. Wu, H. Chen, J. L. Brash, Langmuir 2012, 48, 17011.

153 M. Liu, J. C. Leroux, M. A. Gauthier, Prog Polym Sci 2014, 48, 111.

154 A. Skandalis, S. Pispas, J Polym Sci, Part A 2017, 55, 155.

155 G. Wang, M. Chen, S. Guo, A. Hu, J Polym Sci Part A 2014, 52, 2684.

156 K. Knop, D. Pretzel, A. Urbanek, T. Rudolph, D. H. Scharf, A. Schallon, M. Wagner, S. Schubert, M. Kiehntopf, A. A. Brakhage, F. H. Schacher, U. S. Schubert, Biomacromolecules 2013, 14, 2536.

157 P. Scheibe, M. Barz, M. Hemmelmann, R. Zentel, Langmuir 2010, 26, 5661.

158 Y. Feng, C. Xiao, J Appl Polym.Sci 2006, 101, 1248.

159 D. Chatterjee, B. Mandal, Macromolecules 2006, 39, 9192.